Optical characterization of gradient in droplets : application to CO2 capture by MEA spray

Suttiya Chiewudomrat

Normandie Université

THESE

Pour obtenir le diplôme de doctorat

Spécialité Optique

Préparée au sein de INSA de Rouen - Normandie

Optical characterization of gradient in droplets: Application to CO_2 capture by MEA spray

Présentée et soutenue par
Suttiya CHIEWUDOMRAT

Thèse soutenue publiquement le 17 Mai 2018 devant le jury composé de		
M. Claude de BELLEFON	Directeur de Recherche CNRS, CPE à Lyon	Rapporteur
M. Emmanuel PORCHERON	HDR, Responsable du LPMA, IRSN à Paris	Rapporteur
Mme. Nadine GABAS	Professeur, ENSIACET à Toulouse	Examinateur
Mme. Sawitree SAENGKAEW	HDR, Présidente de Rainbow Vision	Examinateur
M. Sébastien LEVENEUR	HDR, Maître de Conférences, LSPC, INSA de Rouen	Co-encadrant
M. Lionel ESTEL	Professeur des universités, LSPC, INSA de Rouen	Directeur de thèse
M. Gerard GRÉHAN	Directeur de Recherche CNRS, CORIA	Co-directeur de thèse

Thèse dirigée par Lionel ESTEL, laboratoire LSPC et Gerard GRÉHAN, laboratoire CORIA

INSA INSTITUT NATIONAL DES SCIENCES APPLIQUÉES ROUEN NORMANDIE

ED PSIME

LSPC Laboratoire de sécurité des procédés chimiques

UMR 6614 CORIA COMPLEXE DE RECHERCHE INTERPROFESSIONNEL EN AEROTHERMOCHIMIE

ACKNOWLEDGEMENTS

This thesis would have not been accomplished without the supports of numerous people as well as the financial support provided by Ministère de l'Enseignement Supérieur et de la Recherche. Therefore, I would like to take this opportunity to thank for their supporting. This work was carried out under the collaboration between Laboratoire de Sécurité des Procédés Chimiques (LSPC) and COmplexe de Recherche Interprofessionnel en Aérothermochimie (CORIA). First, I would like to express my sincere appreciation to my advisers. I consider myself fortunate to have the great supports from them over these years.

Thankfully Dr. Lionel Estel for his kindness, and patience to teach and to discuss with me in chemistry, which I am not familiar. Many thanks for his suggestions throughout my PhD.

Thankfully Dr. Gerard Gréhan for his kindness, and patience for teaching me many things. His insightful guidance as well as discussions with him enlightened me and have better vision of the work. Many thanks for his continued support, and encouragement over these years.

Thankfully Dr. Sébastien Leveneur for his help and comment in chemical engineering view. Thanks for his effort to follow up my work.

Special thanks to Dr. Sawitree Saengkaew who gave me an opportunity to be a PhD student here. She always helps and encourages me for both working, daily life. Many thanks for her kindness, effort to teach and suggest me many things, especially for the setup of rainbow system and her inversion code. Moreover, thank you for being a member of committees in my defense.

I also would like to express my gratitude to my thesis committees, Dr. Claude de Bellefon, Dr. Emmanuel Porcheron, and Dr. Nadine Gabas for their efforts to read my work, and providing thoughtful suggestions.

I would like to thank Benjamin Quevreux, Philippe Toutain, Jacky Galle, and other workshop staffs for the technical supports. Next, thanks to Gilles Godard for lending me the CO_2 detector. Thanks to informatics team for service of computer and network.

I would like to thank all my friends here during my PhD (Lila, Stan, Manuel, Zelong, Marcos, Frédéric, Mohamed, etc.) who are always ready to give me a help whenever I needed. Special mentions go to Lila Ouldarbi and Stanislas Grare who gave the suggestions about image processing in Matlab. I also would like to thank Maria Ouboukhlik who is a previous student worked in CO_2 capture by MEA spray, for her suggestions and helps.

Thanks to Jantarat Promvongsa for her help, suggestion, and being nice sister, she always gives me a hand whenever I asked for. Thanks to Chanisa Kanjanasakul who always talked a lot with me about our work and our life, which made me never lonely. Many thanks for her encouragement and being nice sister. Thanks also to Darawan Pejchang and Wisuttida Wichitwong. My Thai family in Rouen is fulfilled by all of them including the most important person Dr. Sawitree Saengkaew.

Finally, I would like to express my deepest gratitude to my parents and my family in Thailand, who give me the endless support and encouragement. Thank you for always being there for me.

ABSTRACT

Reactive sprays can be found in numerous industries. The characterization of transient state for such droplets is a challenge, asks for the measurement of temperature and/or composition gradients inside the droplets. In this thesis, Global Rainbow Technique (GRT) is extended to be able to quantify the behavior of gradients. After the numerically studied on the characteristics of rainbow scattered by droplet with radial refractive index gradients, an experimental study is carried out for the particular case of CO_2 capture by MEA droplets. According to the investigation, it is demonstrated that the gradients can be quantified during the first moments of injection. The analysis of GRT measurement based on the droplet with or without gradients indicates the identical behavior when the reacting time is long enough.

Keywords : Rainbow technique, Droplet gradients characterization, CO_2 capture

CONTENTS

List of Figures

List of Tables

Nomenclature

Greek symbols

α	Mole ratio of CO_2 to MEA
β	Angle of refraction (°)
κ	Thermal conductivity of MEA30%wt (W/(m·K))
κ_{AA}	Thermal conductivity between water-water molecules (W/(m·K))
κ_{AB}	Thermal conductivity between water-MEA molecules (W/(m·K))
κ_{BB}	Thermal conductivity between MEA-MEA molecules (W/(m·K))
κ_{MEA}	Thermal conductivity of MEA (W/(m·K))
κ_{water}	Thermal conductivity of water (W/(m·K))
λ	Incident wavelength (μm)
ν	Parameter of strength of hydrogen bond
ν_A	Parameter of strength of hydrogen bond for water
ν_B	Parameter of strength of hydrogen bond for MEA
ρ	Density of MEA30%wt (g/cm^3)
σ	Size parameter of a molecule
σ_A	Size parameter of water molecule
σ_B	Size parameter of MEA molecule
τ	Angle of incidence (°)
θ_{rg}	Rainbow angle (°)
ε	Potential parameter
ε_A	Potential parameter of water
ε_B	Potential parameter of MEA

Abbreviations

$\bar{D}$	Mean diameter of molecules
ΔH_R	Total enthalpy change of a reaction (kJ/mol)

$\Delta[CO_2]$	The change in concentration of CO_2 absorbed (mol/L)
$\Delta CO_{2,abs}$	Quantity difference of CO_2 absorbed (mol)
Δt_c	Contact time difference (s)
$\dot{N}_{CO_2}$	CO_2 absorbed flux (mol/(m^2·s))
$\dot{V}$	Volume flow rate of liquid injection (ml/min)
$\tilde{T}$	Logarithmic mean temperature difference (K)
A	Frequency factor for the reaction (L/(mol·s))
A_d	Cross-sectional area of orifice (cm^2)
b	a coefficient that controls gradient profiles
c_p	Specific heat capacity of MEA30%wt at constant pressure (J/(kg·K))
D	Diameter of orifice (μm), (m)
d	Droplet size (μm), (mm), (m)
d_i	Initial droplet size (mm)
d_{32}	Sauter mean diameter (μm), (mm)
$D_{CO_2,MEA30\%}$	Diffusion coefficient of CO_2 in MEA30%wt (m^2/s)
d_{eq}	Equivalent droplet size (μm)
E_a	Activation energy (J/mol), (kJ/mol)
f	Excitation frequency (Hz), (kHz)
g	Gravitational acceleration (m/s^2)
Ha	Hatta number
k	Dimensionless wavelength (in Appendix B.1)
k	Reaction rate coefficient (L/(mol·s))
k_L	Liquid side mass transfer coefficient (m/s)
$k_{Boltzmann}$	Boltzmann constant
Le	Lewis number
M	Molecular weight (g/mol)
M_A	Molecular weight of water (g/mol)
M_B	Molecular weight of MEA (g/mol)
M_{CO_2}	Molecular weight of CO_2 (g/mol)
m_{CO_2}	Weight of CO_2 (g)

M_{MEA}	Molecular weight of MEA (g/mol)
m_{MEA}	Weight of MEA (g)
n	Refractive index
n_c	Refractive index at the center of droplet
n_i	Refractive index at each droplet layer
n_s	Refractive index at the surface of droplet
N_{CO_2}	Mole number of CO_2 (mol)
n_{eq}	Equivalent refractive index
N_{MEA}	Mole number of MEA (mol)
p	Path light inside droplet
P_{vapor}	Vapor pressure (kPa)
R	Universal gas constant (J/(K·mol))
r	reaction rate (mol/(L·s))
r_i	Radius at each droplet layer
s	Distance from orifice (mm), (m)
S_d	Interfacial area of droplet (m^2)
T	Temperature (°C), (K)
t	Traveling time (ms), (s)
t_c	Contact time (ms), (s)
T_{amb}	Ambient temperature (°C)
T_b	Boiling temperature (°C), (K)
T_{cr}	Critical temperature (K)
T_c	Temperature at the center of droplet (°C)
T_s	Temperature at the surface of droplet (°C)
u	Discharge velocity of droplet (m/s)
V_i	Volume at each droplet layer (m^3)
$V_{cr,A}$	Critical volume of water (cm^3/mol)
$V_{cr,B}$	Critical volume of MEA (cm^3/mol)
V_{cr}	Critical volume (cm^3/mol)
W_A	Weight fraction of water
X	A dimensionless number, for identifying the used function to compute liquid side mass transfer coefficient

x	Dimensionless radius
z_1	Correction parameter 1
z_2	Correction parameter 2
r'_A	Number fraction of water molecules
$[CO_2]$	Molar concentration of CO_2 (mol/L)
$[CO_2]_i$	Molar concentration of CO_2 at each droplet layer (mol/L)
[MEA]	Molar concentration of MEA (mol/L)
CCS, CCU	Carbon Capture and Storage, Utilization
CERS	Cavity Enhanced Raman Scattering
CFCs	Chlorofluorocarbons
DEA	Diethanolamine
FGD	Flue-Gas Desulfurization
GLMT	Generalized Lorenz-Mie Theory
GRT	Global Rainbow Technique
IPI	Interferometric Particle Imaging
LIF	Laser-Induced Fluorescence
MDEA	Methyldiethanolamine
MDRs	Morphology Dependent Resonances
MEA	Monoethanolamine
ORT	One-dimensional Rainbow Technique
PDA	Phase Doppler Anemometry
TIC	Total Inorganic Carbon
TLC	Thermochromic Liquid Crystal

Chemical formula

CH_4	Methane
CO	Carbon monoxide
CO_2	Carbon dioxide
H_2	Hydrogen
H_2O	Water
HCl	Hydrochloric acid
HCO_3^-	Hydrogen carbonate ion

$HOCH_2CH_2NH_2$	Ethanolamine, Monoethanolamine
$HOCH_2CH_2NH_3^+$	Protonated amine
$HOCH_2CH_2NHCOO^-$	Carbamate
N_2	Nitrogen
N_2O	Nitrous oxide
NaOH	Sodium hydroxide
NH_3	Ammonia
NO_x	Nitrogen oxides which mostly affect to air pollution i.e. nitric oxide (NO), nitrogen dioxide (NO_2)

CHAPTER 1

Introduction

1.1 General introduction

Chemical industry is one of the largest manufacturers creating a variety of products which impinge on various aspects to human life such as food, pharmaceutical, petroleum, cosmetics, polymers etc. These activities use a large quantity of energy and at the same time are potentially sources of pollution. Classically, the chemical industry processes are sorted as unit operations which are combined in order to create a manufacturing process. Separation systems are one of the unit operations which can be used for different functions such as purification of raw materials and products, removal of contaminants from effluents etc. These separation processes account for 40-90% of capital investment and operating costs in chemical industries, accordingly the development of systems reducing the used energy as well as the creation pollutants can significantly reduce costs and increase profits [11].

Up to now, the most popular approach to predict the behavior and design systems are global approaches, based on the assumption of a steady state. Such approaches can lead to the wrong scale up and mass/ energy balances. Another approach, nowadays possible thanks to the development of computers and associated simulation codes, is a local approach where the evolution of system is followed at the smallest possible scale. This kind of approaches can include the study of transient state systems permitting a better understanding of systems, and therefore to deal with the intensification of the process.

Gas streams are intensively dealt in the process industries, separation systems are exploited in order to remove one or several gaseous components prior using as feedstock or releasing to atmosphere. Several methods exist for gas treatment e.g. adsorption, cryogenic, membrane, absorption (chemical, physical) etc. [12]. Among aforementioned methods, absorption is an important unit operation with a high level of technical implementation and maturity [13]. Absorption can be classified in two categories which are physical absorption and chemical absorption. Both categories use solvent as absorbent to separate the unwanted component in gas phase. For physical absorption, the certain component is physically absorbed by a solvent (e.g. Methanol, Selexol which is a mixture of the dimethyl ether of polyethylene glycol etc.) according to Henry's law meaning it is dependent on pressure and temperature. The process is based on the solubility of gas in the solvents, thus the higher partial pressure and lower temperature for gas phase are preferable. For regeneration process, the heating process or pressure reduction is applied in order to release the absorbed component from the solvent. In contrast, chemical absorption is a powerful separation method which exploits the reaction between gas and liquid phases. Type of solvents and its concentration can be selected permitting to control the absorption rate and absorption capacity. Different types of contactor are employed to create the area of exchange between gas-liquid phases which can be classified according to the mechanisms [14].

- Generating small bubbles of gas into a continuous liquid phase (e.g. plate column, bubble column)
- Spreading the liquid to be thin films passing through the continuous gas phase (e.g. packed column, wetted-wall column)
- Injecting the liquid to be small droplets in continuous gas phase (e.g. spray system)

The classical contactors such as plate column, packed column etc. are commonly used, nevertheless the exchange surface area is relatively small. Since, the area of exchange is one of the main parameters of gas-liquid mass transfer, thus the use of spray system can be a good alternative in order to increase the contacting area. The size of contacting area provided by classical contactors and spray system was roughly compared by considering the identical thickness and liquid volume. For example, liquid volume 1 m^3 can be spread to be liquid film with thickness 100 μm providing the area of exchange 10,000 m^2 for classical contactors while the area can be increased to be 60,000 m^2 for spray system with droplet size 100 μm. In the case of chemical absorption, the contactor such as plate column, packed column etc. can be used as the conventional reactors, however it is limited by highly corrosive system e.g. flue-gas desulfurization (FGD). On the other hand, spray system is able to work with highly corrosive system due to the direct contact between gas-liquid phases. In addition, spray system was applied for FGD system in industry such as Alabama Electric (USA), Dominion Energy (USA) etc. [15, 16]. However, the characteristics of heat and/or mass transfer, including chemical kinetics, in spray system are fairly studied and have not been well described. Accordingly, further studies are required to fulfill gap addresses.

Generally, chemical reactions are studied in the bulk configurations. Nevertheless, chemical reaction in spray system is carried out with droplets which involve local chemical kinetics and/or local mass transfer. For example, the kinetics of reaction could be increased by a factor of a thousand or a million according to the kind of reaction when the chemical reaction takes place with the droplets electrically charged [17]. Therefore, the intrinsic kinetics/ mass transfer in the droplets are necessary to be studied. In the framework of this PhD, the characteristics of gas-liquid mass transfer in droplets have been investigated for a particular case i.e. CO_2 capture by MEA droplets. The better understanding of spray system could lead to the minimization of the setup which could be extended to apply with moving systems such as ships, automobiles etc.

1.2 Application to CO_2 capture technology

Greenhouse effect relies on the greenhouse gases in the atmosphere permitting the sunlight to pass through and trapping heat, then re-emit to the Earth's surface [18, 19]. The primary components of greenhouse gases are water vapor, Carbon dioxide (CO_2), Methane (CH_4), Nitrous oxide (N_2O), Ozone (O_3) and Chlorofluorocarbons (CFCs) [20]. However, the increase of excessive greenhouse gases especially CO_2 creates the climate change on the Earth (global warming problem). The pie chart in Figure 1.1 demonstrates greenhouse gases emission in 2004 confirming that CO_2 is significantly increased due to human activities, for example the use of fossil fuel, deforestation etc. [1]. Accordingly, CO_2 emission must be limited in order to prevent the long term effects. There are various strategies to reduce CO_2 emission e.g. the use of renewable energy, afforestation and reforestation, Carbon Capture and Storage, Utilization (CCS, CCU) etc. [21]. CCS or CCU is a strategy which limits CO_2 at emission sources providing the capture efficiency more than 80% [21]. This strategy consists of three main units which are CO_2 capture, CO_2 transport, and

storage, utilization of CO_2. In this study, only the CO_2 capture unit will be described. There are three available technology options which are post-combustion, oxy-fuel combustion, and pre-combustion [12]. The description of basic principle for each technology is provided below, and the schematic diagram of each technology for coal power plant is displayed as an example in Figure 1.2.

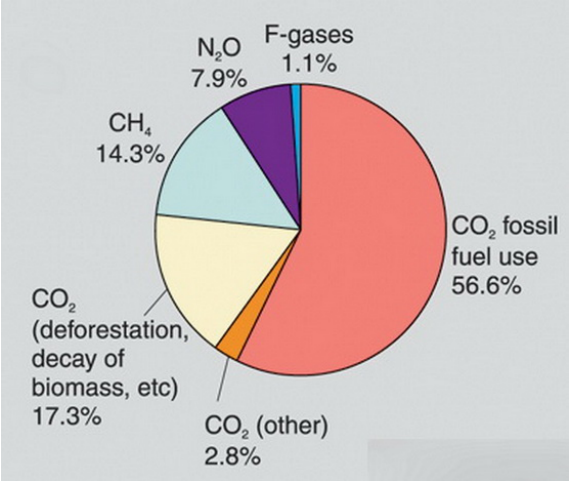

Figure 1.1: The emission of greenhouse gases in 2004 [1]

- **Oxy-fuel combustion technology** [12, 21, 22]

  Oxy-fuel combustion is a technology which fuel is combusted with pure oxygen instead of air, accordingly NO_x is not existed in exhaust gas. For example, in the coal power plants, an air separation unit is used to separate N_2 from the air to produce pure oxygen which is injected with a fuel where the combustion is taken place. Then, flue gas which mainly consists of CO_2 and water vapor passing through CO_2 separation unit before access to the ambient. This technology provides high concentration of CO_2 in flue gas, thus a simple CO_2 separation system is required. However, this technology consumes a lot of energy in order to produce pure oxygen.

- **Pre-combustion technology** [12, 21, 23]

  Fuel is pre-treated before the combustion process. For example, in the coal power plants, air or oxygen reacts with fuel in gasifier to form a synthesis gas (syngas) which is mainly composed by CO_2, Carbon monoxide (CO) and Hydrogen (H_2). The syngas reacts with steam in a shift reactor to produce CO_2 and more H_2. CO_2 is then separated resulting in the H_2-rich fuel which can be used in applications such as gas turbines, boilers, furnaces etc.

- **Post-combustion technology** [12, 21, 22]

  Fuel is combusted with air given power and heat. Then, the flue gas passes through CO_2 separation unit before access to ambient. The partial pressure of CO_2 in flue gas obtained from post-combustion is lower than pre-combustion and oxy-fuel combustion, accordingly a powerful separation system is required.

Each technology has its advantages and disadvantages permitting to select the most suitable technology for certain conditions and limitations in the used system. This study is focused on the post combustion technology since it is suitable for both newly plants and retrofitted to the existing plants. Moreover, there is no any modification on combustion process. Therefore, the chemical absorption which is suitable to work with low to moderate concentration of CO_2 is focused.

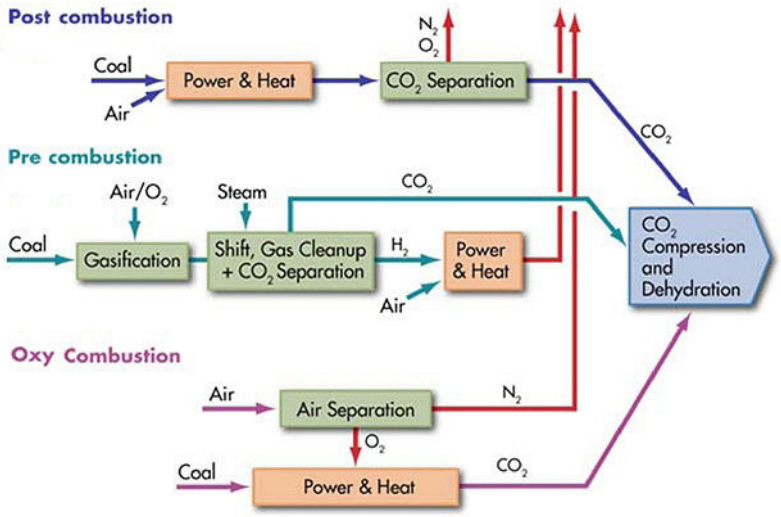

Figure 1.2: Technology options for CO_2 capture from coal power plants [2]

1.3 Chemical absorption for CO_2 capture process

This method is based on acid-base neutralization reaction between gas and liquid phases, thus the alkaline solvents have been utilized to capture acid gases. Different solvents such as NH_3, NaOH etc. had been explored in spray system [24–27]. Monoethanolamine (MEA) is one of the preferred solvents for CO_2 capture system, however it is scarcely studied in spray system especially for the investigation on moving droplets in order to access the transient state.

The basic principle of chemical absorption can be illustrated in Figure 1.3. The process is performed in two steps which are absorption and regeneration (desorption). In this study, MEA is considered as the solvent used for CO_2 capture system, therefore the description of the process is based on the couple of MEA-CO_2 system. For absorption process, the flue gas containing CO_2 enters to the absorption column, then it is in contact with the injected solvent from the top of column resulting in a chemical product as a consequence of chemical reaction. Then, the chemical product is flowed to the desorption column for thermal regeneration process. The operating temperature of desorption column is reached to the range of 120°C-140°C in order to release CO_2 and obtained the CO_2 unloaded solvent [28]. Accordingly, the solvent is used cyclically while CO_2 is used or prepared to be transported and stored.

1.4 Objective and scope

In order to optimize CO_2 capture by spray system, the characteristics of heat and mass transfer phenomena must be known. To reach this aim, it is critical to understand the interaction between liquid and gas phases in the droplets. The accurate characterization of heat and mass behavior inside the droplet asks for the measurement of the gradients of species and/or temperature. Up to now, no devices are able to realize such measurement of gradients. Accordingly, the objective of this thesis is to apply optical technique to evaluate gradients in droplets. To perform such a measurement, a suspended droplet and/or a line of moving monodisperse droplets are used instead of spray to eliminate the complex parameters [4].

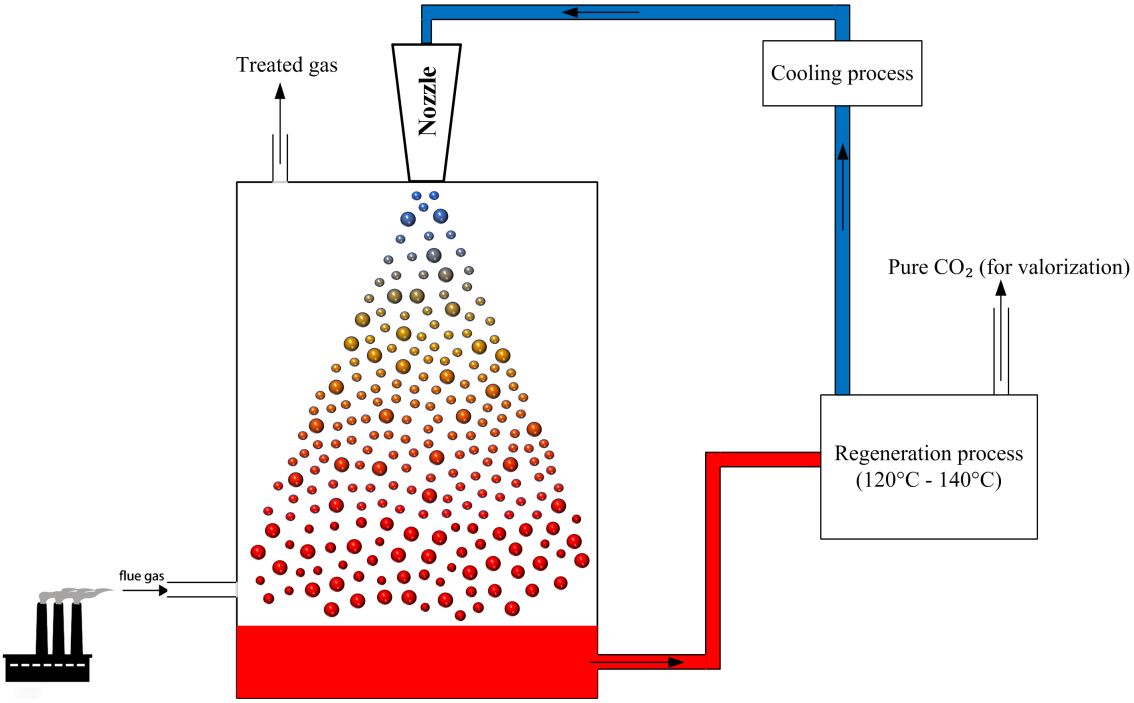

Figure 1.3: Basic principle of absorption and desorption systems for CO_2 capture process

1.5 The structure of this thesis

This thesis will be organized as followed. Chapter 2 indicates the basic background which is applied in this study. The literature review of experimental studies on CO_2 capture by MEA droplets is presented. Attention is given to the complex interaction between MEA droplets and CO_2. Rainbow technique is proposed to be an optical tool in order to characterize droplet properties. Additionally, the correlation of refractive index and concentration of CO_2 at different temperatures is presented.

Chapter 3 introduces the effect of gradients inside droplets on rainbow measurement. The literature review of previous studies for droplets with gradients is presented. The simulation of rainbow signals for a multilayered spherical droplet is provided in order to predict the rainbow signals according to our case study.

Chapter 4 provides the rainbow measurement on a suspended droplet. The experimental setup as well as the optical setup of rainbow system are described. In addition, the explanations of data processing and experimental results are presented.

Chapter 5 demonstrates the rainbow measurement on a line of moving monodisperse droplets with different conditions. Specially, the experiment during CO_2 absorption shows the effect of gradients inside droplets. The evolution of refractive index from experiment and simulation are compared in order to evaluate the gradient profiles. The effect of spatial thermal gradient due to the exothermic process is clarified. Moreover, the computation of activation energy and Hatta number are provided which the obtained values support the hypothesis of the existence of gradients in droplets. Finally, the quantity of CO_2 absorbed is provided.

Chapter 6 is the summary of this study. Some perspectives are discussed for the future research.

CHAPTER 2

Basic background

2.1 Chemical reaction between MEA and CO_2

The absorption process is focused to realize the interaction between gas and liquid droplets in this study, the couple of monoethanolamine (MEA) and CO_2 was selected to be the studied case. Ethanolamine or monoethanolamine is an organic compound where the chemical formula can be written as $HOCH_2CH_2NH_2$. It is a viscous colorless liquid and able to be miscible into water. According to its alkalinity, MEA is exploited to capture acid gas i.e. CO_2, well known in chemical absorption process. The chemical reaction between MEA and CO_2 can be denoted as the equation of reaction (2.1), where R refers to $HOCH_2CH_2$ [4, 29].

$$2\,RNH_2 + CO_2 \rightleftharpoons RNHCOO^- + RNH_3{}^+ \qquad (\Delta H_R = -90kJ/mol) \qquad (2.1)$$

According to the reaction, a major product called "carbamate" is created which induces to have the modification on droplet composition and also generates heat due to the exothermic process. From the equation (2.1), it is demonstrated that the molar ratio between CO_2 and MEA is limited to be 0.5. However, the carbamate can slowly continue to react with CO_2 and H_2O to form hydrogen carbonate ions ($HCO_3{}^-$). This reaction is generally neglected due to the short exposure times of the liquid to the gas encountered in absorber [29]. Nevertheless, it can result higher molar ratio than the predicted value according to equation (2.1) [4].

2.2 Previous studies on CO_2 capture by MEA aqueous droplets

The investigations of capture performance as well as mass transfer in the case of CO_2 capture by MEA aqueous droplets were carried out by several research groups which are described as followed.

In 2008, Kuntz et al. [30] studied the performance of spray column (inside diameter: 10 cm, height: 55 cm) for liquid temperature 25°C. Different spray nozzles (orifice sizes: 0.508 mm, 0.711 mm, 1.02 mm) were used, however the information of droplet size is unknown. The effects of various parameters i.e. gas flow rate, liquid flow rate, CO_2 partial pressure, MEA concentration, and CO_2 loading were presented. In their study, the infrared gas analyzer was used to measure CO_2 concentrations in gas phase before the gas entered to the column and at the point where the gas exited the column. In addition, the liquid sample collected from the bottom of column was analyzed by adding excess hydrochloric acid (HCl) solution. Then, the amount of released CO_2 was used to calculate the quantity of CO_2 captured and verified with the data from gas phase. It was concluded that the liquid flow rate was the most influence factor which affected the variation on mass transfer

performance of spray column. Moreover, the performance between spray column (orifice size: 1.02 mm) and structured packed column (inside diameter: 10 cm, height: 80 cm) was compared under the identical condition (MEA concentration 5 kmol/m^3 $\approx$ MEA30%wt). It was found that the spray column provided better performance for removing CO_2 from gas streams than the packed column by a factor of 2-7.

In 2011, Koller et al. [31] investigated the effect of liquid to gas ratio on CO_2 removal efficiency of simplified single nozzles using MEA30%wt as a solvent at temperature in absorption column 40°C. Two nozzles with different droplet sizes were used, the information of droplet size are not clearly reported. The capture efficiency for demonstration scale operating in continuous absorption/desorption cycle was measured. The smaller droplet indicated better removal efficiency, nevertheless it was fairly low.

In 2014, Seyboth et al. [32] selected two experimental approaches (laboratory scale and pilot scale) to study the CO_2 capture by spray system. In laboratory scale, CO_2 absorption by single falling droplets had been performed. The different droplet sizes (3.2 mm, 4.1 mm, 4.6 mm) was injected in a cylinder chamber (inner diameter: 3.4 cm, height: 250 cm) operating at atmospheric pressure and temperature 40°C. MEA30%wt with different initial loading ratios (mole of CO_2/mole of MEA) was used in order to investigate the influence of CO_2 loading solvent on the rate of absorption. N_2 was used to flush the space around droplet formation and collection, therefore the absorption of CO_2 was taken place while the droplet was falling. Liquid sample was collected from the bottom of column to analyze by adding excess HCl acid to quantify the absorption rate which was used to estimate the required column height. It was reported that the optimum droplet size for a larger scale was expected to be in the range of 1-2 mm.

In the pilot plant system, a designed prototype was tested in the closed loop absorption/desorption with a nozzle providing Sauter mean diameter (d_{32}) 1.6 mm at operating temperature in absorption column 40°C. The absorption system consisted of three consecutive spray columns, each 5 m high and with inner diameter 0.37 m. In their study, the infrared gas analyzes were applied to measure CO_2 concentration at different sampling points (top, middle, bottom of each column) which was used to calculate the removal efficiency. Moreover, the liquid samples were collected in order to determine CO_2 solvent loading. From the tested system, the good removal efficiency was obtained, however the mass transfer efficiency was approximately 10% - 20% lower than the data from laboratory scale.

In 2014, a unit part of spray system was studied by Han [3]. The CO_2 absorption by individual droplets with diameter in the range of 2.5 mm to 2.9 mm was presented. The experimental apparatus of Han's work is displayed in Figure 2.1. Water and MEA30%wt were used as liquid solvents, the study of mass transfer was considered on both with and without chemical reaction. The experiment was performed in a chamber (dimension: 3 cm $\times$ 3 cm $\times$ 60 cm) which was saturated by humid CO_2. The bottom of the chamber was filled with kerosene to avoid the reaction between the fallen droplet and CO_2. The droplet was quickly submerged into kerosene as the density of kerosene is lower than water and MEA30%wt. An overflow tube (u-tube) was used to keep constant the level of kerosene during the experiment. The study was carried out during the droplet formation and fall. Soap film flow meter was used to measure the rate of CO_2 filled up in the chamber. An average temperature over the chamber which was obtained by measuring the temperatures of gas phase in the chamber at two heights (upper part and lower part), kerosene, and liquid phase was used for the calculation liquid phase mass transfer coefficient. The measurements of droplet formation were separately performed at different average temperatures (water: 24°C and 50°C, MEA30%wt: 50°C) to determine the absorption rate of droplet formation. Whereas the measurements of droplet formation and fall were done at different heights and average

temperatures (Water: 30°C and 50°C at height 41 cm and 59 cm, MEA30%wt: 30°C at height 14 cm, 25 cm, 53 cm and 50°C at height 7 cm, 17 cm, 33 cm, 52 cm). The falling height was adjusted by changing the level of kerosene. The absorption rate of droplet fall was determined from the difference between the total absorption rate and absorption rate of droplet formation. For water droplets, the liquid phase mass transfer coefficient increased with the rise of average temperature over the chamber and falling droplet height, nevertheless it decreased as the droplet formation time increased. For MEA30%wt droplets, the liquid phase mass transfer coefficient increased with the rise of average temperature over the chamber and falling droplet height.

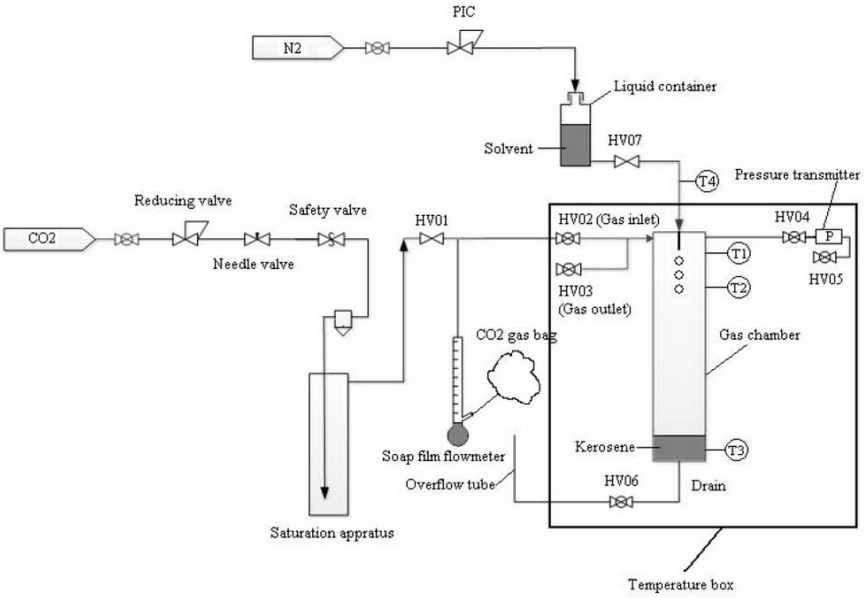

Figure 2.1: The experimental apparatus for CO_2 absorption by individual droplets in the work of Han [3]

In 2015, Tamhankar et al. [33] performed the measurements of CO_2 capture by MEA30%wt and MEA40%wt spray at liquid temperature 30°C. Spray column has inside diameter 0.2 m with 3 m height. From their study, the liquid sample was collected from the bottom of spray column and analyzed by using Total Inorganic Carbon (TIC) to determine the quantity of CO_2 loaded. In addition, Phase Doppler Anemometry (PDA) was used to measure drop size distributions at different concentric spray regions permitting to quantify planar surface area. According to the obtained size distributions from PDA, Sauter mean diameter (d_{32}) of the spray was in the range 150 μm - 300 μm. From the study, it was reported that the increase of MEA concentration and liquid flow rate provided higher mass transfer coefficients. Moreover, the increasing liquid flow rate resulted the larger planar surface area.

In 2015, the local optical measurement during droplets falling was performed by Ouboukhlik et al. [4, 34, 35]. Global Rainbow Technique (GRT) was applied to trace the evolution of CO_2 absorbed by MEA30%wt spray. The experimental system is displayed in Figure 2.2. The chamber consists of a cylinder column diameter 18 cm with 30 cm height connecting to a rectangular chamber dimension 20 cm $\times$ 30 cm $\times$ 30 cm. MEA30%wt spray was injected into the chamber which was provided a continuous CO_2 flow. Then, the measurement was performed at different positions (every 5 cm from 5 cm to 25 cm from orifice). By using GRT, average refractive index and drop size distribution were obtained. The measured refractive index in each position was converted to CO_2 concentration by using a correlation. An average temperature of liquid in CO_2 ambient obtained from a

thermocouple was about 45°C. Moreover, PDA was applied to characterize water spray providing the droplet velocity and drop size distribution. It was found that the average droplet velocity was about 1.2 m/s with Sauter mean diameter (d_{32}) in the range 80 μm - 120 μm.

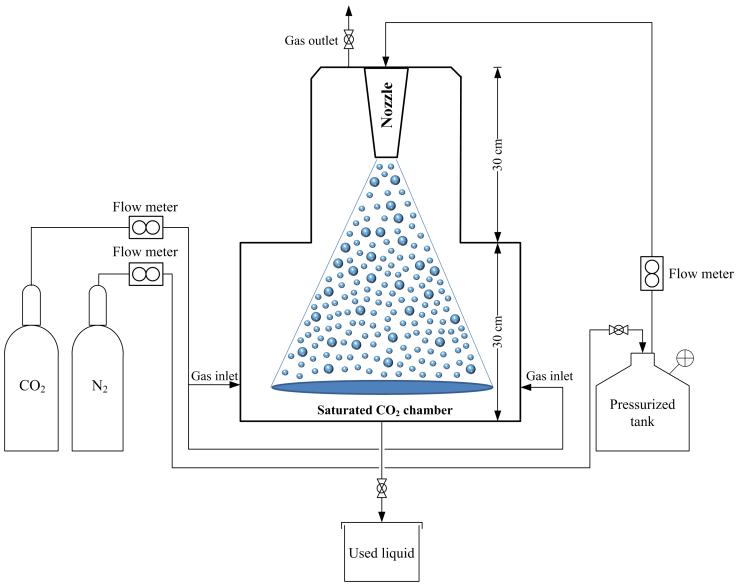

Figure 2.2: Experimental system of CO_2 absorption by MEA aqueous spray in the work of Ouboukhlik (modified, [4])

In 2017, the developed pilot plant system [32] was further investigated by studying the influence of two different nozzles (d_{32} = 1.6 mm with spray angle 90°, d_{32} = 1.1 mm with spray angle 45°) by Zimmermann et al. [36]. MEA30%wt was used in the study and the temperature in absorption column was about 40°C. The smaller droplet size demonstrated better CO_2 removal efficiency which suggested to the reducing of column height.

In 2017, Wu et al. [37] investigated overall mass transfer coefficient of CO_2 absorption in a diameter-varying spray tower (diameter: 12-20 cm, height: 50 cm). Dual-nozzle opposed impinging spray with orifice size 500 μm was used in the experiments, however the information of droplet size is unknown. The infrared gas analyzers were applied and continuously measured CO_2 concentration on both gas inlet and gas outlet. Several parameters i.e. MEA concentration, liquid flow rate, gas flow rate, and CO_2 concentration were varied in order to investigate the overall mass transfer coefficient. The results showed that the higher mass transfer coefficients were obtained when liquid to gas ratio and mole ratio of MEA to CO_2 were increased.

The investigations of CO_2 capture by MEA droplets were studied at different scale systems and different droplet sizes i.e. droplet size in the ranges of millimeters to micrometers, column height in the ranges of 55 cm to 15 m which cannot be directly compared. The effect of liquid flow rate which resulted in the increase of exchange surface was demonstrated to be an influence factor to the mass transfer performance in previous studies [30, 33, 37]. The better captured performance was also found with the smallest droplet size [36]. However, it was reported that mass transfer performance was underestimated from the prediction [32, 34]. Among these studies, the investigations were mostly obtained from the overview of system i.e. analyzing CO_2 absorbed by a liquid sample or determining the reduction of CO_2 at the gas outlet. Although, the evolution of CO_2 absorbed was measured by Ouboukhlik et al. [4, 34, 35], however the hypothesis of homogeneous droplet was applied to analyze the obtained data. Therefore, in this study, the evolution of CO_2 absorbed by MEA droplets is further investigated to access the local analysis.

Table 2.1: Summary of previous studies on CO_2 capture by MEA aqueous droplets

Authors	**Operating system**	**Used technique**	**Main result**
Kuntz et al. (2008)	Spray column (diameter 10 cm, height 55 cm), droplet size: not reported	• Infrared gas analyzer • adding excess HCl acid to liquid samples	Spray column provided better captured performance than structured packed column by a factor of 2-7.
Koller et al. (2011)	Spray system in demonstration scale (not reported the column size), droplet sizes: not clearly reported	Not reported	Single spray nozzle demonstrated low removal efficiency.
Seyboth et al. (2014)	• Individual droplets (chamber diameter 3.4 cm, height 250 cm), droplet size: 3.2 mm, 4.1 mm, 4.6 mm • Spray column (diameter 0.37 m, total height of absorption system 15 m), d_{32} 1.6 mm	• Infrared gas analyzer • adding excess HCl acid to liquid samples	• The optimum droplet size for a large scale can be expected in range of 1-2 mm. • A designed prototype was achieved a good removal efficiency, however the mass transfer efficiency was approximately 10%-20% lower than the data from laboratory scale.
Han (2014)	Individual droplets with size in the range of 2.5 mm to 2.9 mm (chamber dimension: 3 cm × 3 cm × 60 cm)	Using soap film flow meter to measure the rate of filled up CO_2 in chamber	Liquid phase mass transfer coefficient for MEA30%wt droplets increased with the rise of average temperature over the chamber and falling droplet height.

Continue on the next page

Table 2.1: Summary of previous studies on CO_2 capture by MEA aqueous droplets (cont.)

Authors	**Operating system**	**Used technique**	**Main result**
Tamhankar et al. (2015)	Spray system (diameter 0.2 m, height 3 m), d_{32}: 150 μm - 300 μm	• Using Total Inorganic Carbon to analyze liquid samples • Using PDA to measure drop size distribution	• The increase of MEA concentration and liquid flow rate provided higher mass transfer coefficients. • The increasing liquid flow rate resulted the larger planar surface area.
Ouboukhlik et al. (2015)	Spray system (chamber: total height 60 cm), d_{32}: 80 μm - 120 μm	• Using GRT to measure evolution of refractive index • Using PDA to measure droplet velocity and size distribution	The evolution of CO_2 absorbed was evaluated based on the hypothesis of homogeneous droplets.
Zimmermann et al. (2017)	Spray column (diameter 0.37 m, total height of absorption system 15 m), d_{32}: 1.6 mm, 1.1 mm	• Infrared gas analyzer • adding excess HCl acid to liquid samples	The smaller droplet size demonstrated better CO_2 removal efficiency.
Wu et al. (2017)	Dual-nozzle opposed impinging spray column (diameter 12-20 cm, height 50 cm), droplet size: not reported	Infrared gas analyzer	The higher mass transfer coefficients were obtained when liquid to gas ratio and mole ratio of MEA to CO_2 were increased.

2.3 Interaction between MEA droplet and CO_2

According to CO_2 absorption by MEA droplets, the investigation of interaction between MEA droplet and CO_2 is needed in order to have a better understanding on gas-liquid mass transfer. In the system without chemical reaction, the heat transfer according to Fourier's law depends on the surface of exchange as well as the mass transfer according to Fick's law. This fact supports that the surface of exchange is one of major factors to the mass transfer if chemical reaction has not been involved. Nevertheless, in the case of chemical reaction as for CO_2 capture by MEA droplets, the reaction takes place and a new component has been created which can affect the mass transfer efficiency.

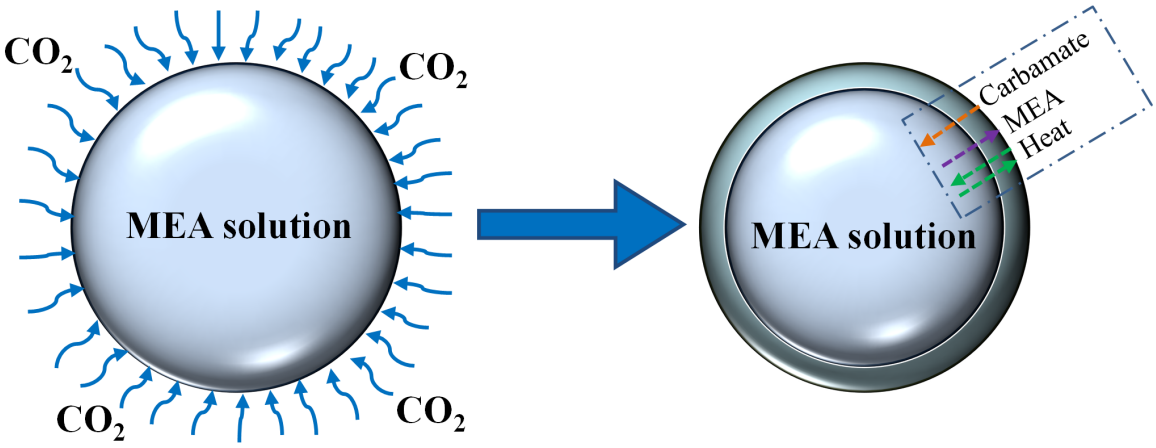

Figure 2.3: The interaction between MEA aqueous droplet and CO_2

The schematic diagram in Figure 2.3 represents the interaction between MEA aqueous droplet and CO_2. The molecules diffusion from gas to liquid phases takes place at the interfacial area (droplet surface). Chemical reaction occurs starting at the surface of droplet to form carbamate which provided the heat generation. Consequently, a thin film of carbamate is created around the droplet which is a barrier of absorption process. Meanwhile, the diffusion and/or convection phenomena occur inside droplet due to the gradients of species (concentration) and/or temperature. Due to the exchange of molecules inside droplet, the available molecule of MEA can move to the surface and continue to capture CO_2. In this case, the competition between mass transfer and chemical kinetics needs to be taken into account. For heterogeneous system, a dimensionless number which was introduced by Shirôji Hatta known as "Hatta number" is used to give global characterization of the system taking into account the chemical reaction, however it is not devoted for the case of droplets. Therefore, the evolution of gas-liquid mass transfer/ chemical kinetics in droplets will be experimentally studied and quantified.

2.4 Optical characterization of droplets compositions and/or temperature

There are various optical techniques which can be applied to characterize thermophysical properties of droplets. Each technique provides different information and sensitivity permitting to select the most suitable technique for the studied system in order to obtain the required data. The droplet compositions and/or temperature can be characterized by using Raman scattering, laser-induced fluorescence, thermographic phosphors (laser-induced

phosphorescence), rainbow technique etc., therefore the basic principle of each technique is described as followed.

- **Raman scattering** [38–41]

  This technique is based on inelastic scattering which the net exchange of energy between photons and molecules result to have the increase or decrease of molecules' vibrational or rotational energies. Raman spectrum is represented by plotting intensity versus frequency shift which is traditionally measured as wavenumber (cm^{-1}). The position of the peak is unique for each set of molecules structure. The peak intensity is linearly proportional to the number of molecules (species concentration). In addition, the spectral shape is also sensitive to the change of temperature. However, the measurement of multicomponent droplets needs to have the sufficient separation spectrum between substances and high enough concentration. Also, the intensity of Raman scattering is weak, therefore a powerful laser is necessary. In the particular case of spherical droplet, morphology-dependent resonances (MDRs) can be occurred which strongly affects to Raman spectrum. Therefore, the signal interpretation needs to take into account both liquid properties and droplet size which is more complicated.

- **Laser-Induced Fluorescence (LIF)** [39]

  This technique is widely utilized for visualization and quantitative measurement to access droplet temperature. Fluorescent dye needs to be added into droplets in order to observe the luminous intensity which is a result of emission of photons from the excited molecules. In practical, there are a lot of factors which can influence on the fluorescence intensity, such as local laser power, tracer concentration, tracer temperature etc. Accordingly, the use of intensity ratio from different bandwidths of wavelength can eliminate the undesirable factors permitting to measure the temperature. However, the fluorescent dye needs to be carefully selected as it can affect droplets properties (e.g. composition, pH etc.). Moreover, the calibration is needed to obtain the correlation between the intensity ratio and temperature which is used for signal interpretation.

- **Thermographic phosphor** [39]

  Thermographic phosphor is a temperature measurement technique which has the same basic principle as laser-induced fluorescence. Inorganic phosphors forming as fine powders with the size in micro range are made of a host material doped with a small amount of an activator (rare earth compound). This activator forms the luminescent centers where the excitation-emission process of phosphor takes place. In order to perform the measurement with droplets, the phosphors needs to be dispersed into liquid before the injection. The intensity ratios from different bandwidths of wavelength are obtained to determine the corresponding temperature. However, the correlation between the intensity ratios and temperature is required from the calibration which can be heavy procedures as it must be performed under well controlled conditions.

It apparently appears that there are few techniques to apply for the measurement of composition or temperature. Raman scattering is able to apply for both measurements. However, the intensity of signal is very weak, moreover MDRs must be taken into account for the signal analysis in the case of spherical droplets. On contrary, LIF and thermographic phosphors are applied to the temperature measurement. These techniques are indirect methods as the additive substance is used to be the tracer which referred to the

droplets temperature. However, it needs to carefully select additive substance as it could modify liquid properties. According to this study, the evolution of CO_2 capture by MEA droplets involves the chemical reaction, thus the rainbow technique is selected due to no any additives needed. Additionally, the intensity of signal is stronger than Raman scattering since this technique is based on elastic scattering. The rainbow signal provides the measurement of refractive index which is an intrinsic property of liquids related to both composition and temperature. Accordingly, the basic principle including some previous research works on rainbow technique are provided in the section 2.5.

2.5 Rainbow technique

2.5.1 History of rainbow

In 1637, rainbow phenomenon was geometrically explained by René Descartes who applied the law of reflection and refraction (known as Snell–Descartes law) to describe the path of light in raindrops [42]. From his study, the position of rainbow angle was demonstrated without the explanation of rainbow color and supernumerary bows. The rainbow color was realized due to the experiment of Newton in 1666 which represented the effect of light dispersion [42]. This shows that refractive index also depends on wavelength. However, the intensity of light distribution was unable quantified by geometrical optics. Accordingly, a principle of wave propagation was applied taking into account diffraction effect by George B. Airy in 1838. The intensity of light distribution around rainbow region was expressed known as "Airy function" [42] which the droplet size was also taken into account. Airy theory satisfies to describe the first peak of rainbow, however it still has an error at the higher order of supernumerary bows.

Later, in 1908, the exact solution of Maxwell's equations was solved by Gustav Mie [43]. It is known as Lorenz-Mie theory used to describe light scattering of a spherical particle by taking into account all kinds of interaction of light with droplet. In 1909, Peter J.W. Debye also proposed another solution permitting each kind of light interaction to be independently quantified [6]. The order of each kind of light interaction is denoted in Figure 2.4 which the index represents the number of path's light inside droplet.

- Order 0 (p=0) is external reflection rays.
- Order 1 (p=1) is the rays with two times refraction.
- Order 2 (p=2) is the rays with one time internal reflection and two times refraction.

Both solutions (Mie's solution, Debye's solution) are infinite series which requires long computations. In 1969, Nussenzveig [42] developed Debye series by applying the modified Watson transformation (Complex Angular Momentum). Analytical solutions nearly as accurate as Mie's solution were proposed with faster computational time.

2.5.2 Characteristic of rainbow signal

The normalized light distribution around rainbow angle is computed in the framework of Lorenz-Mie theory and plotted versus the scattering angle from 132° to 150° displayed in Figure 2.5. This signal is simulated according to a droplet size 100 μm with refractive index equal to 1.333 for the incident wavelength 0.589 μm. The low frequency on rainbow signal consisting of main peak of rainbow and supernumerary bows is created by the interference between one time internally reflected rays (p=2). Rainbow signal also includes a high frequency called "ripple structure" created by the interference between one time internally

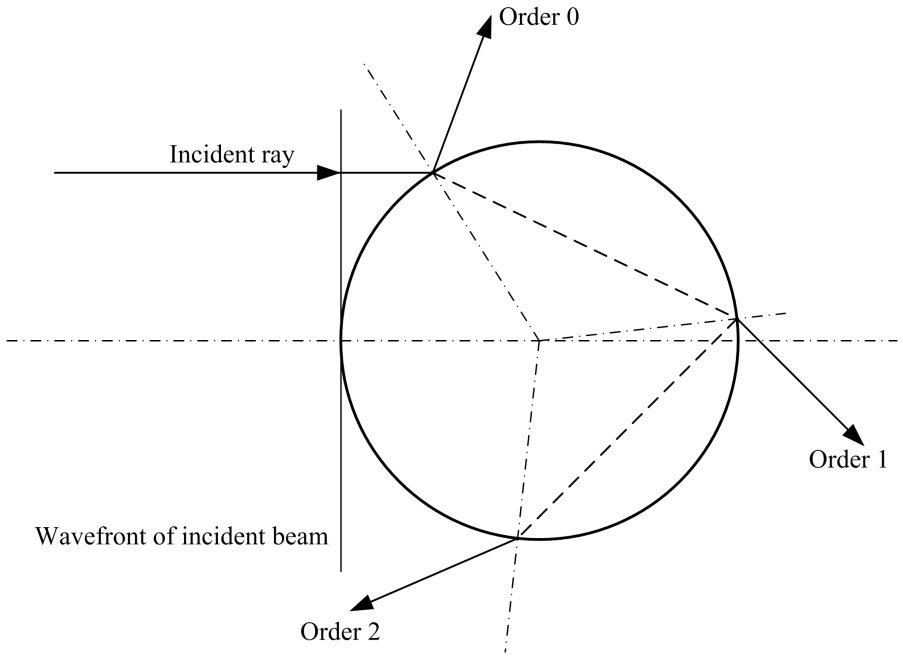

Figure 2.4: The path of light in a spherical droplet (modified [5])

reflected rays (p=2) and other kinds of interaction of light with particle, but mainly the externally reflected rays (p=0).

The simulated rainbow signals at refractive index equal to 1.371 and 1.397 with 100 μm of droplet size are compared in Figure 2.6. It is found that the rainbow signal is shifted toward the larger scattering angle when refractive index increases. Figure 2.7 is the simulated rainbow signals corresponding to droplet size equal to 100 μm and 150 μm for refractive index equal to 1.371. It is found that the rainbow structure is larger for the smaller droplet size. Therefore, it can be concluded that refractive index is obtained from rainbow position and droplet size from rainbow structure. Moreover, the higher accuracy of this information is able to obtain if the ripple structure is considered [43].

2.5.3 Research background on rainbow measurement

Roth et al. [5,44] were the first research group employed the rainbow technique to measure size and temperature of monodisperse droplet under the burning condition. The rainbow angle was observed and quantified to follow the evolution of droplet temperature according to refractive index variation. The droplet size was measured independently from fringe spacing in forward region (scattering angle between 30° to 80°).

Van Beeck et al. [45] performed the experiment of single free falling droplet with diameter in the range of millimeters (1 mm to 5 mm). In the study, the droplet size was obtained from the fringe spacing of supernumerary bows and droplet temperature was extracted from the fitting between measured and computed signal based on Airy theory. However, it was found that the non-spherical droplet affects to rainbow position resulting in the error on the obtained temperature. Accordingly, Global Rainbow Technique (GRT) was proposed by van Beeck et al. [46] in order to avoid the effect of droplet shape. This technique is available for measuring the average refractive index of droplets crossing the control volume which is typically 1 mm^3. In this case, the ripple structure disappeared due to the superposition of light distribution of different droplet sizes [44].

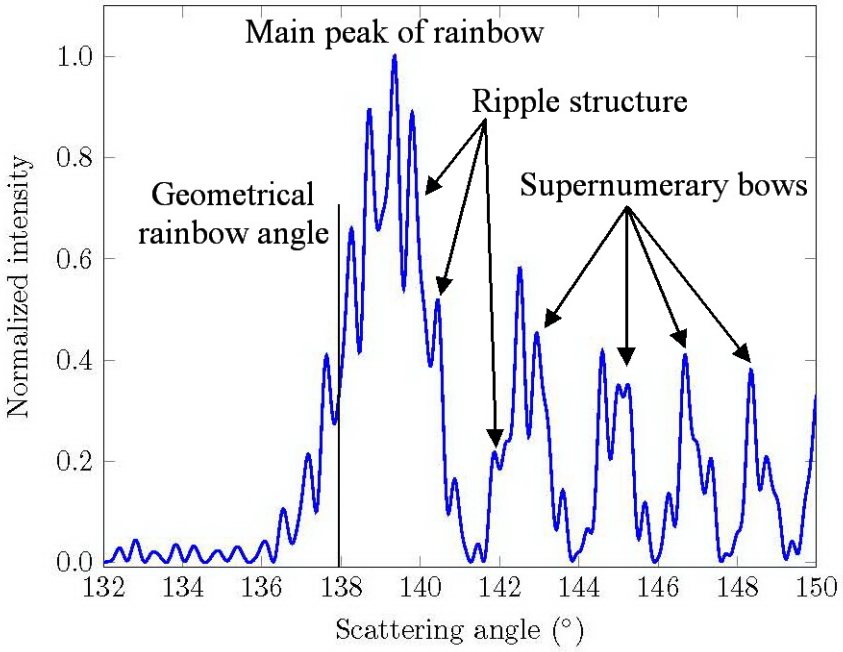

Figure 2.5: Characteristic of rainbow signal computed in the framework of Lorenz-Mie theory for λ=0.589 μm, n=1.333, d=100 μm (modified [6])

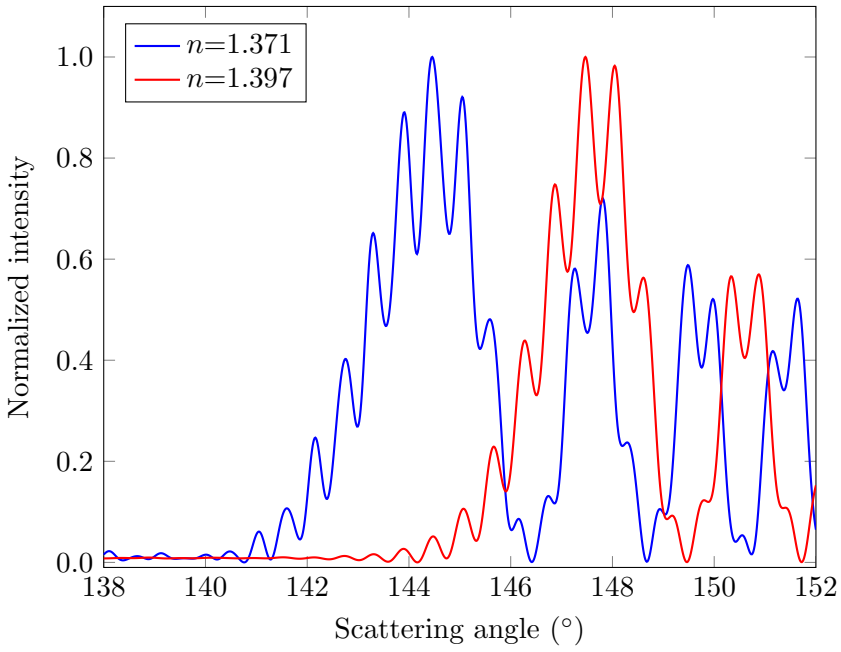

Figure 2.6: Rainbow signals with different refractive index values (λ=0.589 μm, d=100 μm)

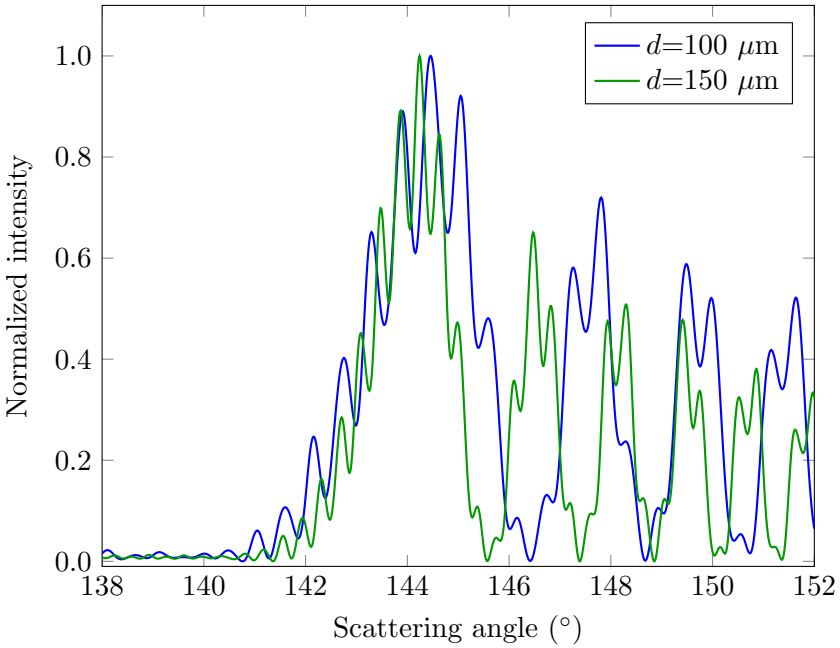

Figure 2.7: Rainbow signals with different droplet sizes (λ=0.589 μm, n=1.371)

Later, Saengkaew [6, 43] developed rainbow technique to study on both individual droplet and a cloud of droplets. A new inversion algorithm based on Nussenzveig theory was proposed. This approach provided accurate data comparable to Lorenz-Mie theory with the computation as fast as Airy theory [6]. The automatic inversion code of the recorded rainbow signals was achieved permitting to process individual or a series of recorded signals in order to extract refractive index and drop size distribution. Moreover, this algorithm is able to work with and without considering the ripple structure.

Rainbow technique is a non-intrusive method able to work with both monodisperse droplets and polydisperse droplets (a cloud of droplets) without additives. Accordingly, this technique is applied in order to access droplet temperature and/ or composition, for example the study on droplet evaporation [47], the measurement of spray composition [4, 48], and temperature measurement of spray under the burning condition [49].

2.6 Refractive index sensitivity for CO_2 capture by MEA30%wt

Refractive index is used to characterize the droplet properties in this study. This physical property is sensitive to both temperature and composition. The reaction between CO_2 and MEA30%wt simultaneously affects to temperature and composition of droplets. The heat creation increases the temperature resulting in the decrease of refractive index while refractive index is higher according to the quantity of CO_2 absorbed. Therefore, the sensitivity of refractive index on temperature and concentration is recognized.

Refractive index at different CO_2 loaded was reported in the study of Ouboukhlik [4]. The values are represented in Figure 2.8. MEA30%wt solution with different CO_2 loaded was prepared and measured refractive index by a refractometer in the temperature range 10°C to 40°C. It was found that the variation of refractive index about 0.002 representing the temperature change about 10°C and it can demonstrate the variation of CO_2 concentration about 0.2 mol/L. The values as presented in Figure 2.8 are fitted to determine a correlation on both temperature and CO_2 concentration which is then used to quantify CO_2 absorbed in the analysis part for this study.

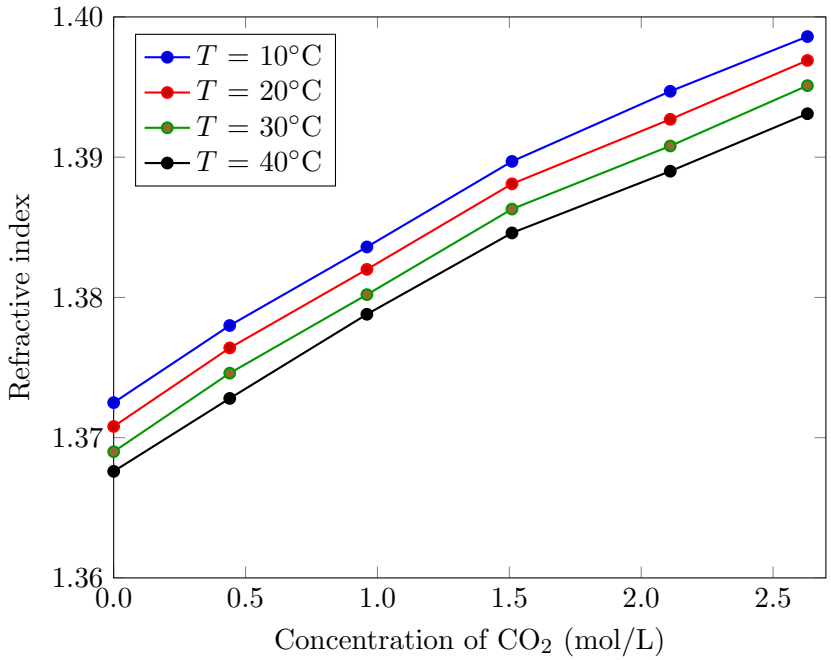

Figure 2.8: Refractive index values with different CO_2 concentrations in the temperature range 10°C to 40°C [4]

2.7 Chapter summary

Different optical techniques using for characterization of droplet compositions and/or temperature were described. Rainbow technique is selected to be a non-intrusive tool to trace the evolution of CO_2 absorbed by MEA droplets. Up to now, rainbow technique is limited to apply with homogeneous droplets i.e. uniform refractive index in droplets, therefore it will be extended to the droplet with gradients in Chapter 3.

CHAPTER 3

Refractive index gradients

This chapter is divided into four main parts. Refractive index gradients and its effect on rainbow measurement are described in the first section. Then, the literature review of previous studies on droplets with gradients by different optical techniques are available in the second section. Later, the simulation of rainbow signals for a multilayered spherical droplet with radial refractive index gradients is presented in the third section. The characteristic of droplet model as well as the used assumptions, simulation process, and the results are indicated. Additionally, the selecting method of coefficient b to evaluate the gradient profiles is described. Then, the chapter summary is provided in the last section.

3.1 Refractive index gradients

According to the research activities as discussed in section 2.5.3, all cases studied which rainbow technique was employed to quantify droplet temperature or composition were applied based on the assumption of homogeneous droplet. However, non-homogeneous droplets are able to be occurred in transient state of the real reactive systems such as combustion, condensation, evaporation, and CO_2 absorption leading to the gradients of temperature and/or composition. For example, if a cold droplet is injected to a hot environment, the whole droplet cannot instantaneous warm. It takes time to warm from the surface to the center. Similarly, if a chemical reaction takes place with droplets, it also takes time to completely react. As spatial properties of droplet are non-uniform, consequently the light path inside droplet is altered which can affect to optical measurements. Therefore, the effect of gradients on rainbow measurement is discussed in this study.

Schematic diagrams of path's light produced by homogeneous and non-homogeneous droplet are demonstrated in Figure 3.1a, 3.1b. The light paths of homogeneous droplet and non-homogeneous droplet are represented as solid line and dashed line, respectively. Figure 3.1a displays a non-homogeneous droplet where the refractive index at the surface is greater than at the center of droplet ($n_s > n_c$). This phenomenon can be found in the systems of evaporation, condensation, and CO_2 absorption. The increase of refractive index at the droplet surface is induced by the decreasing temperature (evaporation and condensation) and the increasing quantity of carbamate (the chemical product due to MEA reacting with CO_2). From Figure 3.1a, it was found that rainbow angle is shifted to smaller angle when the refractive index at the surface is greater than at the center of droplet. In contrast, a non-homogeneous droplet where the refractive index at the surface is less than at the center of droplet ($n_s < n_c$) was shown in Figure 3.1b. This phenomenon can occur in the combustion or heating systems. The decrease of refractive index at the surface is caused by the increase of surrounding temperature. In this case, it was found that rainbow angle is shifted to larger angle as shown in Figure 3.1b.

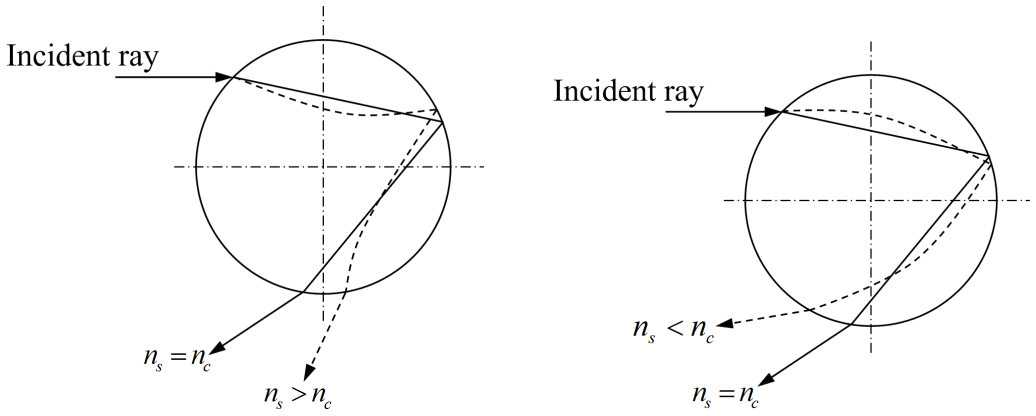

(a) $n_s > n_c$ (b) $n_s < n_c$

Figure 3.1: The path of light in a spherical droplet with radial refractive index gradients (modified [7, 8])

In addition, the effect of gradients in droplets has been presented in several research works both numerical and experimental approaches. For numerical research works, the extension of light scattering for radially non-homogeneous sphere was demonstrated. Kai and Massoli [50] proposed a finely stratified sphere model to describe scattering of electromagnetic-plane waves by non-homogeneous droplet which it was later used to study the fluctuations of rainbow positions during the heating and cooling processes by Kai et al. [7]. Moreover, Generalized Lorenz-Mie theory (GLMT) was also extended for multilayered sphere by Onofri et al. [51] permitting to deal with arbitrary incident beams. Later, Wu et al. [52] provided an improvement of the algorithm which was first introduced by Wu and Wang [53] to compute light scattered by multilayered sphere. The modification of rainbow signals due to the effect of refractive index discontinuity inside droplet was demonstrated. Airy theory was also extended for more general case of non-homogeneous droplet by Vetrano et al. [8]. The extended approach was applied to an inversion algorithm for the case of burning droplets with the assumption of parabolic refractive index profiles to quantify refractive index at the center and at the surface of droplet [54]. Furthermore, rainbow measurement for droplets with gradients was numerically studied by Saengkaew et al. [55]. It was found that the rainbow created by non-homogeneous particle is always fitted with rainbow created by homogeneous particle, which equivalent refractive index and equivalent size were obtained.

From aforementioned of the numerical research works, it is able to conclude that the existence of refractive index gradients inside droplets affects to interpretation of recorded rainbow signals. Then, some of experimental research works on droplets with gradients are presented in section 3.2.

3.2 Previous studies on droplets with gradients

According to the previous experimental studies, several techniques were employed to quantify the gradients inside droplets.

In 1996, the first study was presented by Anders et al. [56] who observe the influence of temperature gradients under the burning condition of monodisperse droplets. Geometrical optics was exploited to determine the evolution of rainbow positions which the experimental and theoretical results were qualitatively compared.

In 1998, Richards et al. [57] also studied temperature gradients in a convectively cooled droplet using thermochromic liquid crystal (TLC) thermography. The micro-encapsulated beads with diameter range 5 μm to 15 μm were diluted into distilled water to act as tracer particles permitting to visualize the transient temperature inside droplet. The droplet with diameter 1 mm was suspended and placed in a jet of dry air. Then, a heated coil was briefly inserted to the jet flow upstream of the droplet to create a step change in temperature. A sequence of images taking from the recorded video was used to analyze the temperature in a cooling droplet. The droplet image was divided into 100 μm square subregions to determine the average temperature of each subregion. Then, it was used to calculate the volume-average temperature in droplet for each image. Therefore, the temperature variation in a cooled droplet was obtained in order to interpret heat transfer information.

In 2006, Laurent et al. [58] studied thermal gradients of cooling and burning droplets. Two techniques which are rainbow refractometry and laser induced fluorescence (LIF) were combined in their study. A line of monodisperse droplets (size $\approx$ 100 μm) was used. The measurements were done on ethyl alcohol and acetone droplets with different injection temperatures at ambient pressure for cooling or burning conditions. Two measured temperatures were obtained, LIF provided a mean temperature while rainbow refractometer offered an equivalent temperature. A hypothesis of parabolic temperature profile inside droplet was applied in order to characterize the temperature at the droplet surface and the temperature at the droplet center. Then, the results were compared to a numerical prediction which the good tendency was obtained.

In 2006, the measuring temperature gradients in evaporating alcohol/water droplets were performed by Hopkins et al. [59]. Two techniques which are LIF and cavity enhanced Raman scattering (CERS) were combined. LIF was used to investigate volume averaged temperature whereas the near-surface temperature was determined by CERS. However, both techniques cannot be applied simultaneously, thus the experiment was separately performed in common conditions. A line of monodisperse droplets with the initial diameter $<$ 120 μm was injected in a chamber. Dry nitrogen was flowed through the chamber to refresh the gas surrounding of the droplets. The pressure inside chamber was maintained to be 7 kPa and 77 kPa to perform the measurements. For CERS measurement, the spectrum which encompasses both regions of CH and OH frequencies was collected from the outer shell of alcohol/water droplets over the evaporation times (0.22-2.33 ms). Accordingly, the intensity ratio of spectrum which is confined by CH molecules to OH molecules permitted to realize the change of composition at droplet surface. In addition, the spectrum which is limited by OH molecules demonstrated the decreasing temperature due to the evaporation. For LIF measurement, Rhodamine B was added into the droplets in order to be a temperature tracer. The bandwidth of fluorescence spectrum was observed to extract the volume averaged temperature over the period of 0 to 12 ms. Then, the quasi-steady state model was used to compare with the measured results. The predicted values were in agreement with the measured values from CERS while the disparity of the temperature predicted by the model and measured by LIF suggests that substantial temperature gradients can exist with evaporating droplet.

Recently, in 2016, Rosebrock et al. [60] also performed a study of temperature gradients in droplets under the burning condition. In the study, rainbow technique was applied coupled with Interferometric Particle Imaging (IPI). IPI was separately used to measure the droplet size while the maximum positions of the first two peaks of rainbow signals were extracted. Then, the measured results were compared to the combustion models by taking into account the temperature dependent on physical properties and the decrease of droplet size in order to evaluate temperature profiles inside droplet.

It can see that different techniques i.e. LIF, thermochromic liquid crystal thermography, CERS, and rainbow technique were exploited to characterize gradient in droplets qualitatively and quantitatively. However, the quantitative studies combined two techniques in order to evaluate the gradient in droplets. Therefore, in this study, only rainbow technique is proposed to characterize droplets during CO_2 absorption process expecting to observe and quantify the existence of gradient.

3.3 Simulation of rainbow signals for a multilayered spherical droplet with radial refractive index gradients

3.3.1 Multilayered sphere model and the used assumption

A droplet is assumed to be multilayered sphere as illustrated in Figure 3.2. Each layer has its refractive index which is denoted as n_1, n_2,..., n_i. The distribution of refractive index along droplet radius or gradient profile is described by equation (3.1) [55].

$$n(x) = n_c + (n_s - n_c) \times \left(\frac{e^{bx} - 1}{e^b - 1} \right) \tag{3.1}$$

where: n_c : refractive index at the center of droplet
n_s : refractive index at the surface of droplet
b : a coefficient that controls gradient profiles
x : dimensionless radius

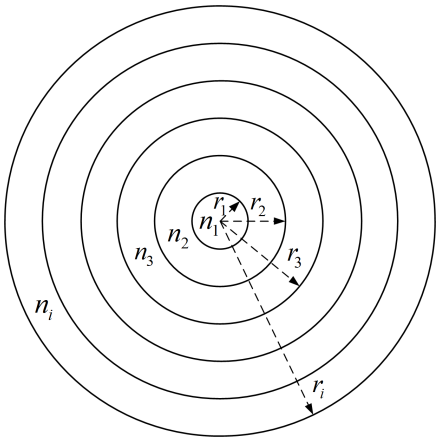

Figure 3.2: Multilayered sphere model

In the simulation, the droplet size equal to 100 μm similarly to the size in the experiment was used. The number of layer was selected to be 128 in order to provide continuous refractive index variation inside droplet. The coefficient b was varied from -100 to 100 with an increment equal to 1. Considering the chemical reaction between MEA and CO_2, refractive index increased due to the modification of droplet composition and at the same time decreased due to the increasing temperature. As the heat creation is a consequence of the reaction process, thus it will be considered as the second effect and subsequently investigated. Accordingly, the simulation was done by assuming as the isothermal droplet with a temperature about 20°C. Assuming that the reaction is taken place at the surface of droplet, the created product i.e. carbamate moves toward the center of droplet while MEA moves from the center toward the surface of droplet. Therefore, the case of greater refractive index at the surface than at the center of droplet is considered. The

simulation is presented as three cases. All cases was assumed that the center of droplet is unaffected i.e. there is no refractive index variation at the center of droplet. Since a MEA solvent at 30%wt is used in the experiment, thus refractive index at the center of droplet (n_c) was defined as refractive index of MEA30%wt which equals to 1.371 at $T = 20°C$. On the other hand, refractive index at the surface of droplet (n_s) was varied depending on the ability for the created carbamate at droplet surface. The increase of refractive index varies with the amount of CO_2 absorbed, however refractive index of fully CO_2 absorbed (1.397 at $T = 20°C$) is a limit. Therefore, the refractive index values equal to 1.374, 1.385, and 1.397 were used as refractive index at surface (n_s). These three values correspond to refractive index of MEA30%wt which absorbed CO_2 about 11%, 54%, and 100%, respectively.

3.3.2 Simulation process

1. All required parameters were already defined in section 3.3.1 i.e. droplet size, coefficient b, refractive index at the center (n_c) and at the surface of droplet (n_s), number of layers. These parameters were applied to equation (3.1) and computed by Matlab providing the refractive index distributions as a series of text files corresponding to the values of coefficient b. Examples of refractive index distribution along dimensionless droplet radius are shown in Figure 3.3. The distributions were simulated from refractive index at the center and at the surface equal to 1.371, 1.397 respectively. These values correspond to refractive index of MEA30%wt and MEA30%wt with 100% of CO_2 loaded. Red and blue solid lines represent refractive index distributions when b is negative and positive values respectively. It was found that the gradient is steep at the center of droplet when b is negative while the gradient is steep at the surface of droplet for positive value of b. Moreover, refractive index distribution is linear when b equal to zero which is represented by black solid line.

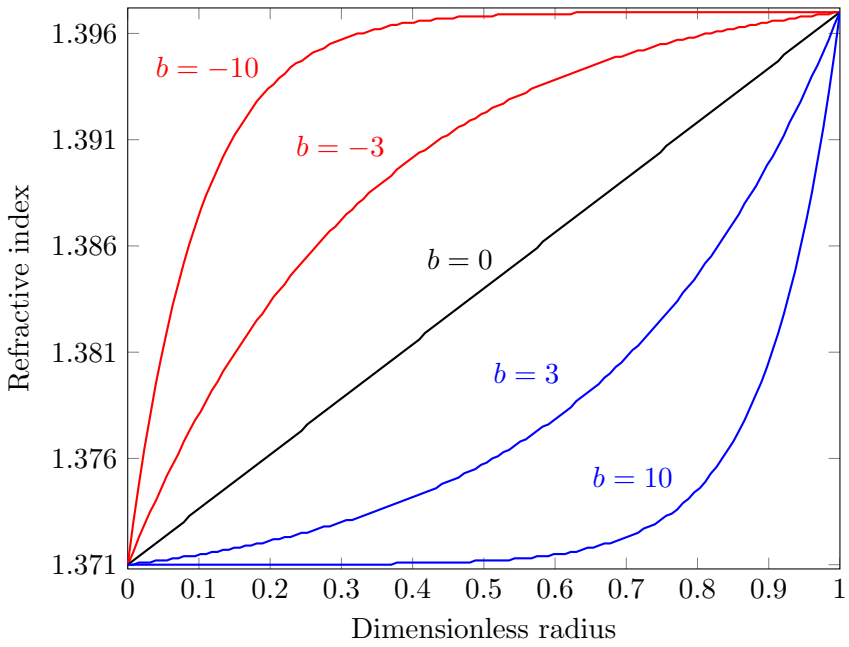

Figure 3.3: Examples of refractive index distribution along dimensionless droplet radius or gradient profiles, where $n_c = 1.371$, $n_s = 1.397$, 128 layers

2. The series of refractive index distributions was applied to a code provided by Gréhan. This code was used to simulate rainbow signals which were computed in the framework of Lorenz-Mie theory for multilayered sphere. Additional parameters i.e. incident wavelength, scattering angle range, and number of point on simulated signal are required. The incident wavelength equal to 0.589 μm was used, this value is identical as in the experiment. The rainbow signals were simulated in the range of scattering angle from 139° to 151° with the number of points on the signal equal to 1024. These configuration parameters were used for all simulated signals. Then, the rainbow signals corresponding to each refractive index distribution were exported as another series of text files.

   An example of simulated rainbow signal for droplet with a gradient (n_c=1.371, n_s=1.397, b=10) was compared to the rainbow signals created by homogeneous droplet (n=1.371 and n=1.397) in Figure 3.4. From this example, the rainbow signal created by droplet with gradient departs from the range of the rainbow signals of homogeneous droplet. An angular shift toward the lower scattering angle was observed representing the decrease of refractive index. This particular behavior represents a signature of gradient in droplet.

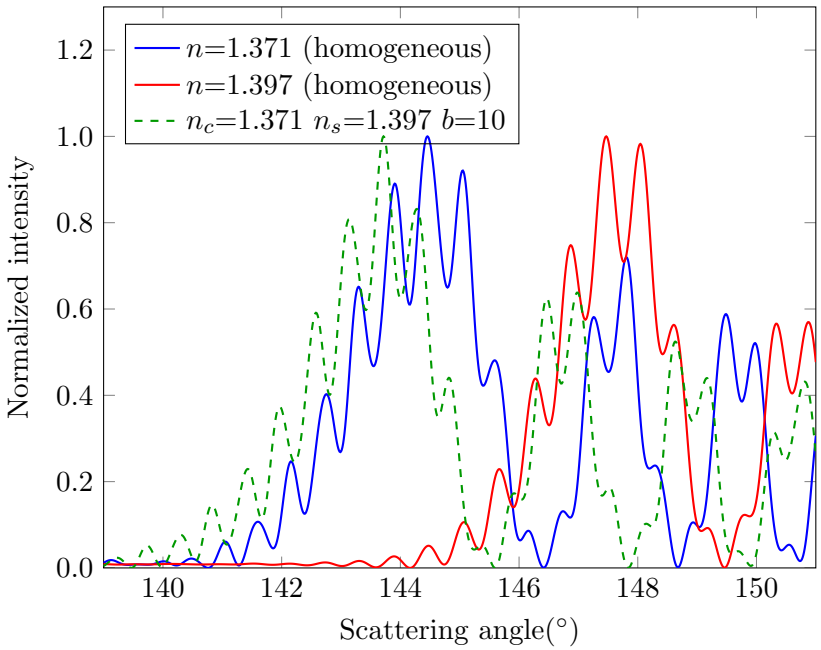

Figure 3.4: Comparison of simulated rainbow signals created by droplet with and without gradient where an angular shift toward the lower scattering angle is observed from the rainbow signal created by the droplet with gradient.

3. The computed rainbow signals based on Lorenz-Mie theory were considered as the prediction of rainbow signal obtaining from the experiment which can be called "recorded rainbow signal". Then, an inversion code which was developed by Saengkaew [6] was used. The inversion code computed the rainbow signal in the framework of Nussenzveig theory under the assumption of homogeneous spherical droplet in order to search for the best fit of the recorded rainbow signal. Therefore, equivalent refractive index and equivalent droplet size are defined as the refractive index and size of the homogeneous droplet creating a rainbow which is the best fit of the rainbow created by the droplet with a refractive index gradient. To use the inversion code,

the following parameters must be defined; scattering angle range, diameter range, incident wavelength, the number of point on the signal, and number of droplets. Finally, the rainbow signals were fitted without taking into account the ripple structure to obtain the equivalent refractive index and equivalent droplet size.

4. The first three steps were repeated when the couple of refractive index at the center and at the surface has been changed.

3.3.3 Equivalent refractive index and equivalent size

According to the work of Saengkaew et al. [55], it has been proved that the rainbow signal produced by non-homogeneous droplet can be always fitted by rainbow signal of homogeneous droplet. For example, the rainbow signal of non-homogeneous droplet where coefficient b equals to 10, n_c is 1.371 corresponding to refractive index of MEA30%, n_s is 1.397 corresponding to refractive index of MEA30%wt with fully CO_2 loaded is plotted as the green dashed line in Figure 3.9. The black solid line represents the rainbow signal of homogeneous droplet corresponding to the equivalent refractive index (n_{eq}) 1.3647 with equivalent size (d_{eq}) 100.1 μm, which provides the perfectly fit with the non-homogeneous one. These two rainbow were computed in the framework of Lorenz-Mie theory. It can be seen that the rainbow signal cannot be distinguished whether there is a gradient or not. However, the equivalent refractive index in this case provides the value where is outside the range of n_c and n_s. Therefore, this particularity will be exploited in this work. On the other hand, equivalent size is very close to the simulated size which cannot extract more information, thus only equivalent refractive index is focused in this study.

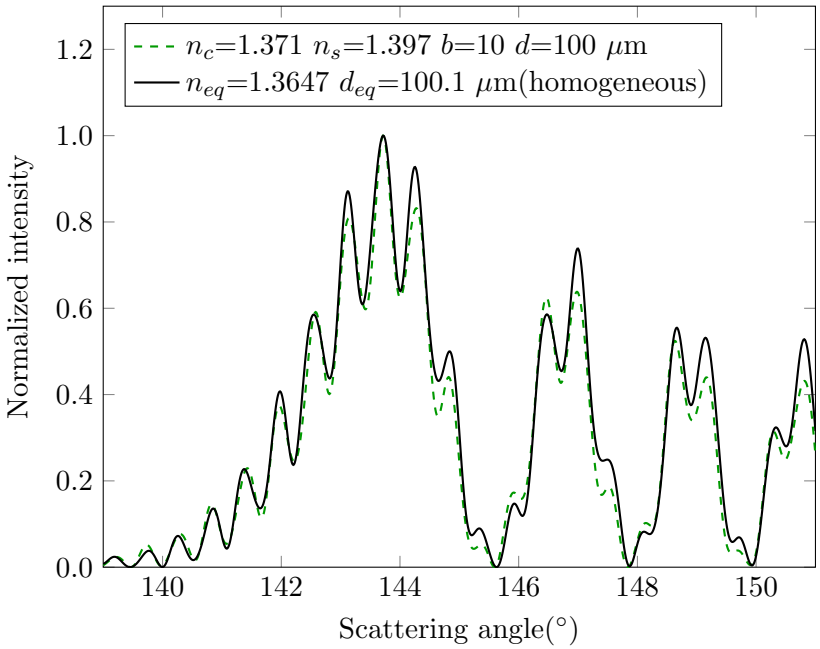

Figure 3.5: Rainbow signal of non-homogeneous droplet is perfectly fit by rainbow signal created from homogeneous droplet, providing an equivalent refractive index and equivalent size

3.3.4 Simulation results

In the simulation, for one droplet size (100 μm) where refractive index at the surface is 1.397, equivalent refractive index values from 200 rainbow signals corresponding to coeffi-

cient b from -100 to 100 were extracted and plotted as blue in Figure 3.6. If the refractive index at the surface is changed to be 1.385 and 1.374, the equivalent refractive index values for coefficient b from -100 to 100 are plotted as green and red in Figure 3.6. From these curves, four different parts are observed. First corresponds to coefficient b about 30 to 100, the equivalent refractive index is essentially constant corresponding to the value of refractive index at the center. This part belongs to strong gradient at the surface, but the gradient is thin. In second part, the equivalent refractive index decreases and increases, the value is less than refractive index at the center. This part corresponds to coefficient b about 2 to 30 where the gradient is large and strong at the surface. Then, equivalent refractive index strongly increases in the third part, corresponding to the coefficient b close to zero. In the fourth part, the coefficient b is negative. The equivalent refractive index is constant close to the value of refractive index at the surface. This part belongs to the strong gradient at the center. In addition, equivalent refractive index is also affected by the difference of refractive index at the center and surface of droplet. The minimum value of equivalent refractive index for b positive is lower when the difference between refractive index at the center and surface of droplet is greater. This characteristic will be used in the analysis part in order to estimate refractive index at the surface of droplet.

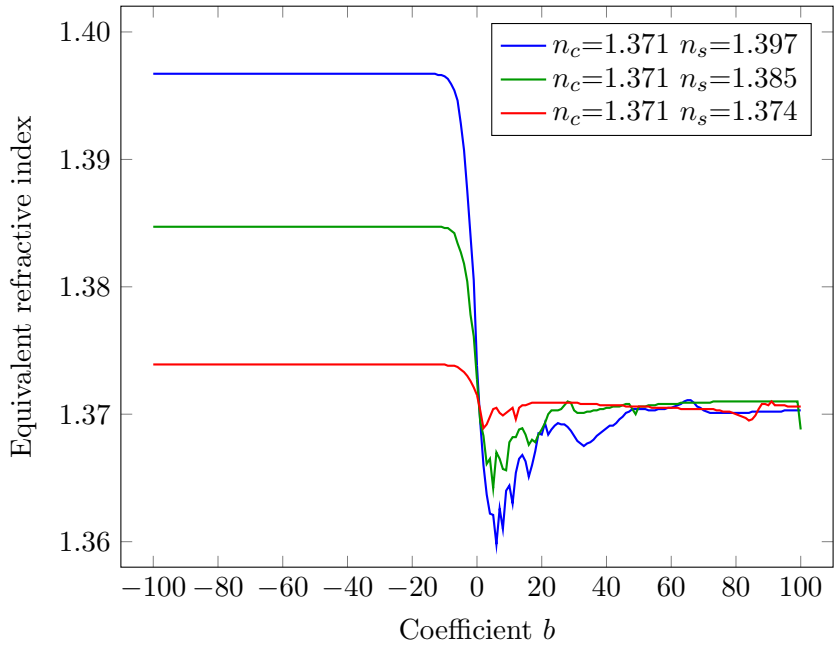

Figure 3.6: Equivalent refractive index values extracted from the simulated rainbow signals (d=100 μm), the values were less than refractive index at the center and at the surface where the gradient is large and strong at the surface.

Moreover, the fluctuation of equivalent refractive index was found in the case of b positive as shown in Figure 3.6, this behavior could be caused by the interference effect. Accordingly, the simulation was recomputed by varying droplet size from 100.00 μm to 100.30 μm with an increment equal to 0.02 μm to observe fluctuated behavior. The patterns of equivalent refractive index fluctuation for droplet size 100.0 μm, 100.1 μm, 100.2 μm, and 100.3 μm in the case of n_c=1.371, n_s=1.374 are illustrated in Figure 3.7. It was found that fluctuation of equivalent refractive index is shifted as periodic i.e. the fluctuation pattern is shifted with a change of droplet size and returns to be the same pattern when the droplet size is changed about a half of the incident wavelength (0.3 μm). Therefore, equivalent refractive index values were averaged from droplet size 100.00 μm

to 100.28 μm (14 values) in order to obtain the main behavior which is plotted as black dashed line in Figure 3.7. However, the average curve is still rough, therefore it will be fitted to obtain the smooth curve, as represented in red dashed line. It means to construct one dashed line as plotted in Figure 3.8, 2800 rainbow signals need to be computed and processed.

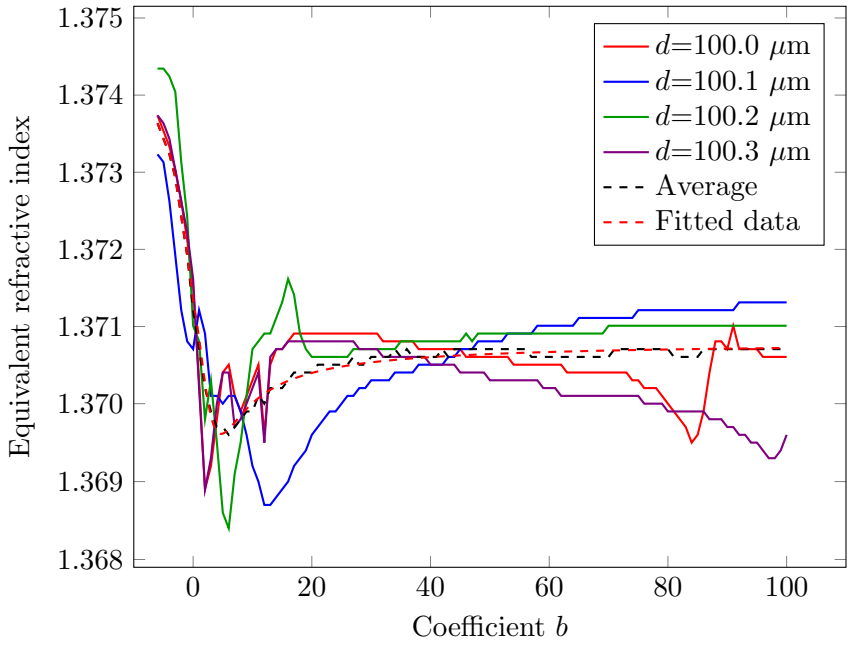

Figure 3.7: Equivalent refractive index values are periodic when the droplet size has been changed about 0.3 μm, thus the equivalent refractive index values were averaged to obtain the main behavior (case: n_c=1.371, n_s=1.374).

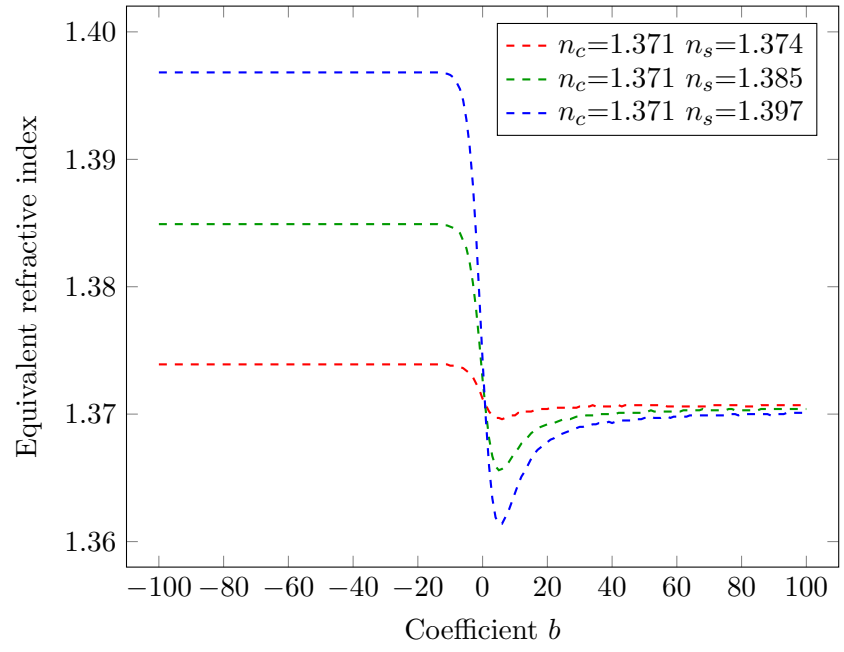

Figure 3.8: Equivalent refractive index values obtained from droplet size 100.00 μm to 100.28 μm (14 values)

3.3.5 Selecting method of coefficient b to evaluate gradient profile according to equivalent refractive index

After refractive index at the surface of droplet is estimated, the numerical and experimental results will be compared in order to evaluate the gradient profiles. Thus, it is necessary to consider how a corresponding gradient profile can be selected. Figure 3.9 shows equivalent refractive index corresponding to the different gradient profiles where n_c=1.371, n_s=1.374, obtained from the simulation. For example, if equivalent refractive index equals to 1.372, a value of coefficient b denoted as b_1 in Figure 3.9 corresponding to a gradient profile is obtained. However, some equivalent refractive index values e.g. 1.370 provide two values of b denoted as b_2, b_3 in Figure 3.9 which corresponds two different gradient profiles. Therefore, in order to avoid this complicated situation, the assumption that the reaction takes place at the surface, and then diffuses to the center is used. It means the coefficient b decreases when the measurement position is farther.

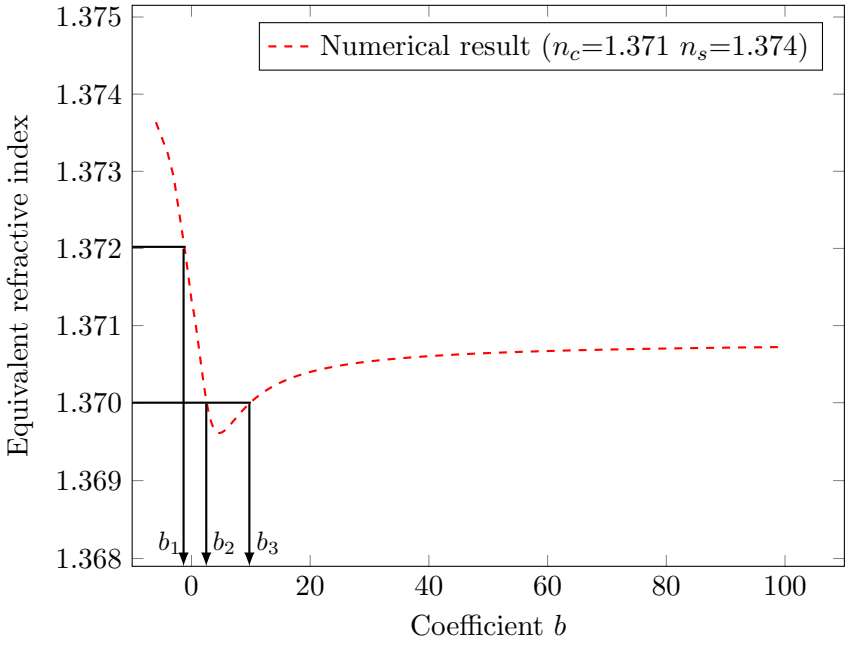

Figure 3.9: Examples of the selecting coefficient b according to the equivalent refractive index represents that equivalent refractive index can provide two values of b i.e. two gradient profiles. Thus, the selection of b is based on the assumption that the droplet is pure MEA30%wt from the beginning. Then, the reaction takes place at the surface, and diffuses to the center i.e. b decreases at farther position.

3.4 Chapter summary

The simulation of rainbow signals for a multilayered sphere was done to predict the rainbow signals. The equivalent refractive index was extracted based on the assumption of homogeneous droplet. It was found that equivalent refractive index was affected by the gradients inside droplet which was obvious when the gradient is large and steep at the surface corresponding to coefficient b about 2 to 30. The equivalent refractive index values departed from any physical values, this characteristic is a signature of gradients in droplet.

CHAPTER 4

Rainbow measurement on a suspended droplet

This chapter is divided into seven parts, presenting the rainbow measurements on a suspended droplet. The experimental setup for a suspended droplet and the preparation of reactive liquid (MEA30%wt) are indicated in the first, second section, respectively. Then, the optical setup as well as the calibration system for rainbow technique are described in the third section. The operating conditions and experimental method are provided in the fourth section. Later, the processing of experimental data is demonstrated in the fifth section, where determinations of refractive index and droplet size are illustrated. The sixth section is the experimental results. Then, the chapter summary is provided in the last section.

4.1 Description of experimental setup for a suspended droplet

The overview of the suspended system is represented in Figure 4.1. A plastic tube connecting with a manual syringe was used to create a suspended droplet with the size in range of 2-3 millimeters. The suspended droplet was located inside a transparent chamber size 250 mm $\times$ 250 mm $\times$ 500 mm which can be adjusted in three axes (left-right, forward-backward, upward-downward). There are two gas inlets on the side, a gas outlet on the top, and a liquid outlet at the bottom of the chamber. The gas inlets permit to create gas flow inside chamber, then it can be flowed out from the top of chamber in order to conserve the pressure inside chamber to be atmospheric. The bottom of chamber is connected to a ball valve where the used solvent can be drained from the chamber. The volume flow rate of N_2 and CO_2 were controlled by the identical model of gas flow meter (Brooks Sho-Rate, model: 1355G (R-6-15-A: Glass). MEA aqueous solution was used as a solvent in the experiment, therefore the preparation of solution is described in section 4.2.

4.2 Preparation of MEA aqueous solution by weight

In order to prepare MEA aqueous solution, the chemical product ethanolamine ($\geq$ 99% purity) was dissolved into distilled water to obtain the solution at the desired concentration. As the MEA aqueous solution with concentration 30% by weight (MEA30%wt) was used in the experiment, thus it was prepared according to the definition of concentration by weight as given in Equation (4.1). For example, MEA30%wt 1000 g is obtained when ethanolamine 300 g dissolved in water 700 g.

$$\text{Percent by weight of solute} = \left(\frac{\text{weight of solute}}{\text{weight of solution}}\right) \times 100 \tag{4.1}$$

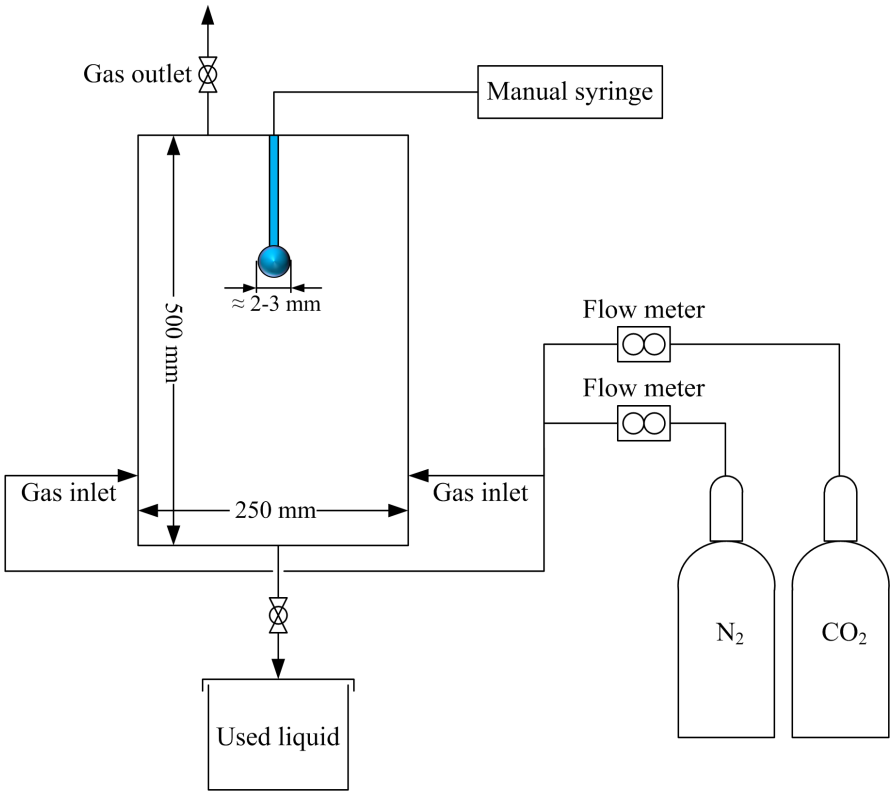

Figure 4.1: Schematic diagram of experimental system for a suspended droplet

4.3 Description of optical adjustment and calibration system for rainbow technique

Since the rainbow technique was applied to characterize droplet properties, thus the explanations of optical adjustment as well as the calibration system are provided. The setup of the optical components including with the optical alignment are detailed in section 4.3.1, whereas the calibration system is described in section 4.3.2. The optical adjustment and calibration system for a suspended droplet and a line of moving monodisperse droplets are based on the same basic principle. Only some optical components are added or suppressed.

4.3.1 Optical adjustment

The real setup of rainbow system as shown in Figure 4.2 combines two main parts which are emission part and detection part. Emission part consists of a continuous laser with wavelength 0.589 μm (Shanghai Dream Lasers, Model: SDL-589-050T, Power: 61 mW, laser beam diameter $<$ 1.5 mm). A diverging lens was added for the experiment of suspended droplet to provide fully illuminated on droplet. While detection part combines a plano convex lens (1^{st} lens: diameter 80 mm with focal length 160 mm) collecting the scattered light around rainbow angle and creating an image on a circular diaphragm size 2 mm and 4 mm (for the experiments of a line of moving monodisperse droplets), a biconvex lens (2^{nd} lens: diameter 100 mm with focal length 200 mm) creating an image from the focal plane of first lens on a semi-transparent screen which will be recorded by a CCD camera (Kappa, 1025 x 1373 pixel^2). These two main parts was located on an optical bench which is able to rotate and move in upward-downward directions. All optical components of emission and detection parts need to be aligned and adjusted to locate at the appropriate positions which are described as followed.

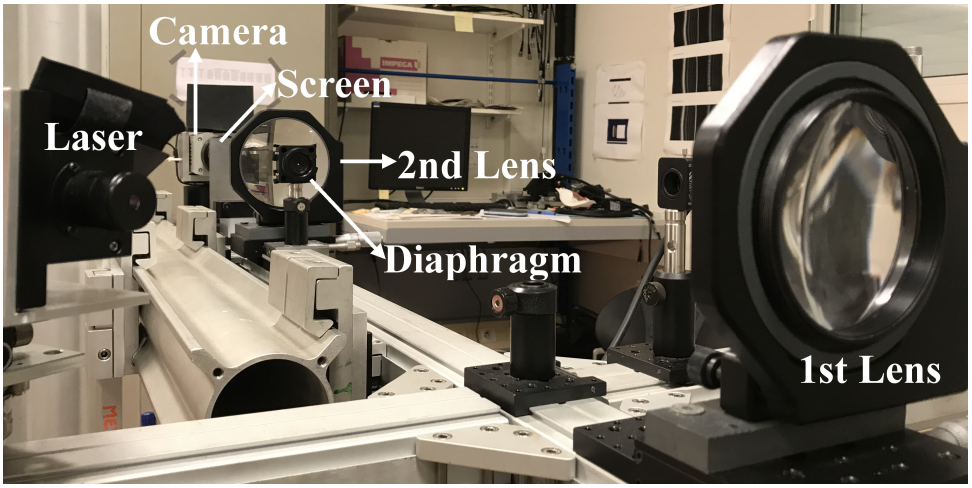

Figure 4.2: The optical system for rainbow measurement

- **Optical alignment**

  The laser was moved to the end of optical bench while three circular diaphragms which had already been adjusted to be the same level were placed on the identical bench. Then, the laser was adjusted until the laser beam passing through those circular diaphragms. This indicates that the laser beam was aligned with the optical bench. In addition, all optical components in the detection part were adjusted to be co-axial and perpendicular by using the laser beam one by one.

- **Optical position**

  In order to specify the position of each optical component, a thin wire was used as a reference object. The first lens can be placed at any positions, where the distance from the object is farther than its focal length in order to avoid virtual image creation. The first lens was illuminated by a white light in order to search for its focal plane where the brightest and smallest spot can be observed. Then, the clearly visible image of the wire is appeared at the image plane where the circular diaphragm is located. This diaphragm is used to limit the measurement area permitting to reject the scattered light coming from outside the control volume. Later, the second lens was mounted behind the diaphragm considering the scattered light on the focal plane of first lens as an object in order to create an image on the semi-transparent screen. To achieve this image position, a semi-transparent paper with marks was placed on the focal plane of first lens to search for the position where the mark obviously appeared on the semi-transparent screen. Finally, the camera was installed at the end of optical bench for recording the rainbow images.

4.3.2 Calibration system

The relationship between scattering angle and the pixels in the horizontal direction of image was obtained from a mirror calibration. A mirror was placed at the same position as the reference object which was specified in the section of optical adjustment. The mirror was installed on the rotation and linear translation stages permitting to rotate and move in upward-downward and left-right directions. The top view of calibration system is illustrated in Figure 4.3. In order to perform a calibration, the mirror was rotated with

an increment equal to 1° resulting in 2° on the recorded image. In addition, the rotation of mirror must be in the range that the reflected light can be collected by the first lens as well as passing through the circular diaphragm size 2 mm and 4 mm. Figure 4.4 displays a set of recorded images from a calibration presenting the reflection spots at different angles. The corresponding correlation of those images is demonstrated in Figure 4.5. However, the calibration must be performed when there is the modification on optical adjustment.

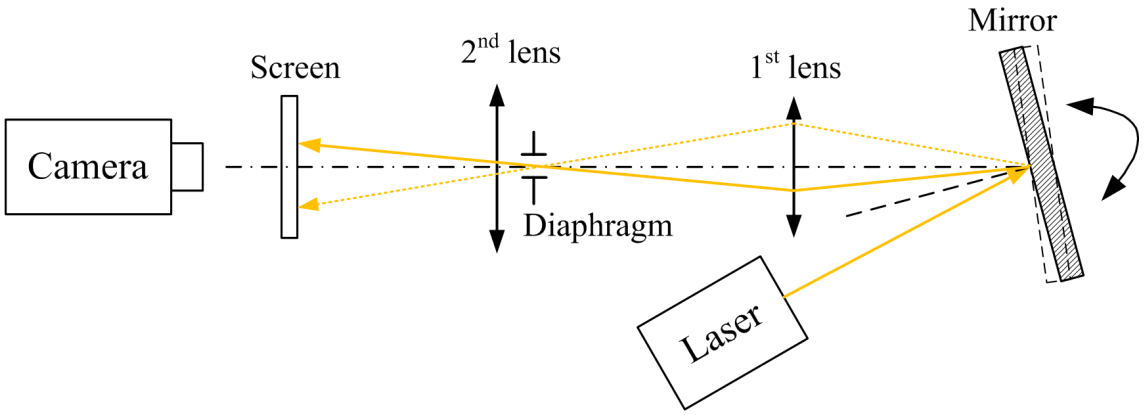

Figure 4.3: Top view of calibration system

Figure 4.4: A set of recorded reflected light for an angular calibration

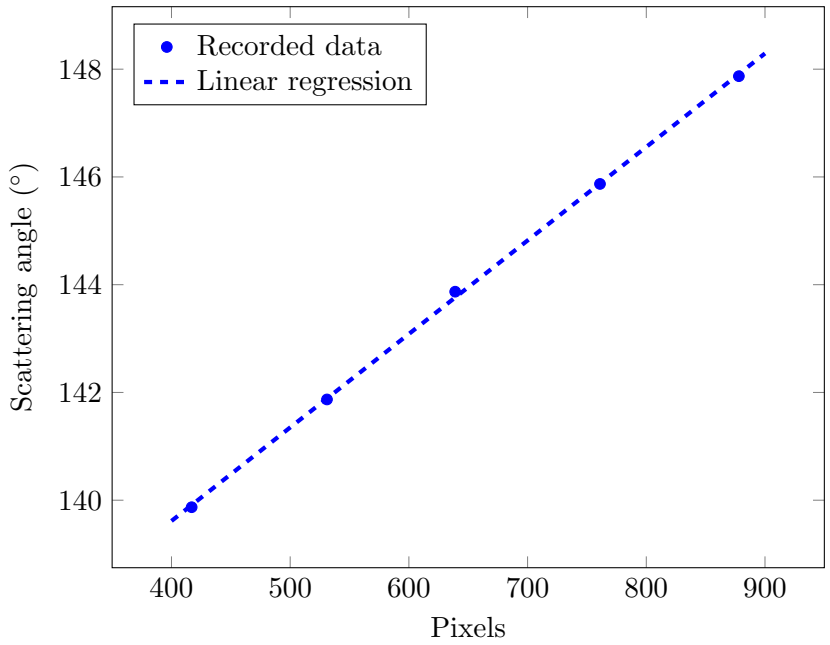

Figure 4.5: The extracted angular positions corresponding to Figure 4.4 and its linear regression.

4.4 Operating conditions and experimental method

4.4.1 Operating conditions

The experiment was performed at ambient temperature about 20°C under two conditions considering as long and short observation periods. Long observation period offers the investigation during 100 minutes of refractive index of MEA30%wt and pure MEA while short observation period demonstrates refractive index of MEA30%wt with different percentages of CO_2 volume flow rate for 2 minutes. The identical volume flow rate of gas approximately 5.6±0.1 L/min was applied for all measurements.

- **Long observation period: 100 minutes**

  Refractive index of MEA30%wt was measured under the conditions of stagnant ambient air and pure N_2 flow while refractive index of pure MEA was measured under the condition of pure N_2 flow. Series of rainbow images were recorded with 30 seconds of delayed time by a CCD Camera. In this measurement, an additional CCD camera was installed on the side of the chamber to observe the variations of droplet size by recording an image every 10 minutes. Accordingly, the evolution of droplet size can be quantified. Both cameras were separately operated which the images of droplet and rainbow signals were started to record after injecting droplet for 1 minutes and 1.5 minutes, respectively.

- **Short observation period: 2 minutes**

  Different percentages of CO_2 volume flow rate i.e. 100%, 50%, 30%, and without CO_2 were applied. Series of rainbow images were recorded for 2 minutes with a second of delayed time. The rainbow images were recorded prior injecting droplet, thus it was able to observe the signals since the droplet formation is completed.

4.4.2 Experimental method

The measurements for both conditions were done according to the following instructions.

- A MEA30%wt suspended droplet was created by a manual syringe and located in the chamber. To perform this step, the bubbles locating in the liquid line need to be vented prior starting the measurement in order to provide a stable suspended droplet.

- Then, the gas flow meter was adjusted to the desired value providing the gas flow to the chamber. For the second condition, the different ratios of CO_2 and N_2 volume flow rates were adjusted resulting in the different CO_2 concentrations. The mixing ratios for each case were illustrated in Table 4.1.

- A reference droplet was injected and adjusted until it was illuminated by the two laser beams at the cross sectional point, then a new droplet is injected. For the first condition, the images of droplet and rainbow images were started to record after the new droplet was injected. On the other hand, the rainbow images for the second condition were recorded before the new droplet is injected. The appearance of the new droplet was identified by the interruption of rainbow signal. Thus, the evolution of rainbow signals was able to be followed from the beginning of droplet formation. However, the rainbow signals after the complete droplet formation were only considered.

Table 4.1: The mixing ratios between N_2 and CO_2 used for the condition of short observation period

Case	N_2 flow rate (L/min)	CO_2 flow rate (L/min)	Total flow rate (L/min)
no CO_2	5.67	-	5.67
30% CO_2	3.92	1.58	5.5
50% CO_2	2.75	2.75	5.5
70% CO_2	1.58	3.92	5.5
100% CO_2	-	5.67	5.67

4.5 Processing of experimental data

4.5.1 Determination of refractive index

A recorded rainbow image of MEA30%wt droplet in pure N_2 flow was displayed in Figure 4.6, a stable rainbow pattern was obtained showing that the droplet was not perturbed by N_2 flow. From the image, seventy pixels from the middle part of image were selected to extract the normalized light distribution which was shown as the green solid line in Figure 4.7. Refractive index was extracted by searching for the best fit between recorded and computed signals using the inversion code. In Figure 4.7, a part of rainbow signal was selected representing by the yellow squares while the orange squares indicates the best fit of computed signal. It can be seen that the rainbow structure of computed signal was not well fitted since the inversion code is limited to use with the maximum droplet size 1 mm. Accordingly, only refractive index values obtained from the inversion code were focused. For the first condition, the evolution of droplet size was quantified by an additional method which will be described in section 4.5.2.

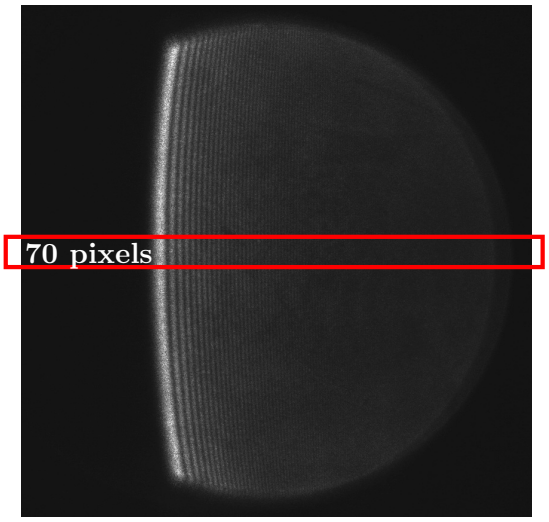

Figure 4.6: A recorded rainbow image of MEA30%wt droplet in pure N_2 flow. A stable rainbow pattern was obtained demonstrating the droplet was unaffected by N_2 flow.

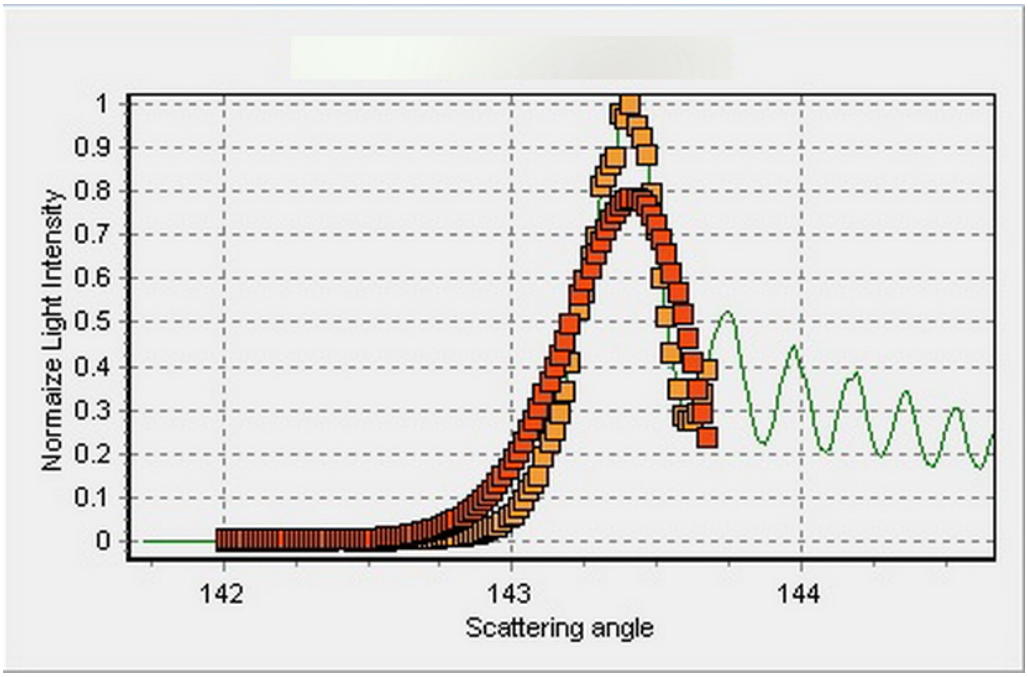

Figure 4.7: The fitting between recorded and computed rainbow signals obtained from the inversion code demonstrated the unfit rainbow structure due to the limitation of inversion code which is able to work with the maximum droplet size 1 mm.

4.5.2 Determination of droplet size from the image

In order to determine the droplet size from the recorded images, a calibration is needed. As the size of plastic tube is known, therefore it was used as a reference object providing a correlation between pixels and horizontal distance. Figure 4.8a illustrates an example of recorded image, then edge detection technique was applied to search for the boundary of the objects in the image as displayed in Figure 4.8b. The locating area of droplet as shown in Figure 4.8c was selected, then the maximum horizontal distance was determined to quantify the droplet size.

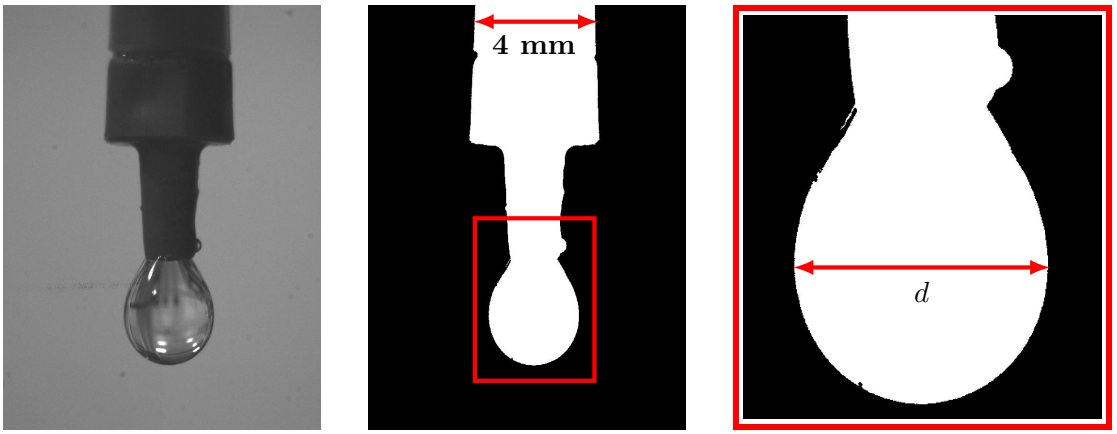

(a) Recorded image

(b) Boundary of objects in the image

(c) The maximum horizontal distance representing droplet size

Figure 4.8: An example of image processing for droplet size determination

4.6 Experimental results

The results were separated as two sections according to the experimental conditions. Refractive index and droplet size variations of MEA30%wt in stagnant ambient air, pure N_2 flow and pure MEA in pure N_2 flow were presented in section 4.6.1. Whereas the extracted refractive index values of MEA30%wt at different concentrations of CO_2 were provided in section 4.6.2.

4.6.1 The measurement of MEA30%wt in stagnant ambient air, pure N_2 flow and pure MEA in pure N_2 flow

Considering the cases of MEA30%wt in stagnant ambient air and MEA30%wt in pure N_2 flow in Figure 4.9, it was found that refractive index values increased versus the time, accordingly two possibilities were considered. The first possibility is the change of droplet position which was checked by moving the droplet in three directions (left-right, backward-forward, and upward-downward). It was found that the rainbow signal was unaffected by droplet position. The second possibility is the effect of evaporation. This assumption is reasonable if the droplet size decreases. The recorded droplet images of MEA30%wt in stagnant ambient air and pure N_2 flow were displayed in Figure 4.10, 4.11 where the evolutions of the droplet size were extracted and depicted in Figure 4.13. It was found that the droplet size decreased about 0.4 mm and 1 mm in stagnant ambient air, pure N_2 flow respectively. Therefore, the assumption of evaporation is acceptable.

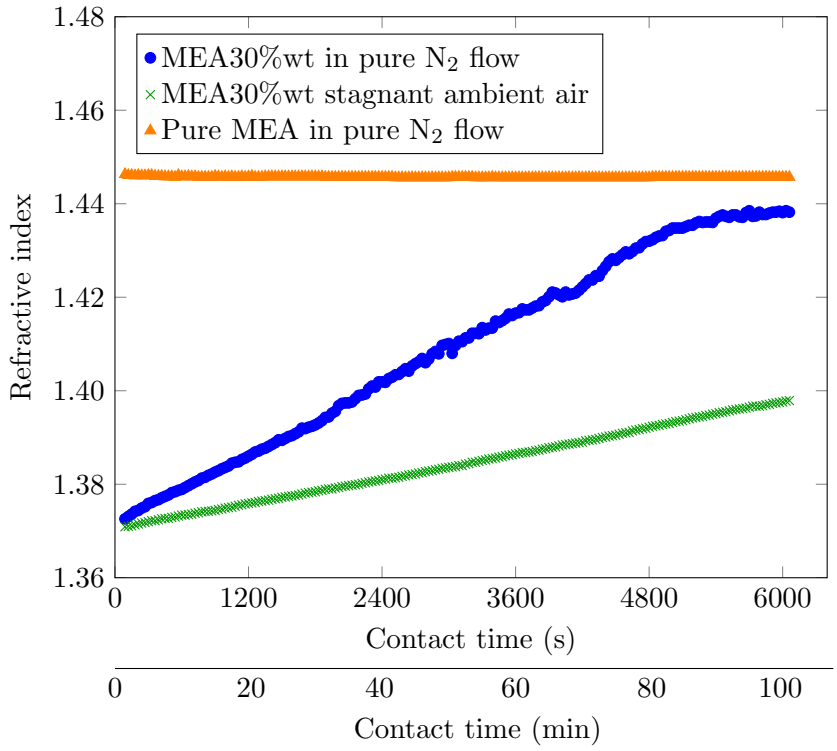

Figure 4.9: Refractive index of MEA30%wt in stagnant ambient air, pure N_2 flow and pure MEA in pure N_2 flow

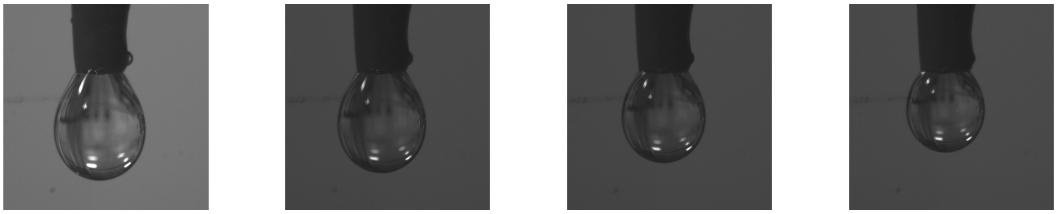

(a) 1 minutes (b) 30 minutes (c) 60 minutes (d) 100 minutes

Figure 4.10: MEA30%wt in stagnant ambient air

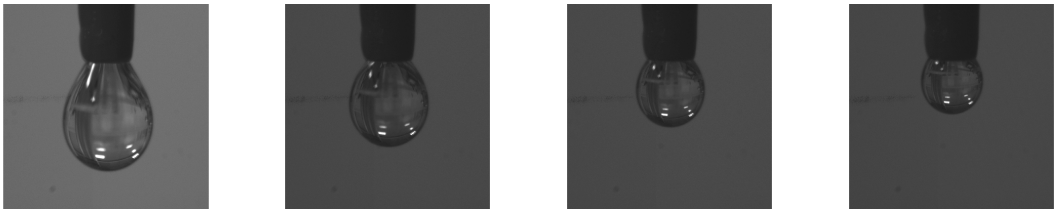

(a) 1 minutes (b) 30 minutes (c) 60 minutes (d) 100 minutes

Figure 4.11: MEA30%wt in pure N_2 flow

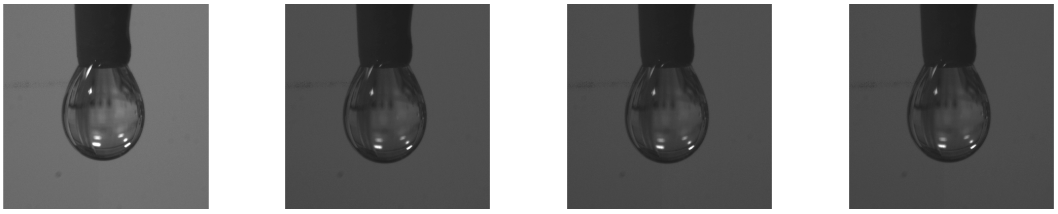

(a) 1 minutes (b) 30 minutes (c) 60 minutes (d) 100 minutes

Figure 4.12: Pure MEA in pure N_2 flow

In addition, the hypothesis of the evaporation of water component was considered. MEA30%wt is a binary mixture between water and ethanolamine, thus the evaporation of the substance which has higher vapor pressure could be expected. In this case, water (for $T = 20°C$; $P_{vapor} = 2.3392$ kPa [61], $T_b = 100°C$) has higher vapor pressure than ethanolamine (for $T = 20°C$; $P_{vapor} = 0.053$ kPa [62], $T_b = 170°C$), consequently refractive index increased due to the increasing MEA concentration. This can be confirmed by the investigation of refractive index and droplet size of pure MEA in pure N_2 flow. The obtained refractive index values for the case of pure MEA in pure N_2 flow were illustrated in Figure 4.9 while the recorded images and evolution of droplet size were displayed in Figure 4.12, 4.13, respectively. It was found that both refractive index and droplet size were stable along the measurement period. Therefore, it can be concluded that water is the main evaporating component in the cases of MEA30%wt in stagnant ambient air and pure N_2 flow. In contrast, there is no observable evaporation effect for the case of pure MEA in pure N_2 flow.

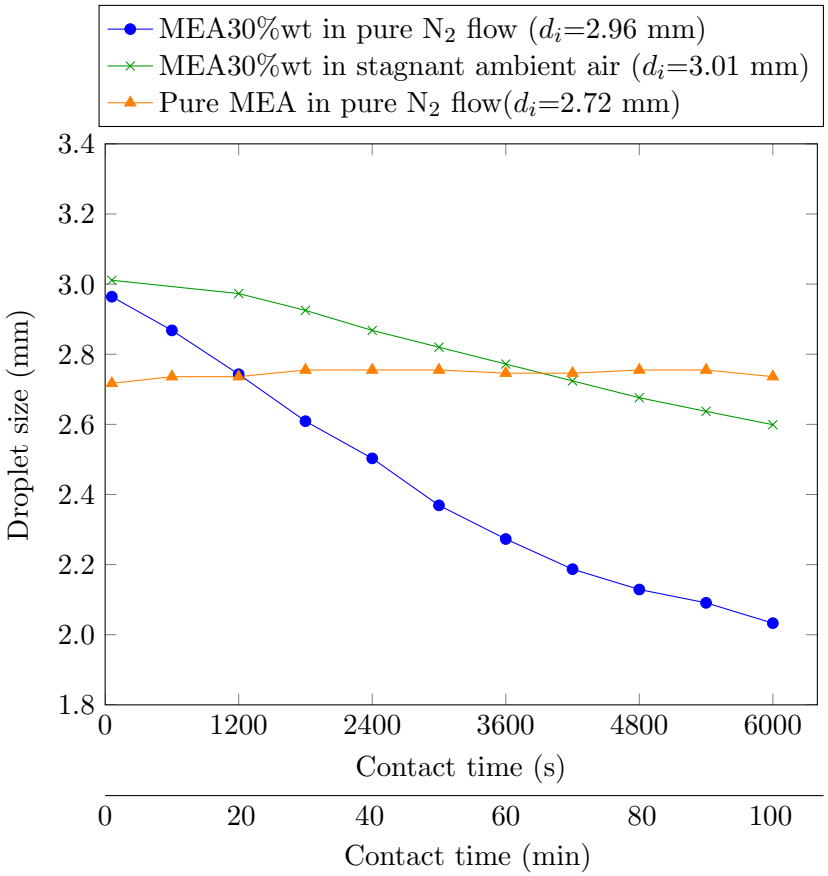

Figure 4.13: Droplet size of MEA30%wt in stagnant ambient air, pure N_2 flow and pure MEA in pure N_2 flow

4.6.2 The measurements of MEA30%wt at different percentages of CO_2 volume flow rate

This experiment was focused on the first two minutes since the beginning of injection expecting that the evaporation had not yet involved. The measurements were separated as five cases which are without CO_2, 30%, 50%, 70%, and 100% of CO_2 volume flow rate. The droplet formation time for each measurement was about 2-3 seconds. In these measurements, the processing of rainbow signals was only considered after the droplet formation was completed

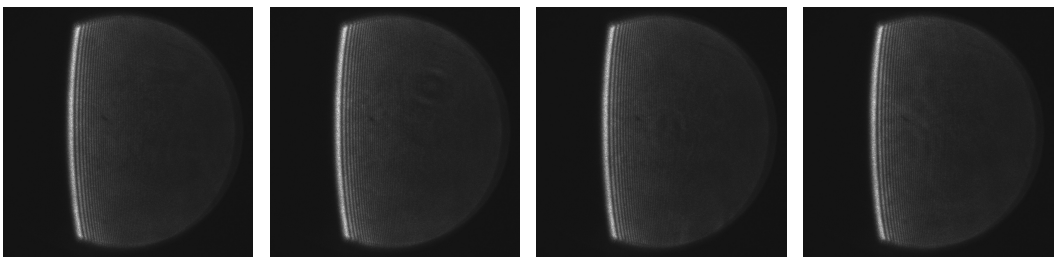

(a) 2 seconds (b) 10 seconds (c) 20 seconds (d) 90 seconds

Figure 4.14: Recorded rainbow signals of MEA30%wt without CO_2 flow (pure N_2 flow)

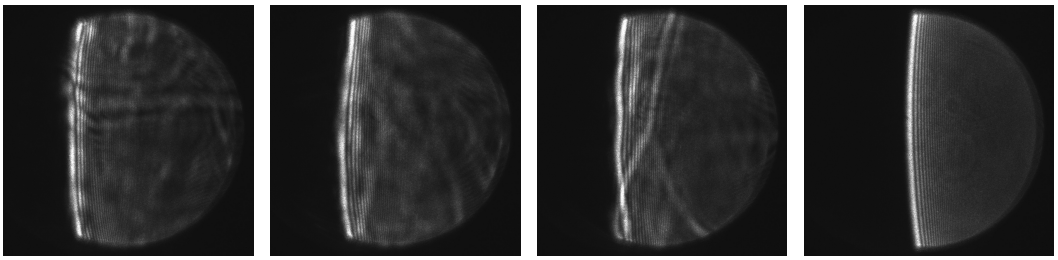

(a) 3 seconds (b) 10 seconds (c) 20 seconds (d) 80 seconds

Figure 4.15: Recorded rainbow signals of MEA30%wt with 30% of CO_2 and 70% of N_2

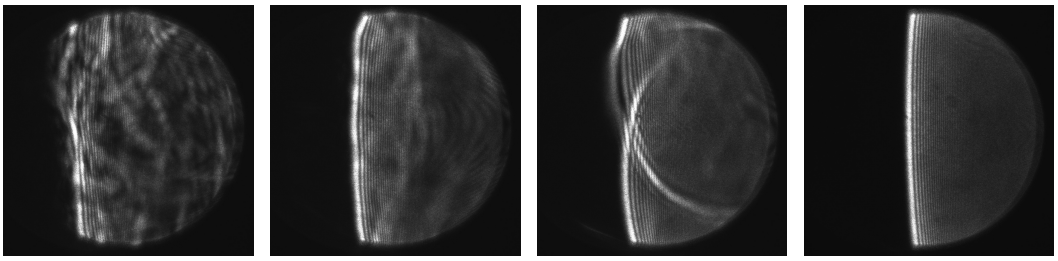

(a) 3 seconds (b) 10 seconds (c) 20 seconds (d) 45 seconds

Figure 4.16: Recorded rainbow signals of MEA30%wt with 50% of CO_2 and 50% of N_2

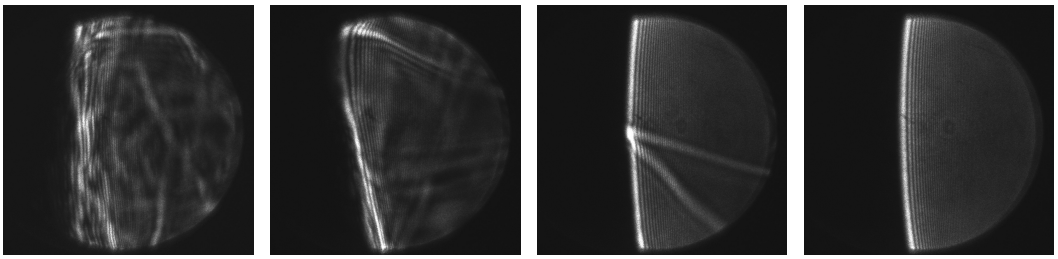

(a) 3 seconds (b) 10 seconds (c) 20 seconds (d) 31 seconds

Figure 4.17: Recorded rainbow signals of MEA30%wt with 70% of CO_2 and 30% of N_2

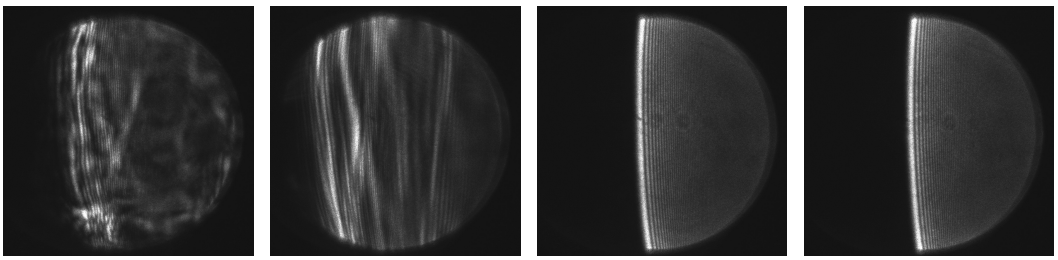

(a) 3 seconds (b) 10 seconds (c) 20 seconds (d) 30 seconds

Figure 4.18: Recorded rainbow signals of MEA30%wt with 100% of CO_2 (pure CO_2 flow)

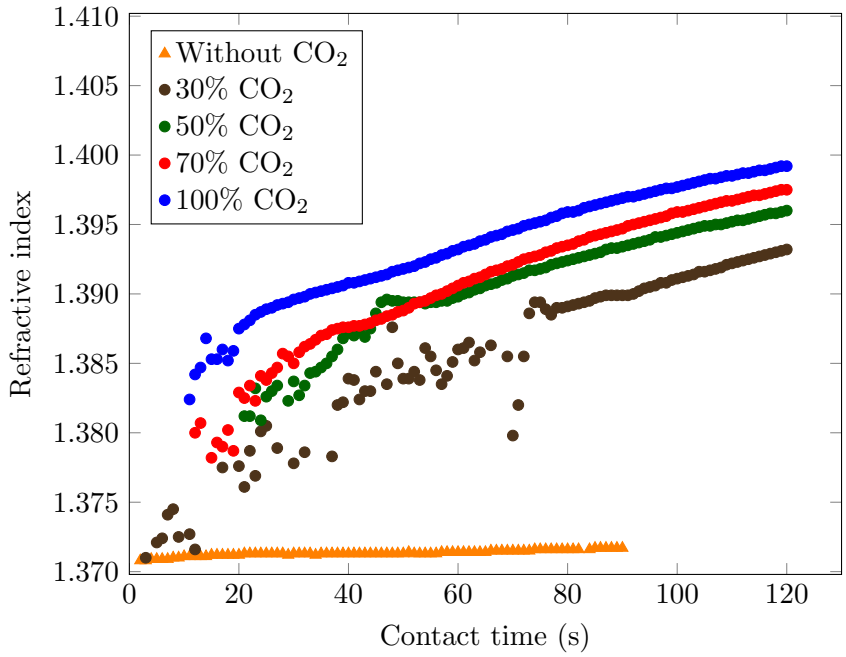

Figure 4.19: Extracted refractive index of MEA30%wt in the cases of without CO_2, 30%, 50%, 70%, and 100% of CO_2 (the total volume flow rate for all cases is 5.6±0.1 L/min)

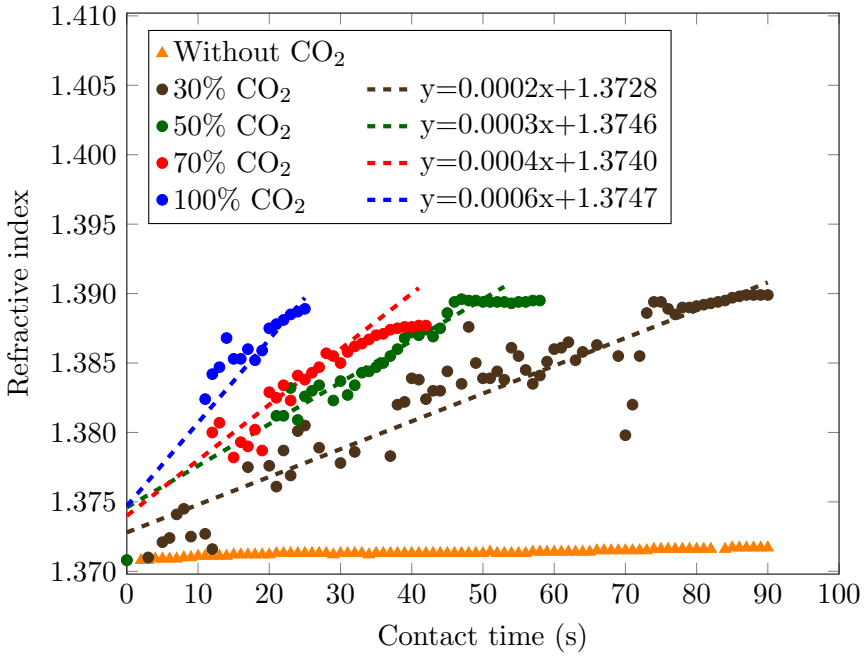

Figure 4.20: The slopes during the first period of measurement were quantified in the cases of MEA30% with 30%, 50%, 70%, and 100% of CO_2

The first case is the injection of MEA30%wt without CO_2 flow (pure N_2 flow). The recorded rainbow images at 2, 10, 20, and 90 seconds are displayed in Figure 4.14 where the well-organized rainbow patterns can be observed. On the other hand, the recorded rainbow images of MEA30% in the cases of 30%, 50%, 70%, and 100% of CO_2 flow demonstrated the disorganization on rainbow patterns as displayed in Figure 4.15, 4.16, 4.17, and 4.18, respectively. Consequently, the improper light distributions were obtained i.e. unable to identify the main rainbow peak and/or supernumerary bows, the asymmetry of rainbow pattern between upper and lower part. However, this behavior occurred for a period in each case depends on the concentration of CO_2. It was found that the well-organized rainbow patterns started at time 80, 45, 31, 20 seconds for the cases 30%, 50%, 70%, and 100% CO_2 flow, respectively. The variations of refractive index at different concentrations of CO_2 flow i.e. without CO_2, 30%, 50%, 70%, and 100% of CO_2 were plotted versus the time and illustrated in Figure 4.19. Refractive index values were stable along the measured time in the case of without CO_2 flow while other cases demonstrated the increasing refractive index versus the time. The stronger slope during the first period of measurement can be observed. In addition, the increase of refractive index during the first period provided different slopes for each case. Therefore, linear function was applied to quantify their slopes as shown in Figure 4.20. It was found that the strongest slope belonged to the case of 100% CO_2 flow and the smallest slope was the case of 30% of CO_2 flow. However, the variation of refractive index providing these different slopes obtained from the improper light distributions, consequently it is complicated to extract the correctly additional information. Therefore, the rainbow measurement on a line of moving monodisperse droplets is proposed in Chapter 5. Moreover, the droplet size in micro range close to the size in the real spray is obtained.

4.7 Chapter summary

In this chapter, the experimental setup including operating conditions for the measurements suspended droplet was described. In addition, the optical adjustment and calibration system of rainbow technique were indicated.

The rainbow measurements on suspended droplet were performed under two main conditions. For the first condition (measurement period: 100 minutes), the measurements of refractive index and droplet size were separated as three cases i.e. MEA30%wt in stagnant ambient air, MEA30%wt in pure N_2 flow, and pure MEA in pure N_2 flow. For the cases of MEA30%wt, it was found that the evaporation of water in MEA30%wt droplet induced to have the increasing refractive index due to the increase of MEA concentration in droplet. In contrast, there is no observable evaporation effect for the case of pure MEA in pure N_2 flow.

For the second condition (measurement period: 2 minutes), the experiment of MEA30%wt at different concentrations of CO_2 flow was carried out. From the recorded images, the disorganization of rainbow patterns due to the reaction between MEA and CO_2 affected the analysis of results. Accordingly, a line of moving monodisperse droplets with size in the range of 100 μm to 200 μm is proposed.

CHAPTER 5

Rainbow measurement on a line of moving monodisperse droplets

This chapter is organized as eight parts, presenting the rainbow measurements on a line of moving monodisperse droplets. The generating of a line of monodisperse droplets is described in the first section. In the second section, the preparation of reactive liquid with loaded CO_2 (MEA30%wt loaded CO_2) is provided. Refractive index of MEA30%wt unloaded and loaded CO_2 will be measured by refractometer and rainbow technique which are presented in the third, fourth section, respectively. Then, refractive index measurement on a line of moving droplets during CO_2 absorption process by rainbow technique is indicated in the fifth section. Later, the analysis of experimental results to evaluate the gradient profile inside droplets as well as the investigation of the quantity of CO_2 absorbed are demonstrated in the sixth section. The seventh section presents the improvement of refractive index gradients evaluation by considering the change at the center of droplets. Additionally, the chapter summary is available in the last section.

5.1 Generating of a line of moving monodisperse droplets

The generating of spherical droplet with constant size and stable rate is essential for the experiment of a line of moving monodisperse droplets. In this study, two droplet generators i.e. FMP technology, model: MTG-01-G2, and TSI Incorporated, model: 3450 were used to perform the experiments. The device from FMP technology was applied for the experiment in section 5.4 where the droplets were produced in downward direction. In contrast, the device from TSI Incorporated as depicted in Figure 5.1 was applied for the experiment in section 5.5 and produced droplets in upward direction. The TSI model offers a gas inlet directly connected to the droplet generator. In addition, it provides a cover permitting to create a small chamber, suitable for the experiment that needs the mixing between gas and liquid phases. The mechanism of generating droplets for both models is based on Rayleigh breakup of laminar fluid jet [9, 63]. The volume flow rate of liquid and excitation frequency are the controlled parameters to generate monodisperse droplets. The volume flow rate was controlled by a flow meter or a syringe pump to produce a liquid jet. A signal generator supplied a sine wave form amplitude 15 volts (from peak to peak: 30 volts) to excite the piezoelectric element which was connected to the droplet generator. Consequently, the liquid jet is disintegrated to be droplets according to the vibration of piezoelectric.

The volume flow rate and the range of excitation frequency were computed based on the diameter of orifice. Table 5.1 shows the volume flow rate of liquid injection and the operating range of excitation frequency for orifice sizes 50 μm and 100 μm which are used in the experiments. In addition, the discharge velocity of droplet and the expected droplet size are presented. It was found that the expected droplet diameter is about twice orifice size. The details of computation are given in Appendix B.1.

In practical, the bubbles in the liquid line could affect to the stability of liquid injection resulting in the unstable droplet creation, thus the bubbles need to be vented out prior starting the experiment. The stability of the line of droplets can be observed from the stable rainbow signal while the constant droplet size and spherical droplet shape can be indicated by the characteristics of rainbow pattern. The rainbow pattern for spherical droplet has a good shape i.e. no any distortion and the clear ripple structure can be obtained when the constant droplet size along the measured point is produced.

Table 5.1: The used volume flow rate, the operating range of excitation frequency, and the estimated range of droplet sizes for orifice sizes 50 μm and 100 μm

D (μm)	A_d (cm^2)	$\dot{V}$ (ml/min)	u (m/s)	Range of f (kHz)	Range of d (μm)
50	1.96×10^{-5}	0.6	5.1	$9.73 \leq f \leq 29.18$	$125.22 \geq d \geq 86.82$
100	7.85×10^{-5}	2.2	4.67	$4.46 \leq f \leq 13.37$	$250.44 \geq d \geq 173.65$
100	7.85×10^{-5}	2.3	4.88	$4.66 \leq f \leq 13.98$	$250.44 \geq d \geq 173.65$

* D is diameter of orifice, $\dot{V}$ is volume flow rate of liquid injection, u is discharge velocity of droplet, f is excitation frequency, d is droplet size, A_d is cross-sectional area of orifice

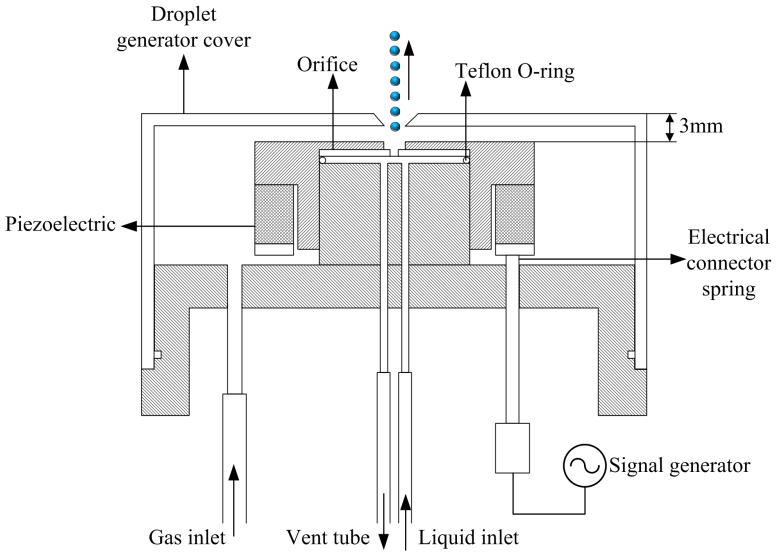

Figure 5.1: Cross sectional view of TSI Incorporated droplet generator, model: 3450 (modified, [9])

5.2 Preparation of MEA30%wt loaded CO_2

CO_2 was loaded to the prepared MEA30%wt by using a saturator. With this device, CO_2 can be directly flowed into the solution bottle. The solution was continuously stirred by a magnetic mixer to assist CO_2 absorbed. Recalling the equation of reaction (2.1), a half mole of CO_2 is able to be captured by a mole of MEA, where its ratio can be represented in equation (5.1). As the weight of MEA was known from the preparation step, therefore the expected weight of CO_2 absorbed can be computed according to equation (5.2).

$$\alpha = \frac{N_{CO_2}}{N_{MEA}} \tag{5.1}$$

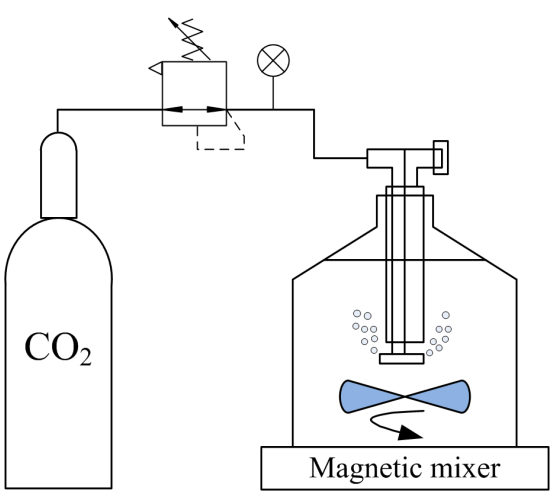

(a) Schematic diagram of CO_2 loaded system

(b) Real CO_2 loaded system

Figure 5.2: Preparation of MEA30%wt with loaded CO_2

$$\alpha = \frac{\left(\frac{m_{CO_2}}{M_{CO_2}}\right)}{\left(\frac{m_{MEA}}{M_{MEA}}\right)}$$

$$m_{CO_2} = \alpha \cdot \left(\frac{m_{MEA}}{M_{MEA}}\right) \cdot M_{CO_2} \tag{5.2}$$

where:
- α : mole ratio of CO_2 to MEA
- N_{CO_2} : mole number of CO_2 (mol)
- N_{MEA} : mole number of MEA (mol)
- m_{CO_2} : weight of CO_2 (g)
- m_{MEA} : weight of MEA (g)
- M_{CO_2} : molecular weight of CO_2 ($\approx$ 44 g/mol)
- M_{MEA} : molecular weight of MEA ($\approx$ 61.08 g/mol)

According to the computation, weight of MEA about 303.8 g was used to prepare MEA30%wt, thus CO_2 about 109.4 g can be absorbed. However, in practical, it was time consuming to reach the fully absorbed point ($\alpha = 0.5$), therefore CO_2 about 102.7 g was absorbed which corresponded to the ratio 0.47. The schematic diagram and the real CO_2 loaded system are displayed in Figure 5.2a, 5.2b, respectively.

5.3 Refractive index measurement by refractometer

In this section, the measurements of refractive index of MEA30%wt unloaded and loaded CO_2 were performed by using a refractometer.

The refractometer (Anton Paar, model: Abbemat 300) as displayed in Figure 5.3 was used to measure refractive index of the liquid samples. The working principle of this apparatus is based on the measurement of critical angle. This device is able to work during the refractive index range 1.26 to 1.72 and the temperature of liquid sample can be varied from 10°C to 85°C. Theoretically, refractive index with an accuracy ± 0.0001 for the standard condition (T=20°C, $\lambda = 0.589$ μm) can be obtained when the equipment is operated at ambient temperature ($\approx$ 23°C) [64].

In this experiment, refractive index values of MEA30%wt unloaded and loaded CO_2 were measured every 10°C from 10°C to 50°C. The measured values are plotted versus the temperature in Figure 5.4. It was found that refractive index of MEA30%wt loaded CO_2 is higher than refractive index of MEA30%wt unloaded CO_2, and the refractive index value of both liquids decrease when the temperature increases.

Figure 5.3: Refractometer (Abbemat 300)

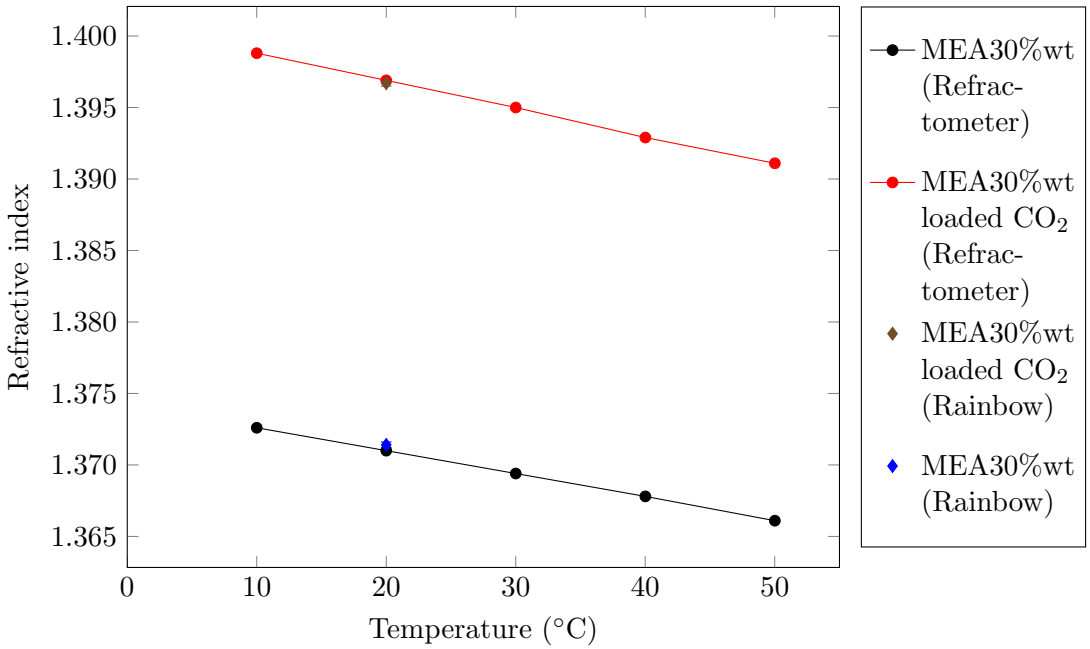

Figure 5.4: Measured refractive index values of MEA30%wt unloaded and loaded CO_2 from refractometer (measuring every 10°C from 10°C to 50°C) and rainbow technique (measuring at room temperature about 20°C)

5.4 Refractive index measurement on a line of moving droplets by rainbow technique

Refractive index values of MEA30%wt unloaded and loaded CO_2 were measured by rainbow technique. The measurements were performed at ambient temperature about 20°C in order to compare with the measured values from refractometer. The optical adjustment and calibration system were identical as described in section 4.3. However, the diverging lens which was used to expand the laser beam was removed while the circular diaphragm was added and adjusted the diameter to be 4 mm for the measurements in this section.

5.4.1 Description of liquid system and operating condition

Schematic diagram of liquid system is displayed in Figure 5.5. The liquid was stored in a pressurized tank (Volume: 5 L) which is able to work with maximum pressure up to 5 bars. N_2 was filled to the tank with a pressure about 1.5 bars in order to create the differential pressure between system and ambient air, permitting the liquid to flow out. A glass tube flow meter (Brooks Sho-Rate, model: 1355G (R-2-15-AAAA), floating material: stainless steel) was connected to the pressurized tank to control volume flow rate of liquid. A droplet generator (FMP technology, Model: MTG-01-G2) with orifice size 100 μm was used.

MEA30%wt unloaded CO_2 was injected with the volume flow rate about 2.2 ml/min, and the excitation frequency about 9.21 kHz was applied to droplet generator. Based on the computation, the droplet size 196 μm with discharge velocity 4.7 m/s could be produced. In contrast, MEA30%wt loaded CO_2 was injected with volume flow rate about 2.3 ml/min, and the excitation frequency about 10.36 kHz was applied to the generator. Accordingly, the droplet size 192 μm with discharge velocity 4.9 m/s is expected. The rainbow signals for both MEA30%wt unloaded and loaded CO_2 were recorded at the position 40 mm from orifice. The temperature of liquid reservoir is considered as equal to the ambient temperature.

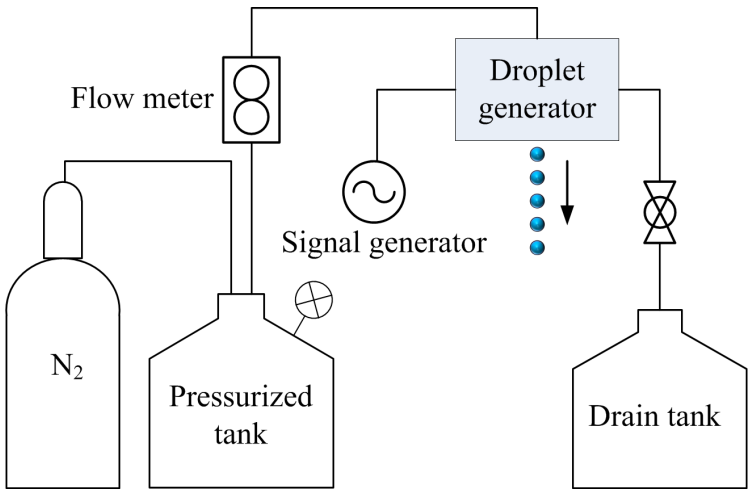

Figure 5.5: Schematic diagram of liquid system for generating a line of moving droplets

5.4.2 Experimental results

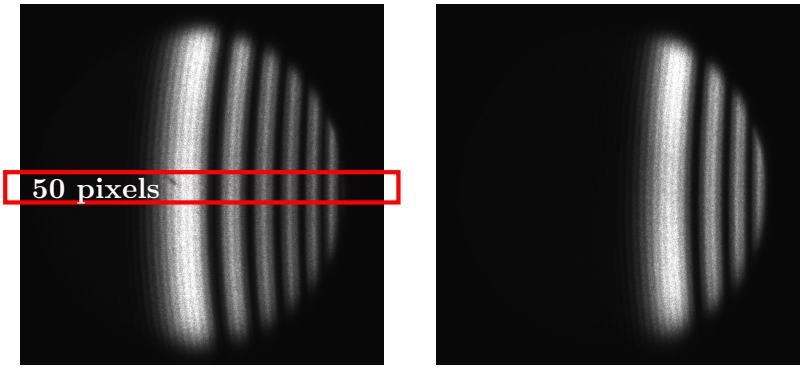

(a) MEA30%wt unloaded CO_2 (b) MEA30%wt loaded CO_2

Figure 5.6: Examples of rainbow pattern created by MEA30%wt unloaded and loaded CO_2 droplets, the angular shift toward the larger scattering angle is clearly visible from rainbow patterns of MEA30%wt loaded CO_2.

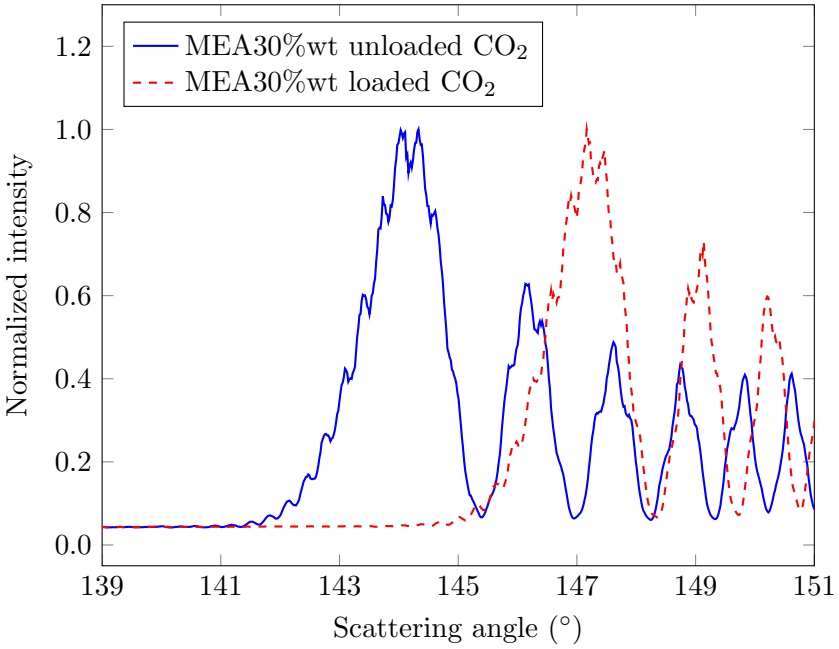

Figure 5.7: The corresponding normalized light distributions from Figure 5.6a, 5.6b were quantified, demonstrating an angular shift approximately 3°.

Table 5.2: Measured refractive index values from refractometer and rainbow technique at temperature 20°C

Measurement method	Solution	Refractive index (T=20°C)
Refractometer	MEA30%wt unloaded CO_2	1.3710±0.0001
	MEA30%wt loaded CO_2	1.3969±0.0003
Rainbow	MEA30%wt unloaded CO_2	1.3714±0.0002
	MEA30%wt loaded CO_2	1.3967±0.0002

Series of 300 rainbow images were recorded by a CCD camera with the exposure time 1.2 ms, which the acquisition time is about 9 frames per second. Typical recorded rainbow images for MEA30%wt unloaded and loaded CO_2 are illustrated in Figure 5.6a, 5.6b respectively. The corresponding normalized light distributions were demonstrated in Figure 5.7. The normalized light intensity was extracted from the middle part of image by summing fifty pixels intensity along the vertical direction while the pixels in horizontal direction were transformed to scattering angle with a relationship obtained by the calibration. It can be seen that the rainbow signal of MEA30%wt loaded CO_2 shifted toward larger scattering angle, representing the increase of refractive index. The inversion code was used in order to search for the best fit between the recorded and computed rainbow signals to extract refractive index and size distribution. From the processing of 300 rainbow signals, the average refractive index values with standard deviations of both solutions were obtained and plotted in Figure 5.4. Additionally, the refractive index values for temperature 20°C obtained from refractometer and rainbow measurement are given in the Table 5.2. In the case of MEA30%wt loaded CO_2, the obtained value from rainbow measurement was in agreement with the value from refractometer by taking into account the standard deviation. In contrast, refractive index of MEA30%wt unloaded CO_2 from rainbow measurement was overestimated about 0.0001 when the standard deviation was considered. Moreover, the average droplet sizes obtained from the inversion code were 181 μm and 205 μm for unloaded and loaded CO_2, respectively.

From the measurements, it was verified that the refractive index variation of MEA30%wt unloaded and loaded CO_2 can be observed by the rainbow system. In addition, refractive index values obtained from rainbow technique were acceptable and comparable to the values from refractometer. Therefore, the next step is to perform refractive index measurement of MEA30%wt during the absorption process. The droplet generator from TSI Incorporated is used which the gas system can be directly connected to droplet generator. Therefore, it is essentially assured that the droplets and gas are in contact.

5.5 Refractive index measurement on a line of moving droplets during CO_2 absorption process by rainbow technique

This section presents rainbow measurements on a line of MEA30%wt droplets under three different conditions which are stagnant ambient air, pure N_2 flow, and pure CO_2 flow. Rainbow images are recorded at different distances from orifice to follow refractive index variation. The description of liquid-gas system, operating conditions, and experimental results are demonstrated, respectively. The optical setup and calibration system were identical as the section 5.4, however the diameter of circular diaphragm was adjusted to be 2 mm.

5.5.1 Description of liquid and gas system

Schematic diagram of liquid and gas system which was used in the experiment is illustrated in Figure 5.8. The droplet generator from TSI Incorporated, model: 3450 was located on three axes of manual translation stages which allowed to be adjusted on left-right, forward-backward, and upward-downward directions. In order to have better a control of liquid volume flow rate, a high precision syringe pump (Chemyx, model: Nexus 6000, syringe volume: 250 ml) was used instead of the pressurized tank and the glass tube flow meter. This syringe pump provides liquid storage including the volume flow rate controller, permits to specify a desired value resulting in a stable liquid injection. The line of droplets was operated in upward direction as shown in Figure 5.9, and a stopper was applied at

the distance about 100 mm from orifice to avoid the reverse flow. This stopper was made from a metal tube, connecting to the used liquid tank, thus the liquid can flow and be stored in the tank. To perform the measurements in the conditions of pure N_2 flow and pure CO_2 flow, the glass tube flow meter (Brooks Sho-Rate, model: 1355G (R-6-15-A), floating material: Glass) was used to control the volume flow rate of gas. Moreover, the cover of droplet generator creates a small chamber permitting to have the co-flow mixing between gas and liquid before access to the ambient. However, the concentration of gas can decrease when the measurement position is farther.

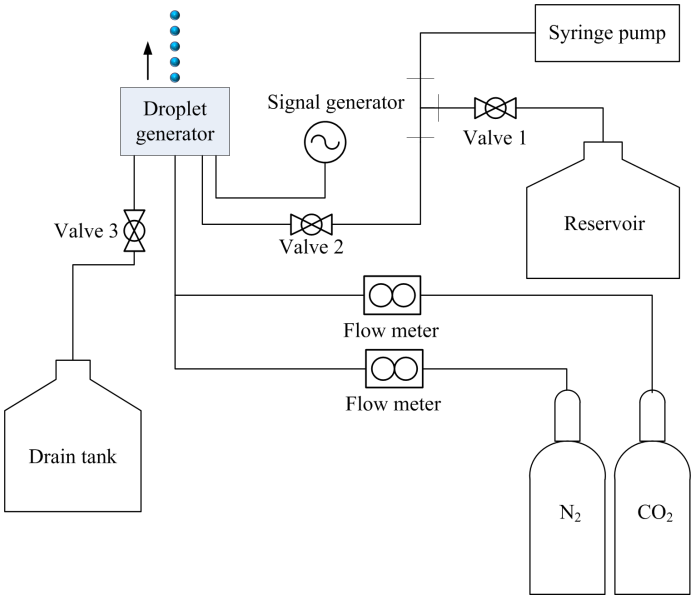

Figure 5.8: Schematic diagram of liquid and gas system

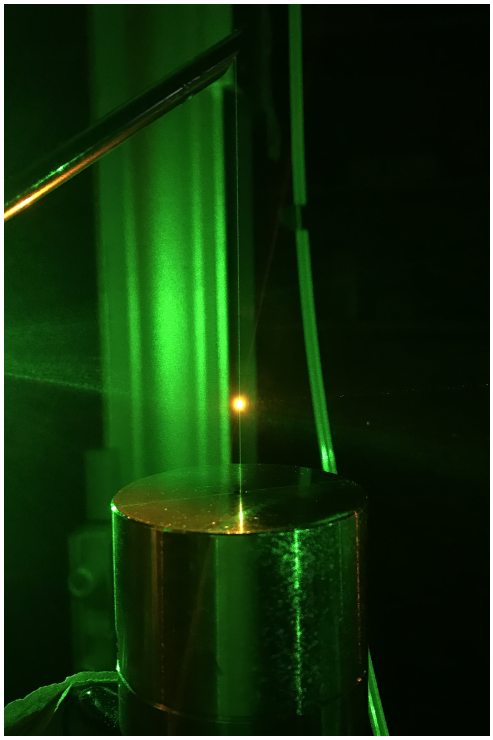

Figure 5.9: A line of moving droplets during operating

5.5.2 Operating conditions

In this measurement, the orifice size 50 μm was inserted on the droplet generator, the volume flow rate equal to 0.6 ml/min was used for the liquid injection, resulting in the discharge velocity of droplets about 5.1 m/s. The excitation frequency in the range of 17 kHz to 19 kHz was applied on the droplet generator, accordingly droplet size in the range of 100 μm to 104 μm is expected. The volume flow rate of N_2 and CO_2 were adjusted to be identical about 0.5 L/min. This value is the maximum gas flow rate, providing the minimum perturbation on the line of droplets. For both conditions, the gas flow was applied 20 minutes prior starting the measurements in order to assure that inside the small chamber is saturated by N_2 and CO_2 ambient. The measurements were done at ambient temperature about 20°C for all conditions. Series of 500 rainbow images were recorded by a CCD camera with the exposure time 1.2 ms. The acquisition time is about 9 frames per second. Considering the excitation frequency for generating droplets with the exposure time on CCD camera, rainbow signal in an image is created by about 20 to 22 drops. Series of rainbow images were recorded at different positions from 9 mm to 43 mm from orifice.

5.5.3 Experimental results

Examples of recorded rainbow image from MEA30%wt droplets under the conditions of stagnant ambient air, pure N_2 flow, pure CO_2 flow are depicted in Figures 5.10a, 5.10b, 5.10c, respectively. These images belong to the measurement position at 23 mm from orifice, it can be seen that the recorded rainbow images are similar, and cannot be distinguished any changes by eyes. Then, the corresponding normalized light distributions were extracted from the middle part of the images, and plotted versus the scattering angle in Figure 5.11. Rainbow signal of MEA30%wt in stagnant ambient air is plotted in blue while the red one represents rainbow signal of MEA30%wt in pure N_2 flow. It can be seen that the rainbow signals in blue and red are very close, indicates that N_2 flow has no effect on droplets composition and temperature. On the other hand, rainbow signal of MEA30%wt in pure CO_2 flow which is plotted in green has a tiny shift toward the lower scattering angle about 0.6°. This behavior indicates the effect of the gradient due to the chemical reaction between MEA and CO_2. This tiny shift is the biggest shift which obtained from the experiment. It shows that the rainbow technique is accurate enough to characterize even small angular change.

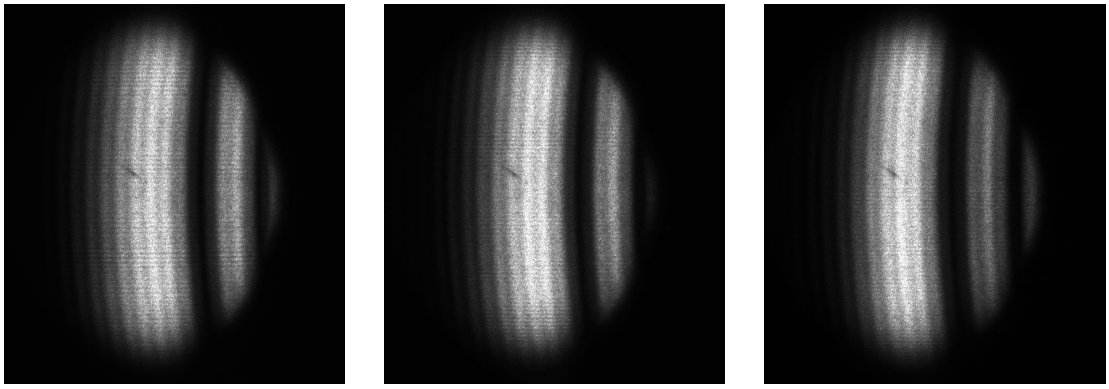

(a) Stagnant ambient air (b) Pure N_2 flow (c) Pure CO_2 flow

Figure 5.10: The recorded rainbow images from MEA30%wt droplets for three conditions demonstrating a small change on rainbow patterns which are unable to see by eyes. Nevertheless, a tiny angular variations were quantified from the analysis of images.

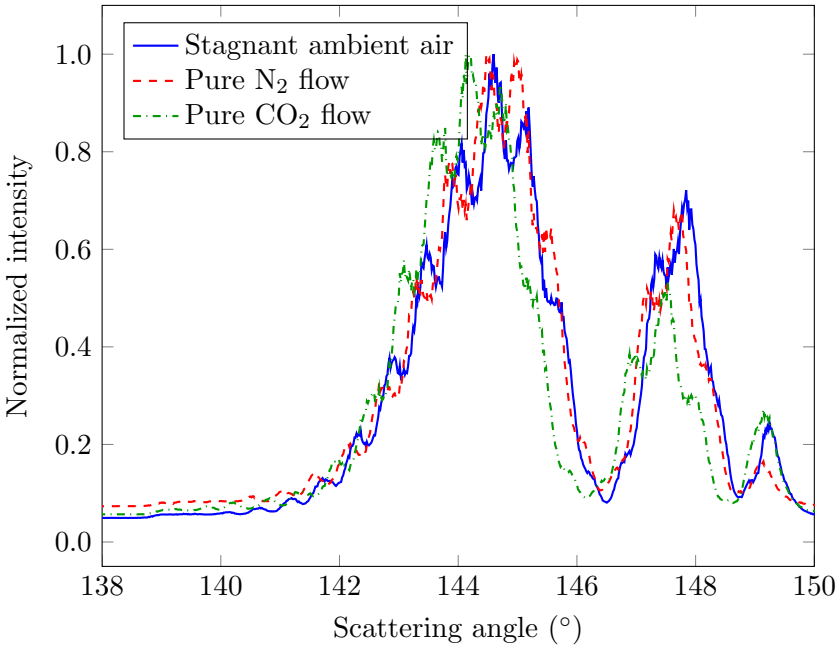

Figure 5.11: The normalized light distributions extracted from the rainbow images in Figure 5.10a, 5.10b, 5.10c, the signals are similar for the conditions of stagnant ambient air and pure N_2 flow, nevertheless a little shift about 0.6° toward the lower scattering angle was observed in the condition of pure CO_2 flow.

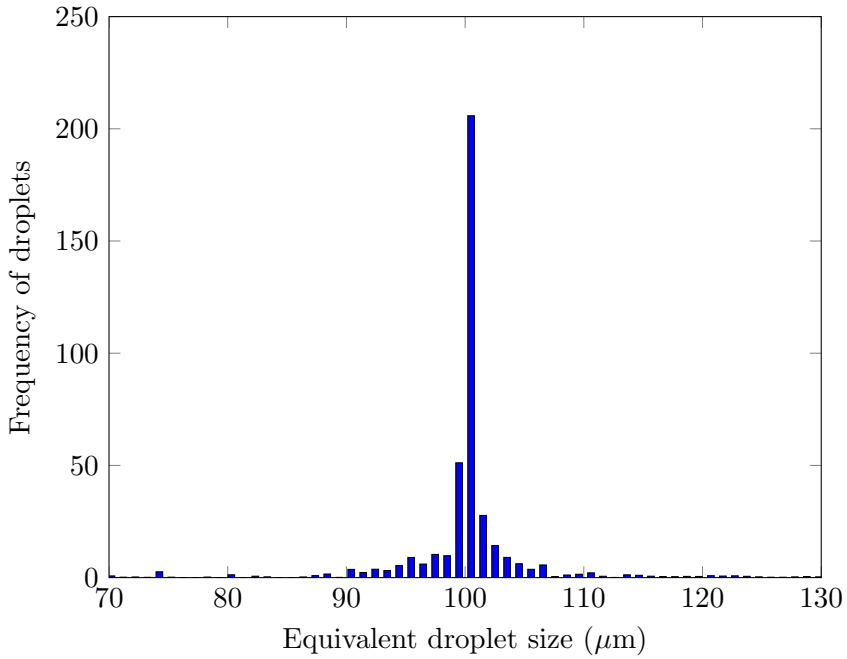

Figure 5.12: Cumulative size distribution obtained from a series of rainbow signals, representing the nearly monodisperse droplets.

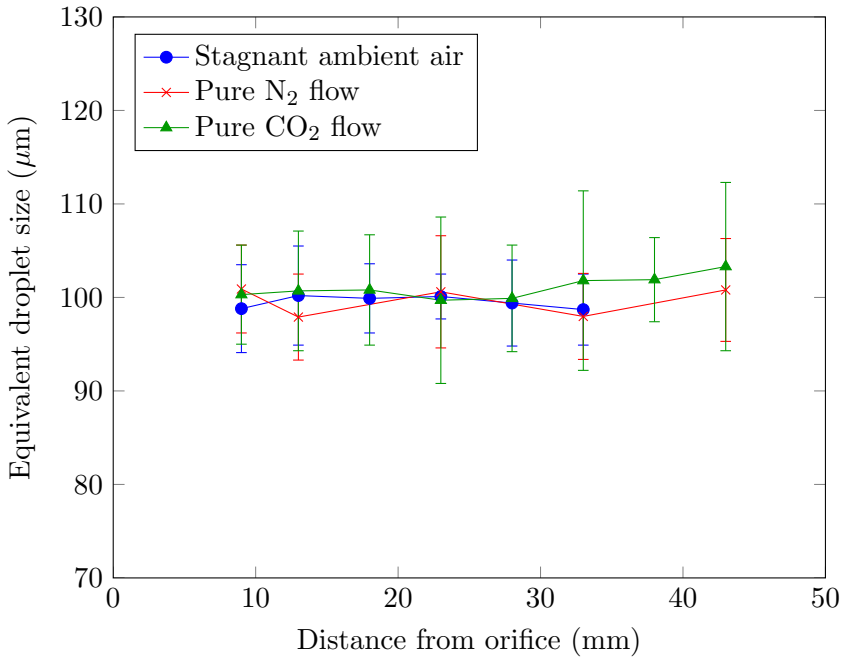

Figure 5.13: The average equivalent droplet sizes and their standard deviations were determined from the cumulative size distributions. For all conditions, the stable equivalent droplet sizes along the measurement positions were obtained.

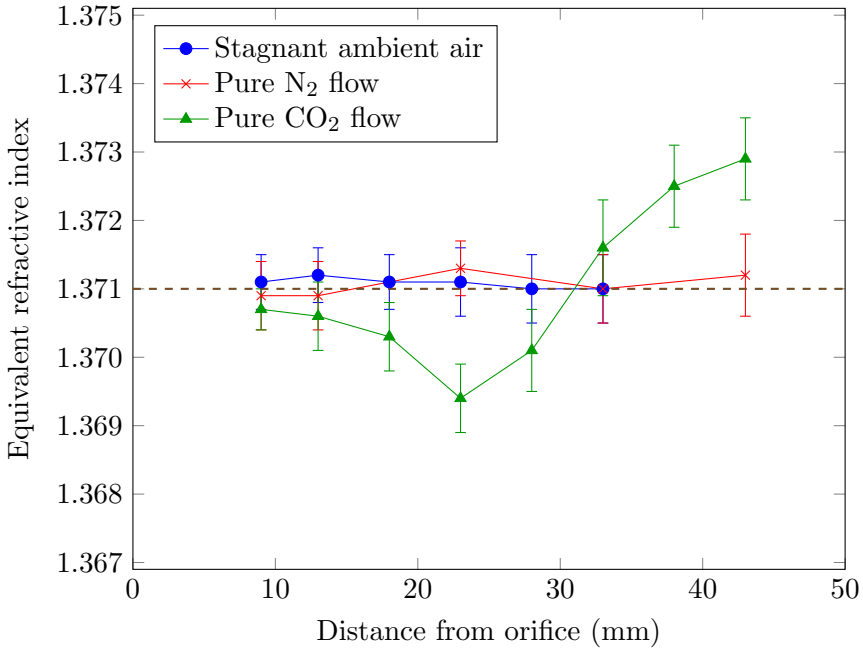

Figure 5.14: The average equivalent refractive index values with standard deviations for all conditions were obtained from at least 300 recorded rainbow signals. The values for the conditions of stagnant ambient air and pure N_2 flow were stable along the measurement positions, and in agreement with refractive index of MEA30%wt at 20°C obtained from refractometer. However, the values in the condition of pure CO_2 flow were a strong function of measurement positions, demonstrating a signature of the existing gradients in droplets.

From such rainbow signals, equivalent refractive index and equivalent droplet size were extracted by using the inversion code. The recorded rainbow signal is imported to the code, the first two peaks of rainbow signal which are areas of main interest on the refractive index information are selected. Then, the sampling points on the selected part are defined to be 200 points in order to reduce the computation time. A range of droplet size is defined corresponding to the expected droplet size which can be computed as described in Appendix B.1. In this work, the range of droplet size 51 μm to 150 μm is selected. These set parameters are used to process all rainbow signals. For operating principle of inversion code, the intensity vector given by the recorded rainbow signal is equal to the product of a matrix A by a vector B, which matrix A represents the scattering of particles, while vector B is drop size distribution [6]. The scattering of particles is computed based on Nussenzveig's theory. Then, the inversion of matrix is solved by using Non-Negative Least Square (NNLS) method to extract the size distribution corresponding to a value of refractive index. The example of cumulative size distribution obtained from a series of rainbow signals is depicted in Figure 5.12 representing nearly monodisperse droplets. The average equivalent droplet sizes were determined from the extracted cumulative size distributions and plotted versus the distances from the orifice in Figure 5.13 which their standard deviations are represented as error bars. The average equivalent droplet size in each condition showed stability along every position of measurement, which indicates that the droplet size was not significantly affected by the gradients in droplets. Therefore, only equivalent refractive index is focused in this study. The average equivalent refractive index values for all conditions were plotted versus the distances from orifice and displayed in Figure 5.14. Each value was averaged from at least 300 recorded images which the standard deviation was plotted as an error bar. It was found that equivalent refractive index values were stable along the measurement positions for conditions of stagnant ambient air and pure N_2 flow. This proved that there is no observable effect of N_2 flow on droplet composition and temperature. In contrast, the equivalent refractive index values in the condition of pure CO_2 flow decreased during positions 9 mm to 23 mm, then continuously increased up to position 43 mm from orifice. The obtained values were less than refractive index of MEA30%wt (1.371 at $T = 20°C$) during the position 9 mm to 28 mm from orifice which are 'unphysical'. However, this characteristic was appeared in the simulation results as a signature of the presence of gradients in droplets. Therefore, the evolution of equivalent refractive index in the condition of pure CO_2 flow is further investigated in order to evaluate the gradients in droplets. Moreover, the measurements were repeated under the identical conditions where the measured equivalent refractive index values for all conditions are given in Table 5.3. It was found that the measured values provided the same behavior i.e. the values were stable along the measurement positions in the conditions of stagnant ambient air and pure N_2 flow while the values in the condition of pure CO_2 flow demonstrated the presence of gradients in droplets.

Table 5.3: Measured equivalent refractive index for all conditions

Measurement (set)	Position from orifice (mm)	Refractive index		
		Stagnant ambient air	Pure N_2 flow	Pure CO_2 flow
1	9	1.3711±0.0004	1.3709±0.0005	1.3707±0.0003
	13	1.3712±0.0004	1.3709±0.0005	1.3706±0.0005
	18	1.3711±0.0004	-	1.3703±0.0005
$T_{amb} = 21°C$	23	1.3711±0.0005	1.3713±0.0004	1.3694±0.0005
	28	1.3710±0.0005	-	1.3701±0.0006
	33	1.3710±0.0005	1.3710±0.0005	1.3716±0.0007
	38	-	-	1.3725±0.0006
	43	-	1.3712±0.0006	1.3729±0.0006
2	9	1.3712±0.0005	1.3715±0.0004	1.3710±0.0002
	13	1.3708±0.0005	1.3707±0.0005	1.3707±0.0004
	18	-	-	1.3703±0.0004
	23	1.3709±0.0004	1.3709±0.0005	1.3686±0.0008
	28	-	-	1.3692±0.0005
$T_{amb} = 21°C$	33	1.3711±0.0005	1.3707±0.0006	1.3696±0.0007
	38	1.3710±0.0005	1.3711±0.0004	1.3701±0.0009
	43	-	1.3709±0.0005	1.3715±0.0007
	48	-	-	1.3730±0.0006
	53	-	-	1.3724±0.0006
3	13	1.3709±0.0003	1.3706±0.0003	1.3700±0.0005
	18	-	-	1.3701±0.0004
	23	1.3709±0.0003	1.3706±0.0005	1.3688±0.0008
$T_{amb} = 21°C$	28	-	-	1.3691±0.0005
	33	1.3710±0.0004	1.3706±0.0005	1.3710±0.0007
	38	-	-	1.3715±0.0008
	43	1.3709±0.0004	1.3707±0.0003	1.3720±0.0006
	48	-	-	1.3717±0.0006
	53	-	-	1.3726±0.0011

5.6 Evaluation of gradients inside droplets by comparing the numerical and experimental results

In this section, the evolution of equivalent refractive index obtained experimentally is analyzed by comparing with the numerical result. To simplify the analysis, refractive index at the center and surface are considered to be constant along every measurement position. The gradient profiles are evaluated, and used to compute the quantity of CO_2 absorbed in a droplet. As the reaction between MEA and CO_2 is exothermic, thus the effect of spatial thermal gradient is clarified by a direct measurement combined with computation of Lewis number. Moreover, the activation energy, Hatta number, and CO_2 absorbed flux are determined. Finally, the quantities of CO_2 absorbed in a droplet computed based on non-homogeneous and homogeneous models are compared.

5.6.1 Refractive index gradients evaluation

According to the simulation results in Figure 3.8, two related parameters i.e. coefficient b and refractive index at the surface of droplet must be considered. It was obvious that the trend of equivalent refractive index from experimental result (for position 9 mm to 28 mm) corresponds to numerical result, when coefficient b is positive. Besides, the experimental result for positions 33 mm to 43 mm was in accordance with numerical result when coefficient b is in the beginning range of negative values. Therefore, the equivalent refractive index values in the range of b -6 to 100 were considered.

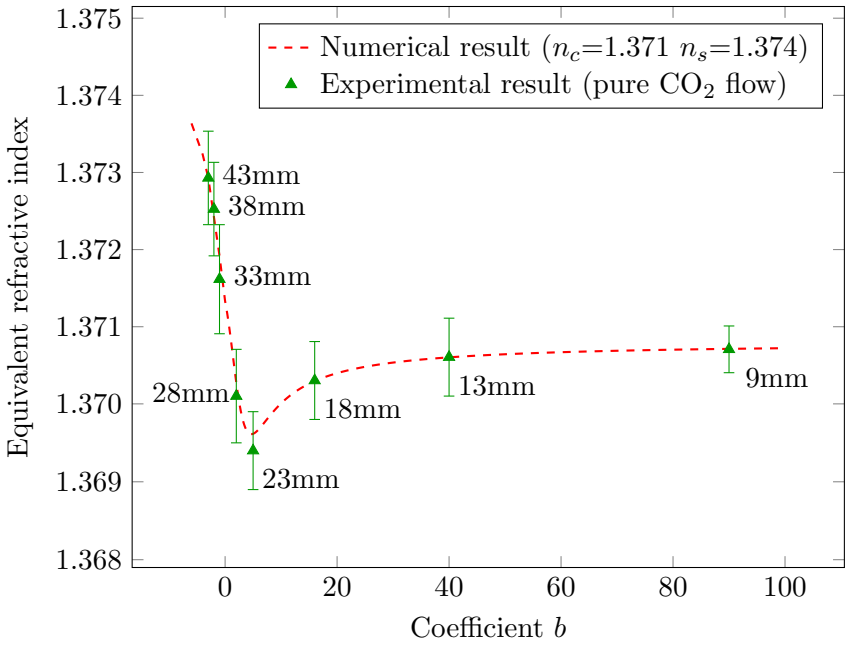

Figure 5.15: The evolution of equivalent refractive index from experimental and numerical results were compared in order to evaluate the gradient profiles. The selection of coefficient b was based on the explanation in section 3.3.5, accordingly the coefficient b decreased at farther position.

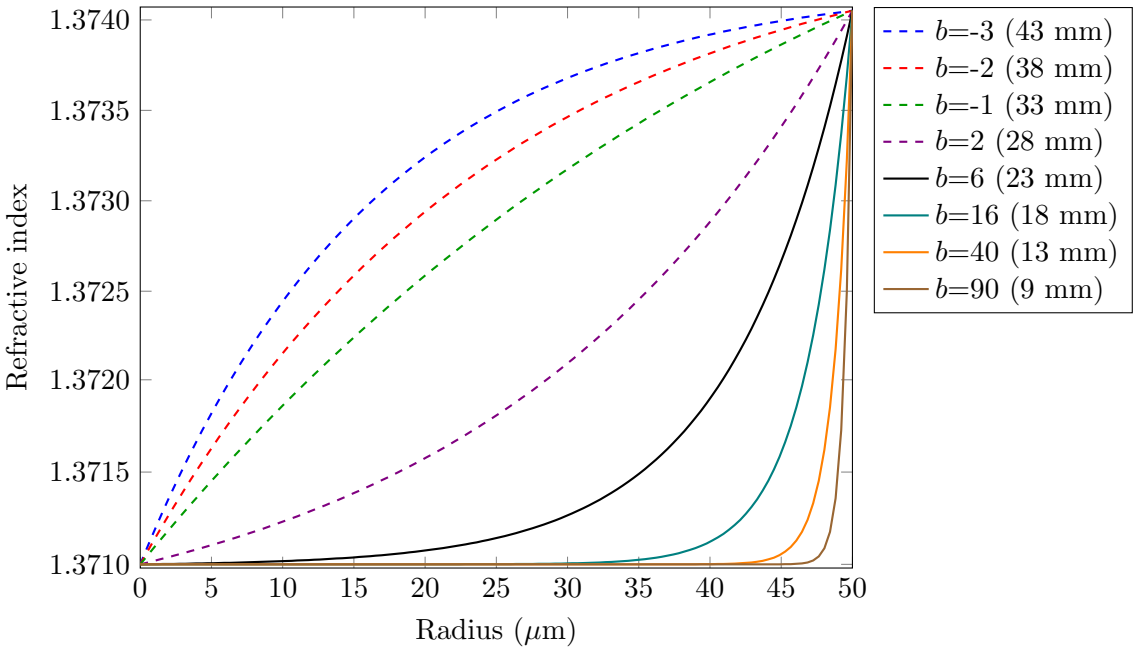

Figure 5.16: Refractive index distributions inside droplet corresponding to the selection of coefficient b in Figure 5.15

Refractive index at the surface of droplet was firstly estimated. The assumption of constant refractive index at the surface along the measurement positions was used. Considering the simulation results in Figure 3.8, it was found that the minimum equivalent refractive index is less when the difference between refractive index at the surface and at the center is greater. Consequently, the minimum value was used as a criteria to estimate refractive index at the surface. It was found that the minimum value from experiment in Figure 5.14 corresponded to the simulation in the case of refractive index at the surface equal to 1.374, representing 10% of CO_2 absorbed at the surface. Therefore, this value was used to be refractive index at the surface of droplet to analyze the experimental results.

Since the reaction between MEA and CO_2 takes place at the surface of droplet, then carbamate counter-diffuses with MEA toward the center of droplet. Consequently, the value of b decreased at farther position. The experimental results were plotted versus the selected b in Figure 5.15, which the corresponding refractive index distributions inside droplet were demonstrated in Figure 5.16. In the next step, the quantity of CO_2 absorbed in a droplet will be investigated according to these gradient profiles.

5.6.2 Investigation of CO_2 absorbed in a droplet

Recalling the measured refractive index values provided by Ouboukhlik [4], the data was fitted by second degree polynomial equation, taking into account two parameters i.e. CO_2 concentration and temperature. The fitted correlation is expressed in equation (5.3), which the corresponding three-dimensional curve is plotted in Figure 5.17.

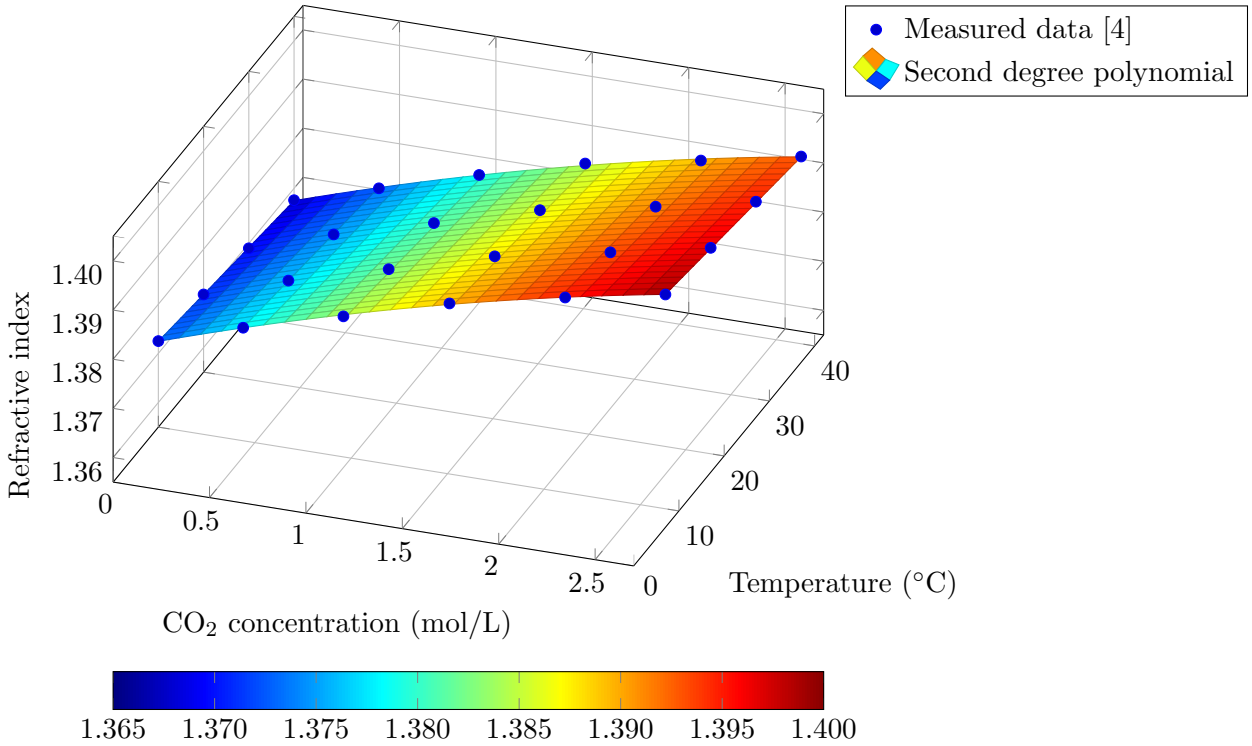

Figure 5.17: Refractive index variation on both temperature and CO_2 concentration

$$n([CO_2], T) = a_1[CO_2]^2 + b_1T^2 + a_2[CO_2] + b_2T + c_1[CO_2]T + c \tag{5.3}$$

where:
- n : refractive index
- T : temperature (°C)
- $[CO_2]$: molar concentration of CO_2 (mol/L)
- a_1 : -0.001198
- a_2 : 0.01318
- b_1 : 4.1668×10^{-8}
- b_2 : -0.000167
- c_1 : -8.004×10^{-6}
- c : 1.37412

Recalling the multilayered sphere model as shown in Figure 3.2, refractive index in each layer obtained in section 5.6.1 can be connected to the local concentration of CO_2 by using the equation (5.3). Then, the quantity of CO_2 absorbed in a droplet is determined according to the equation (5.4).

$$CO_{2,abs} = \sum_{1}^{i=128} \left(V_i \cdot 1000 \cdot [CO_2]_i\right) \tag{5.4}$$

$$V_i = \begin{cases} \frac{4}{3}\pi {r_i}^3, & i = 1 \\ \frac{4}{3}\pi\left({r_i}^3 - {r_{i-1}}^3\right), & 128 \geq i > 1 \end{cases}$$

where:
- V_i : volume in each layer of droplet (m^3)
- r_i : radius in each layer of droplet (m)
- $[CO_2]_i$: molar concentration of CO_2 in each layer of droplet (mol/L)

In order to consider the effect of increasing temperature due to the reaction between MEA and CO_2, the interpretation based on two assumptions which are with and without spatial thermal gradient is considered.

1. **Without spatial thermal gradient**

   According to the refractive index distributions inside droplet in Figure 5.16, CO_2 concentration in each layer of droplet was determined from the equation (5.3), considering the temperature along the droplet radius is constant at 20°C. Then, the quantity of CO_2 loaded in each layer was computed from the multiplication between CO_2 concentration and volume of each layer. Finally, the total quantities of CO_2 absorbed in a droplet were obtained and plotted as function of the contact time in Figure 5.18, represented by the blue triangle scattered with solid line.

2. **With spatial thermal gradient**

   In this case, the spatial thermal gradient is additionally taken into account. The thermal gradient profiles were assumed to be identical shape as refractive index distributions as shown in Figure 5.16. The temperature at the surface of droplet (T_s) was assumed to be 25°C, 30°C, 35°C, and 40°C, while the temperature at the center of droplet (T_c) remains constant at 20°C. Then, the refractive index and temperature in each layer were applied to the equation (5.3) in order to determine the corresponding CO_2 concentration. The quantity of CO_2 absorbed in each layer was computed from the multiplication between CO_2 concentration and volume of each layer. Finally, the total quantities of CO_2 absorbed in a droplet taking into account spatial thermal gradients were obtained and plotted as function of contact time in Figure 5.18, represented by the diamond scattered with dashed lines. The red, green, black, and teal correspond to the cases, where temperature at the surface of droplet equal to 25°C, 30°C, 35°C, 40°C respectively.

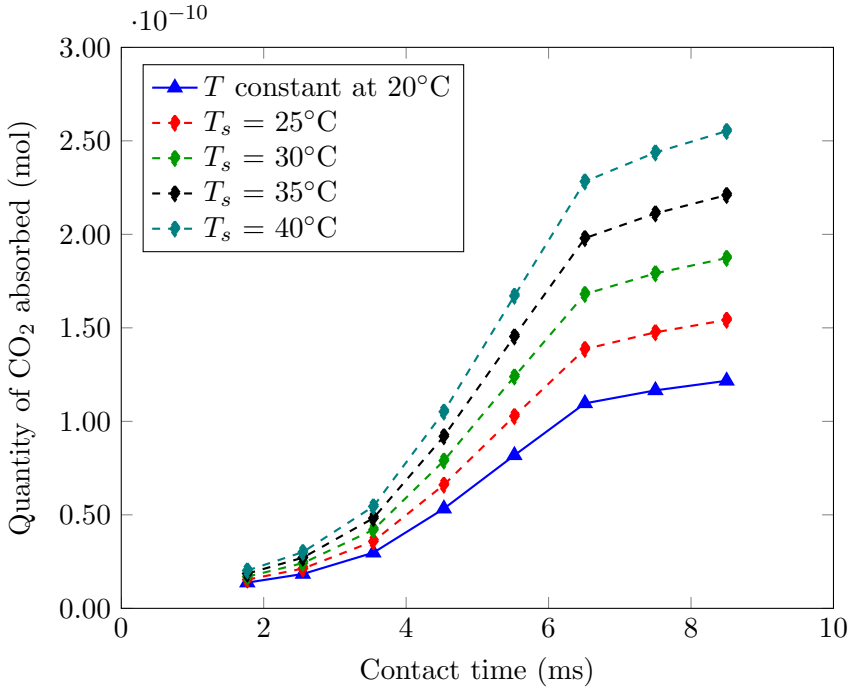

Figure 5.18: Quantities of CO_2 loaded in a droplet for the assumptions with and without spatial thermal gradients

According to Figure 5.18, it was found that the quantities of CO_2 absorbed based on both assumptions increased versus the contact time. The quantity of CO_2 absorbed strongly increased at the beginning, then the slope is less, starting at the contact time about 6.5 ms corresponding to the distance 33 mm from orifice. The change of slope could be due to the decrease of driving force in CO_2 gas, since the system is opened, and CO_2 is mixed with the surrounding air. Moreover, the quantity of CO_2 absorbed at contact time 0 ms representing the droplet before the absorption is considered by continued the same slope of the curve. It can see that the quantity of CO_2 absorbed is not completely zero. Although the identical reactive liquid i.e. MEA30% is used in this study and the study of Ouboukhlik [4], nevertheless the preparation of solution each time could provide a tiny difference in concentration which affects to refractive index. In this study, refractive index of MEA30%wt at 20°C is 1.3710, while the value obtained from Ouboukhlik is 1.3708. Therefore, with the difference on refractive index 0.0002, the overestimation on the quantity of CO_2 absorbed about 0.09×10^{-10} mol could obtain, when the correlation as expressed in equation (5.3) is used.

Comparing the quantity of CO_2 absorbed based on the assumptions of with and without spatial thermal gradient as illustrated in Figure 5.18, it can see that the effect of spatial thermal gradient inside droplet provided the increasing quantity of CO_2 absorbed. Considering at contact time 8.5 ms, the case of temperature at the surface of droplet equal to 35°C provided the quantity of CO_2 absorbed doubled of the case of no spatial thermal gradient. Therefore, the thermal effect are studied and quantified based on two different approaches which are measuring temperature of droplets and computation of Lewis number, presented in section 5.6.3 and 5.6.4, respectively.

5.6.3 Temperature measurement for the conditions of stagnant ambient air and pure CO_2 flow

Temperature measurement under the conditions of stagnant ambient air and pure CO_2 flow was performed. A thermocouple was directly applied to the line of droplets in order to measure the temperature of droplets. The measurements in stagnant ambient air were done at 13 mm, 23 mm, and 43 mm from orifice while the measurements in pure CO_2 flow were done at 13 mm, 23 mm, 28 mm, 33 mm, 43 mm, 53 mm from orifice. The measurements were repeated three times in each position, then the average temperature was determined for each measurement position. The average values are plotted against the distances from orifice in Figure 5.19. It was found that the temperature of droplets in stagnant ambient air is about 19°C, in agreement with the temperature of liquid reservoir while the temperature of droplets in pure CO_2 flow is about 21°C along the measurement positions. From this experiment, it can be concluded that the temperature of droplets increased about 2°C when CO_2 flow was applied.

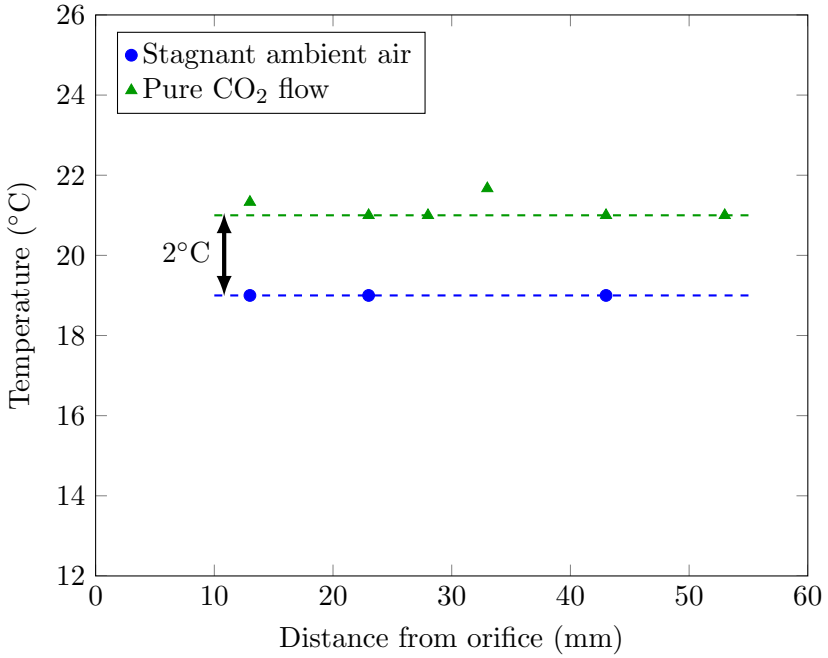

Figure 5.19: Temperature measurement for stagnant ambient air and pure CO_2 flow conditions

5.6.4 Lewis number for CO_2 capture by MEA30%wt

Lewis number is a dimensionless number which is used to characterize the simultaneous effect of heat and mass transfer by comparing thermal diffusivity to mass diffusivity as expressed in equation (5.5).

$$Le = \frac{\kappa}{\rho D_{CO_2,MEA30\%} c_p} \tag{5.5}$$

where: κ : thermal conductivity of MEA30%wt (W/(m·K))
ρ : density of MEA30%wt (kg/m^3)
$D_{CO_2,MEA30\%}$: diffusion coefficient of CO_2 in MEA30%wt (m^2/s)
c_p : specific heat capacity of MEA30%wt at constant pressure (J/(kg·K))

Since the parameters used for Lewis number calculation are temperature dependent, thus Lewis number was computed based on the temperature equal to 25°C which is the closest temperature to the operating condition in the experiment and all required parameters are available.

The density of MEA30%wt was measured by a density meter (Anton Paar, Model: DMA 4100M) every 10°C in the temperature range 10°C to 50°C, where all measured values are provided in Appendix D.2. The density of MEA30%wt at 25°C was determined from the interpolation of the measured values, which is about 1010.6 kg/m^3. The diffusion coefficient of CO_2 in MEA30%wt was computed according to the equation (5.6) as presented in the work of Ouboukhlik [4], using for the temperature range 0°C to 75°C.

$$D_{CO_2,MEA30\%} = (4 \times 10^{-6}) exp\left(\frac{-2395}{T}\right) \tag{5.6}$$

where: T : temperature (K)

Weiland et al. [65] reported specific heat capacity of aqueous MEA, Diethanolamine (DEA), Methyldiethanolamine (MDEA), and aqueous MDEA based blends with MEA, DEA for different CO_2 loaded at 25°C. It was found that specific heat capacity of MEA30%wt unloaded CO_2 was 3734 J/(kg·K). In addition, thermal conductivity of MEA30%wt was estimated according to the study of predicting thermal conductivity of binary liquid mixtures on basis of coordination number [66], where the detail of computation is given in Appendix C.

$$Le = \frac{0.4776}{(1010.6)(1.2985 \times 10^{-9})(3734)} = 97.5$$

According to the calculation based on the specified values, it was found that Lewis number is about 97.5. This means thermal diffusion rate is roughly 100 times faster than mass diffusion rate which demonstrated a faster thermal homogeneity in droplets. Since there is small increasing temperature due to the reaction of MEA and CO_2 as represented in section 5.6.3 with the faster homogeneity in droplets, thus the spatial thermal gradients can be neglected in this study.

5.6.5 Computation of activation energy

Referring to Figure 5.18, the quantity of CO_2 absorbed in a droplet was presented with different temperatures at the surface of droplet. This information can be exploited to determine the activation energy (E_a), which indicates the effect of mass transfer. Therefore, the activation energy is determined according to the Arrhenius equation as expressed in (5.7).

$$k = Ae^{\frac{-E_a}{(RT)}} \tag{5.7}$$

where: k : reaction rate coefficient (L/(mol·s))
A : frequency factor for the reaction (L/(mol·s))
E_a : activation energy (J/mol)
R : universal gas constant ($\approx$ 8.3145 J/(K·mol)
T : temperature (K)

After taking natural logarithm (ln) both sides of equation (5.7), Arrhenius equation can be rewritten in equation (5.8), which is considered as a linear function. Thus, the Arrhenius plot which is the plot between the natural logarithm of reaction rate coefficient ($\ln k$) against the reciprocal of temperature ($1/T$) provides the slope as $-E_a/R$, and the activation energy is obtained.

$$\ln k = \frac{-E_a}{RT} + \ln A \tag{5.8}$$

Firstly, the reaction rate coefficient (k) is determined according to equation (5.9), which the additional parameters i.e. molar concentrations of MEA and CO_2, the reaction rate are needed. MEA30%wt which is used in this study corresponds to molar concentration of MEA 5 mol/L, consequently the molar concentration of CO_2 in equilibrium is 2.5 mol/L.

$$r = k\big[\mathrm{MEA}\big]\big[\mathrm{CO_2}\big] \tag{5.9}$$

where: r : reaction rate (mol/(L·s))
$\big[\mathrm{MEA}\big]$: molar concentration of MEA (mol/L)
$\big[\mathrm{CO_2}\big]$: molar concentration of CO_2 (mol/L)

The reaction rate can be determined from the change in concentration of reactant or product versus the contact time. In this case, the changes in concentration of CO_2 absorbed versus the contact time, which is represented by equation (5.10) are computed based on the data in Figure 5.18 by considering the contact time from 3.54 ms to 6.51 ms, then Δt_c is 2.97 ms. The values of reaction rate, and reaction rate coefficient for droplet temperature 20°C are provided in Table 5.4.

$$r = \frac{\Delta\left[CO_2\right]}{\Delta t_c} \tag{5.10}$$

where: $\Delta\left[CO_2\right]$: the changes in concentration of CO_2 absorbed (mol/L)
Δt_c : contact time difference (s)

Table 5.4: Reaction rate, and reaction rate coefficient at droplet temperature 20°C

T (K)	$1/T$ (K^{-1})	$\Delta[CO_2]$ (mol/L)	r (mol/(L·s))	k (L/(mol·s))	$\ln k$
293.15	3.411×10^{-3}	1.525×10^{-1}	51.35	4.11	1.413

The quantity of CO_2 absorbed which represented by the dashed lines in Figure 5.18 corresponds to the temperature at the surface of droplet equal to 25°C, 30°C, 35°C, and 40°C, while the temperature at the center of droplet remains constant at 20°C. Therefore, the average temperature of droplet is determined from the logarithmic mean temperature difference ($\tilde{T}$) as expressed in equation (5.11). The values of average temperature, reaction rate, and reaction rate coefficient are given in Table 5.5.

$$\tilde{T} = \frac{T_s - T_c}{\ln\left(\frac{T_s}{T_c}\right)} \tag{5.11}$$

where: T_c : temperature at the center of droplet (K)
T_s : temperature at the surface of droplet (K)

Table 5.5: Average temperature, reaction rate, and reaction rate coefficient for the cases, where the temperature at the surface of droplet is 25°C, 30°C, 35°C, and 40°C

T_c (K)	T_s (K)	$\tilde{T}$ (K)	$1/\tilde{T}$ (K^{-1})	$\Delta[CO_2]$ (mol/L)	r (mol/(L·s))	k (L/(mol·s))	$\ln k$
293.15	298.15	295.64	3.382×10^{-3}	1.963×10^{-1}	66.08	5.29	1.665
293.15	303.15	298.12	3.354×10^{-3}	2.407×10^{-1}	81.05	6.48	1.869
293.15	308.15	300.59	3.327×10^{-3}	2.859×10^{-1}	96.27	7.70	2.041
293.15	313.15	303.04	3.300×10^{-3}	3.319×10^{-1}	111.74	8.94	2.190

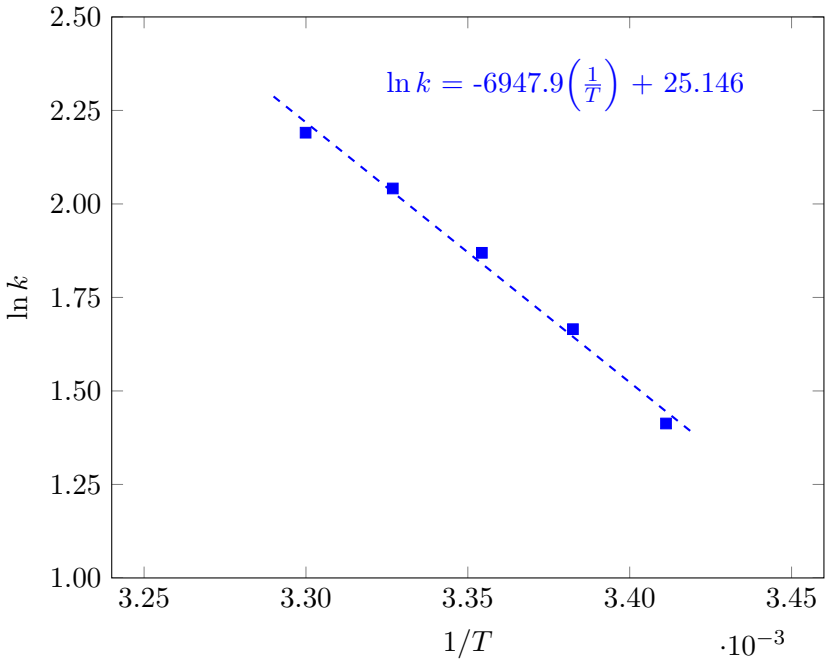

Figure 5.20: Arrhenius plot for CO_2 - aqueous MEA obtained from this study, the values are computed based on the experimental results

$$\frac{-E_a}{R} = -6947.9$$

$$E_a = \frac{6947.9}{8.3145} = 57768.31\text{J/mol} \approx 57.77\text{kJ/mol}$$

In Figure 5.20, the blue square scatters represent the values of natural logarithm of reaction rate coefficient at different droplet temperatures. Then, these values were fitted by linear regression, and plotted as the blue dashed line providing the slope $\left(\frac{-E_a}{R}\right)$ about -6947.9. Therefore, the activation energy equal to 57.77 kJ/mol is obtained in this study, while the activation energy for CO_2 - aqueous MEA equal to 46.7 kJ/mol was presented in the work of Alper [67]. It can see that the activation energy in this study is greater than the value in literature, indicating slower reaction rate. Therefore, the limitation by mass transfer plays a role, supports that there is the existence of gradients in droplet.

5.6.6 Computation of Hatta number

Hatta number (Ha) is a dimensionless number which compares the rate of reaction in liquid film to the rate of diffusion through the film. Some of required parameters which are used for the computation of Hatta number have been already determined i.e. $D_{CO_2,MEA30\%}$, [MEA], and k. However, the liquid side mass transfer coefficient (k_L) is an additionally needed parameter which is determined according to a function provided by Roustan [68]. To select an appropriate function, a dimensionless number (X) as expressed in equation (5.13) is firstly calculated. It was found that the value of X is always less than 0.004 ($X < 4 \times 10^{-3}$), thus the liquid side mass transfer coefficient is determined according to the equation (5.14).

$$Ha = \frac{\sqrt{D_{CO_2,MEA30\%}[\mathrm{MEA}]k}}{k_L} \tag{5.12}$$

$$X = \frac{D_{CO_2,MEA30\%} \cdot t_c}{d^2} \tag{5.13}$$

$$k_L = 2\sqrt{\frac{D_{CO_2,MEA30\%}}{\pi \cdot t_c}} \tag{5.14}$$

where: k_L : liquid side mass transfer coefficient (m/s)
t_c : contact time (s)
d : droplet size (m)

Table 5.6: Liquid side mass transfer and Hatta number at each measurement position

t_c (ms)	X	k_L (m/s)	Ha
1.77	2.004×10^{-4}	9.025×10^{-4}	0.17
2.55	2.887×10^{-4}	7.519×10^{-4}	0.20
3.54	4.008×10^{-4}	6.381×10^{-4}	0.24
4.53	5.129×10^{-4}	5.641×10^{-4}	0.27
5.52	6.250×10^{-4}	5.110×10^{-4}	0.30
6.51	7.371×10^{-4}	4.706×10^{-4}	0.33
7.50	8.492×10^{-4}	4.384×10^{-4}	0.35
8.50	9.624×10^{-4}	4.118×10^{-4}	0.37

The values of liquid side mass transfer, and Hatta number are provided in Table 5.6. It can see that Hatta number obtained from this study is low, and it is in the range of 0.17 to 0.37. The low Hatta number indicates the diffusion limitation, which advocates the hypothesis of the presence of gradient in droplets.

It is obvious that the different analysis methods provides the identical conclusion which indicates the existence of gradient in droplets. In addition, the spatial thermal gradient is negligible in this study as demonstrated in section 5.6.3, 5.6.4. Therefore, the quantity of CO_2 absorbed computed based on the constant temperature at 20°C along the droplet radius and considering only composition gradient.

5.6.7 Computation of CO_2 absorbed flux

As the quantity of CO_2 absorbed is known, the CO_2 absorbed flux (N_{CO_2}) taking into account only composition gradient is then computed according to equation (5.15). The values are plotted versus the contact time in Figure 5.21. The blue curve in Figure 5.21 corresponds to the quantity of CO_2 absorbed which is plotted the blue triangle scattered in Figure 5.18. It can see that CO_2 absorbed flux increases with the contact time until about 5.5 ms, then it decreases until the contact time reaches to 8.5 ms. The decrease of CO_2 absorbed flux could occur due to the change in driving force of CO_2 which is obvious at the farther measurement position (greater contact time). Moreover, the first

point corresponding to the contact time 1.77 ms seems to be overestimated. It could be due to the difference of initial concentration in MEA solution of this work and the work of Ouboukhlik as discussed in section 5.6.2. Accordingly, the quantity of CO_2 absorbed equal to 0.09×10^{-10} mol is subtracted prior to compute the CO_2 absorbed flux. Then, the new CO_2 absorbed flux is represented by the red curve. It was found that the CO_2 absorbed flux is exactly the same values except for the first point, which the value is dropped from the blue curve about 0.16 mol/(m^2·s), providing the reasonable starting point.

$$\dot{N}_{CO_2} = \frac{\Delta CO_{2,abs}}{\Delta t_c \cdot S_d} \tag{5.15}$$

where: $\dot{N}_{CO_2}$: CO_2 absorbed flux (mol/(m^2·s))
S_d : interfacial area of droplet (m^2)
$\Delta CO_{2,abs}$: quantity difference of CO_2 absorbed (mol)
Δt_c : contact time difference (s)

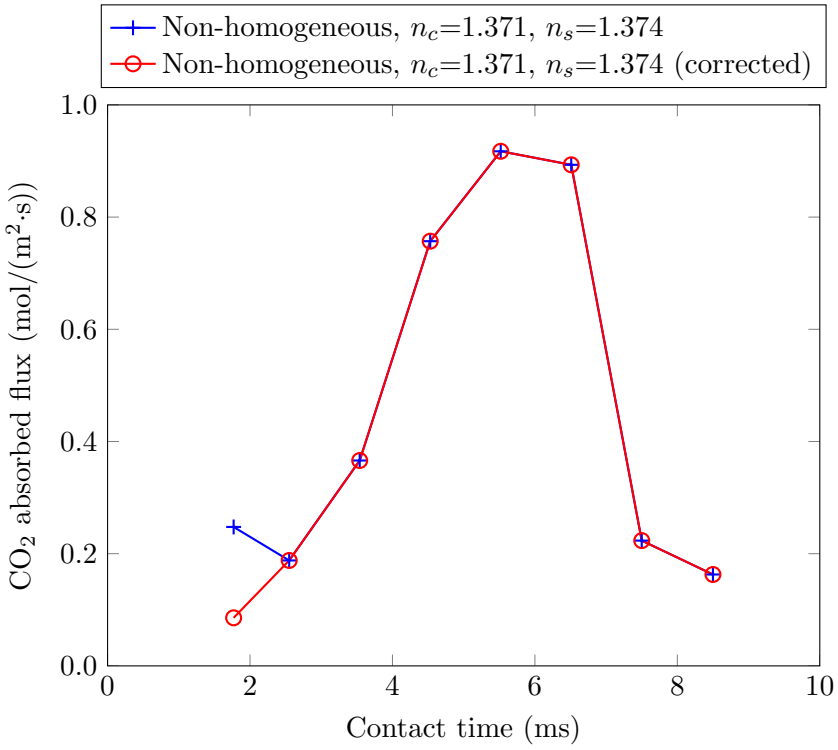

Figure 5.21: CO_2 absorbed flux corresponding to the quantity of CO_2 absorbed (the blue triangle scattered curve) in Figure 5.18

Moreover, the quantities of CO_2 absorbed computed based on non-homogeneous and homogeneous models are compared, as illustrated in Figure 5.22. The homogeneous model provides the negative values, locating in the red ellipse area which corresponds to the contact time about 1.7 ms to 5.9 ms. This behavior is impossible as it means the droplet released CO_2 to the surrounding. At 6 ms, the homogeneous model indicated the starting of CO_2 absorption while the non-homogeneous model provided the amount of CO_2 absorbed about 7% of fully CO_2 loaded. Then, the difference of CO_2 absorbed amounts between both hypotheses decreased to 3% of fully CO_2 loaded when the contact time increased up to 8.5 ms.

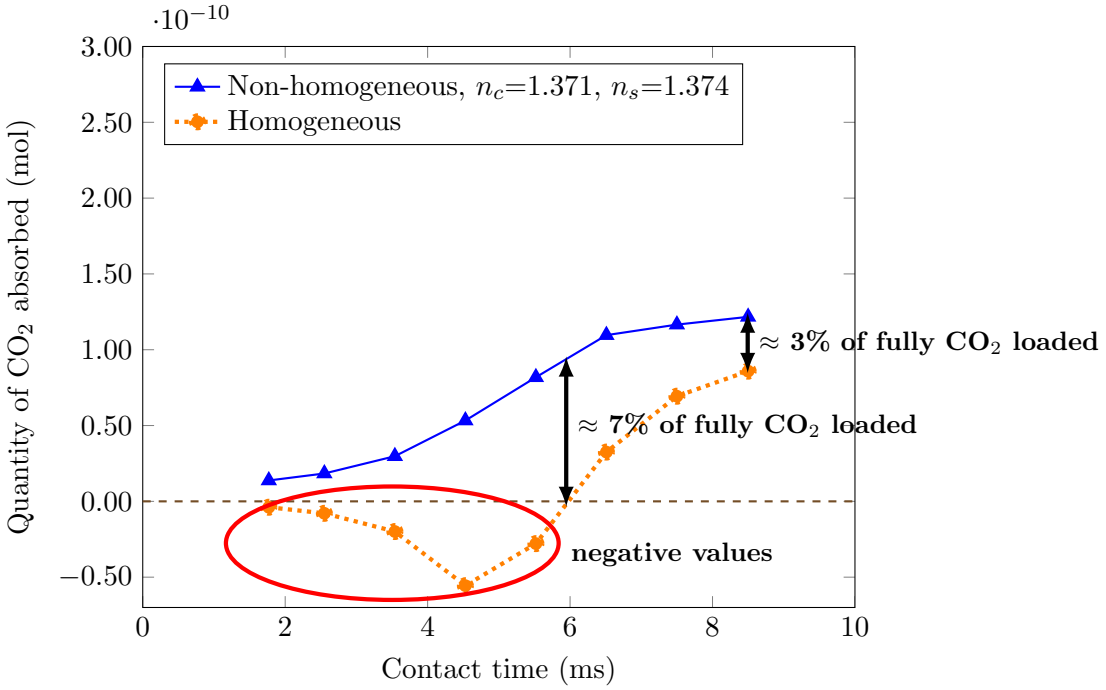

Figure 5.22: Quantities of CO_2 loaded in a droplet computed based on homogeneous and non-homogeneous model for $T = 20°C$

The refractive index distributions or gradient profiles have been already evaluated based on the simplest way which is assumed refractive index at the center, and at the surface of droplet as constant. However, the assumption is not physically acceptable all the times. In order to be more reasonable, the evaluation of refractive index gradients taking into account the change at the center of droplet is considered, and presented in section 5.7.

5.7 Refractive index gradients evaluation taking into account the change at the center of droplet

According to section 5.6.1, the gradient profile corresponding to each measurement position as represented in Figure 5.16 was evaluated without taking into account the variation of refractive index at the center of droplet. However, the center of droplet will obviously be affected by the modification of droplet properties. Therefore, the evaluation of gradient profiles taking into account the change at the center of droplet is presented in this section.

The simulation is firstly redone to see the behavior of equivalent refractive index. In the simulation, refractive index at the center of droplet is defined to be 1.3712, 1.3715, 1.3720, 1.3725, and 1.3730. The coefficient b is varied from 0 to 100 with the increment equal to 1. Then, the identical simulation process as described in section 3.3 is used. The average equivalent refractive index values corresponding to different gradient profiles were determined from the rainbow signals which were computed from droplet size 100.00 μm to 100.28 μm. Then, the smoothed curves are illustrated in Figure 5.23. It was found that equivalent refractive index increase with the rising refractive index at the center of droplet. However, it must be noted that the smoothing procedure provides a tiny change on the curves which affects to the position of minimum equivalent refractive index resulting in the change of b value. Therefore, the gradient profile corresponding to the minimum equivalent refractive index is referred to the coefficient b obtained from the averaging procedure.

Considering Figure 5.16, the gradient profile corresponding to b equal to 2 which

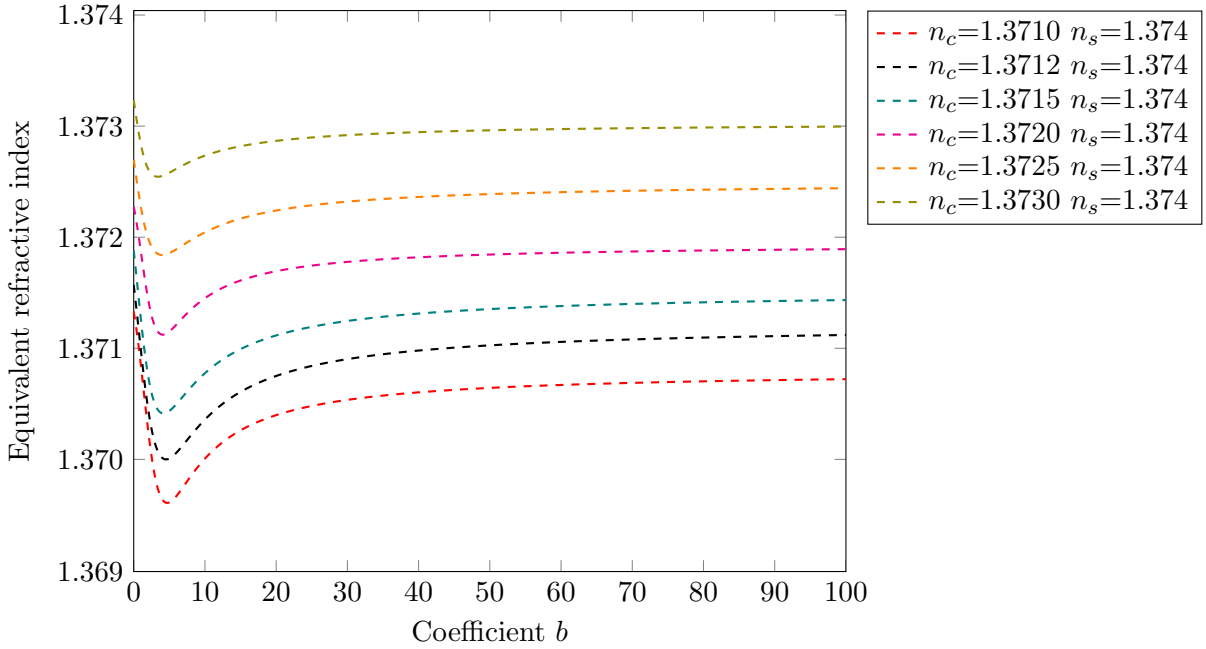

Figure 5.23: Equivalent refractive index at different gradient profiles, extracted from the rainbow signals which are computed from droplet size 100.00 μm to 100.28 μm with smoothing

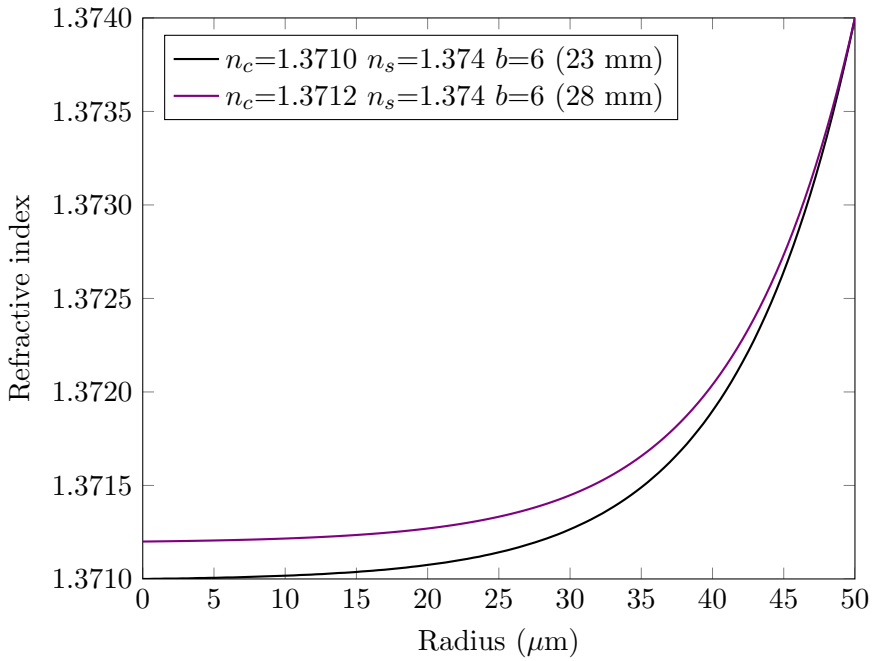

Figure 5.24: Refractive index distributions inside droplet without taking into account the change of refractive index at the center of droplet for position 23 mm from orifice (black), refractive index distributions inside droplet taking into account the change of refractive index at the center of droplet for position 28 mm from orifice (violet)

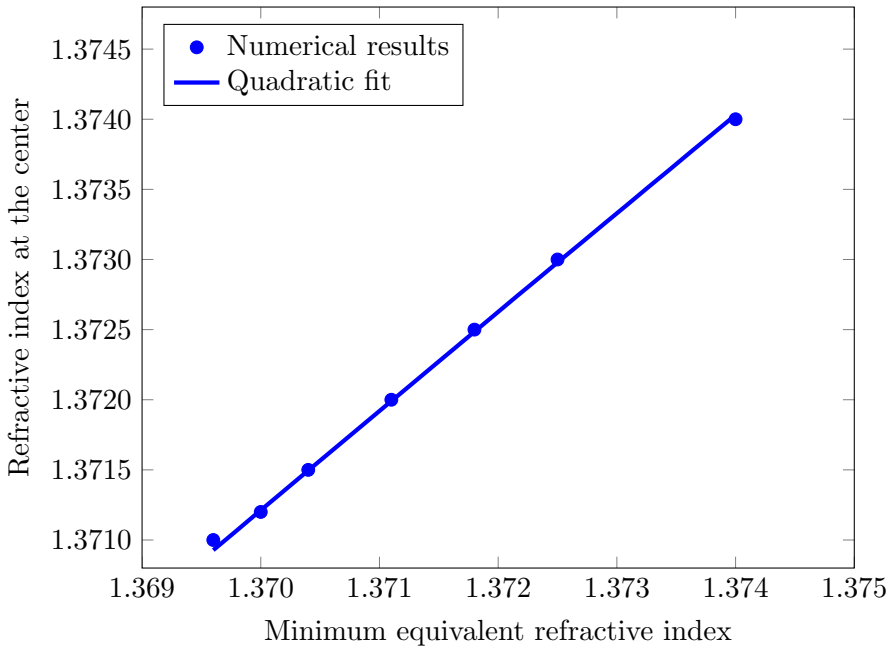

Figure 5.25: Correlation between the minimum equivalent refractive index and refractive index at the center of droplet (for the case of n_s equal to 1.374)

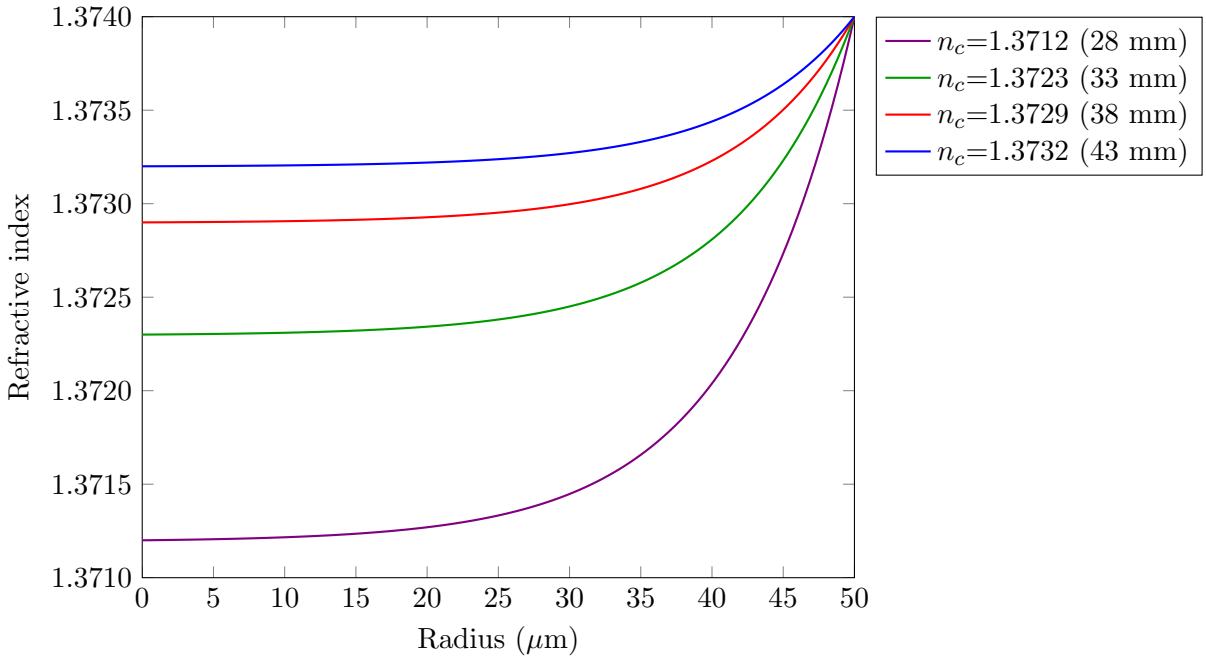

Figure 5.26: Refractive index distributions inside droplet taking into account the change of refractive index at the center of droplet ($n_s = 1.374$, $b = 6$)

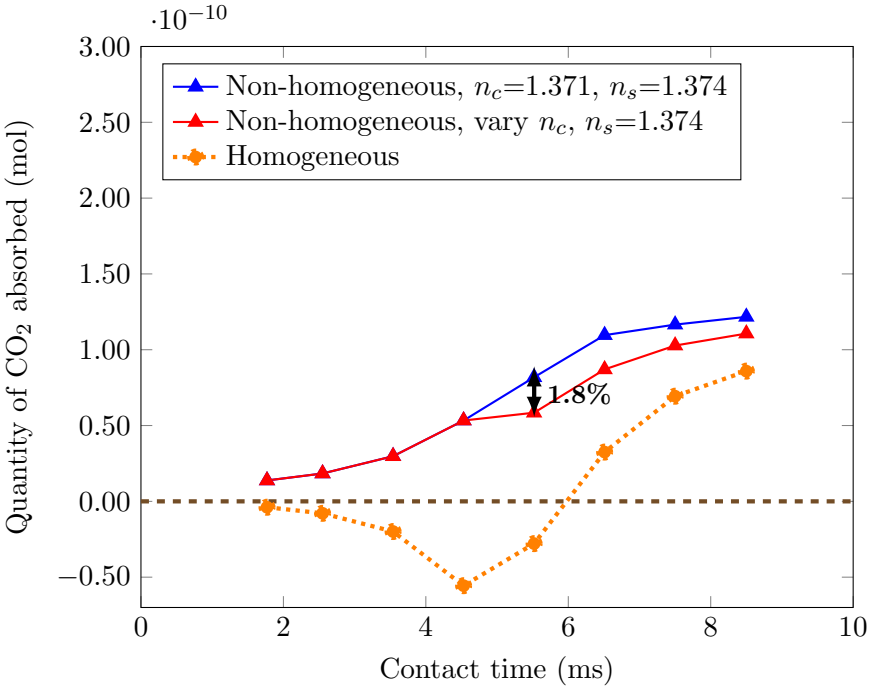

Figure 5.27: Quantities of CO_2 loaded in a droplet based on the assumptions of homogeneous droplet, non-homogeneous droplet with, and without taking into account the change at the center of droplet ($T = 20°C$)

belongs to the measurement position 28 mm seems to be affected at the center of droplet, thus the new gradient profile is evaluated by starting from this measurement position. Since the selected gradient profiles corresponding to the position 23 mm, 28 mm belong to coefficient b equal to 6 and 2 respectively, thus the new gradient profiles are selected from the coefficient b in this range ($2 < b \leq 6$). From the average equivalent refractive index, the minimum equivalent refractive index in each case corresponds to b about 5 or 6, thus in order to be simple, the equivalent refractive index at coefficient b equal to 6 is compared to equivalent refractive index obtained from the experiment. For example, at 28 mm, equivalent refractive index is 1.3701±0.0006, this value is in agreement with the minimum equivalent refractive index for the case of refractive index at the center equal to 1.3712. The corresponding gradient profile is plotted in violet in Figure 5.24.

Moreover, the correlation between the minimum equivalent refractive index and the values of refractive index at the center is plotted in blue scattered points in Figure 5.25, then those data are fitted by quadratic function as plotted in blue line. This correlation is used to determine the value of refractive index at the center, which provides the minimum equivalent refractive index corresponding to the values from experiment (for position 33 mm, 38 mm, and 43 mm). From the correlation, it was found that the equivalent refractive index values obtained from the position 33 mm, 38 mm, and 43 mm are in agreement with the minimum equivalent refractive index, where refractive index at the center is 1.3723, 1.3729, and 1.3732, respectively. The new gradient profiles corresponding to the measurement positions from 28 mm to 43 mm are illustrated in Figure 5.26, which all profiles belong to the coefficient b equal to 6. Then, the quantities of CO_2 absorbed are computed according to these new gradient profiles, and plotted in red in Figure 5.27. It was found that the quantity of CO_2 absorbed increased with the same trend as the blue one which the refractive index at the center was assumed to be constant. The maximum difference of these two hypotheses is less than 2%, where the contact time is about 5.5 ms.

Therefore, from Figure 5.27, the convergence of the curves for non-homogeneous models (both with, without taking into account the change at the center) and homogeneous model could be expected at the later time. This demonstrates the gradients inside droplet is important during the first moments of injection.

5.8 Chapter summary

The refractive index measurements of MEA30%wt unloaded and loaded CO_2 on a line of moving droplets were investigated by rainbow technique. The obtained values were comparable to the values from the refractometer.

A line of MEA30%wt droplets was injected under three conditions i.e. stagnant ambient air, pure N_2 flow, and pure CO_2 flow. Rainbow signals were recorded every 5 mm from 9 mm to 43 mm from orifice. Equivalent refractive index and equivalent droplet size were extracted by using the inversion code. The obtained equivalent droplet size was nearly stable versus the measurement positions for all conditions, thus only equivalent refractive index was focused in this study. For the conditions of stagnant ambient air and pure N_2 flow, it was found that the equivalent refractive index values were stable along the measurement positions. This proved that there is no evaporation effect due to N_2 flow. In contrast, the equivalent refractive index values for the condition of pure CO_2 flow were a strong function of the measurement positions. Moreover, the equivalent refractive index values departed from the range of refractive index of MEA30%wt and refractive index of carbamate representing a signature of gradients in droplets. Accordingly, the evolution of equivalent refractive index was used in order to evaluate the gradient profiles by comparing the experimental and numerical results. In addition, the effect of temperature was considered and quantified by direct measurement and the calculation of Lewis number. From the direct measurement, it was found that the measured temperature increased about 2°C when pure CO_2 flow was applied. Additionally, Lewis number demonstrated the faster thermal homogeneity in droplet, thus the spatial thermal gradients can be neglected in this study. Therefore, only composition gradient was considered. Moreover, the values of activation energy and Hatta number are supported the hypothesis of the existence of gradient in droplets. Then, the quantities of CO_2 absorbed based on the assumption of homogeneous and non-homogeneous droplet were compared. It was found that the effect of composition gradients can be neglected when the measurement position is far enough from the injecting point.

The experimental approach which was used in this study is of general applications which is able to apply for any couples gas-liquid reactions or any situations where the gradient of refractive index from the surface to the center was strong enough.

CHAPTER 6

Concluding remarks

6.1 Summary of accomplishments

The aim of this thesis was to explore the answer of Global Rainbow Technique (GRT) when the scattering particles have a radial refractive index gradient, to propose and test an approach permitting to evaluate this gradient.

For safety reason, experimental facility as well as local 'know-how', the characterization of MEA aqueous droplets during the CO_2 absorption process is selected to be the experimental testing. Rainbow technique has been employed to measure the equivalent refractive index of droplets which is a function of composition and temperature. Both a suspended droplet and a line of moving monodisperse droplets were used in order to perform the experiments. However, the disorganization of rainbow signals in the experiment of suspended droplet for the condition of CO_2 capture provided difficulties on signal interpretation. Therefore, attention was given to the experiment of a line of moving monodisperse droplets.

According to the experimental results on a line of moving droplets, equivalent refractive index was stable and independent to the distances from orifice for the conditions of stagnant ambient air and pure N_2 flow i.e. no evaporation. On contrary, equivalent refractive index for the condition of pure CO_2 flow departed from the range of refractive index of MEA30%wt and refractive index of carbamate. This particular behavior is a signature of the existence of gradients inside droplets. Accordingly, the evolution of equivalent refractive index from the experiment and simulation was compared in order to evaluate the profiles of gradient. In addition, the temperature measurement was also separately performed to clarify the effect of increasing temperature. It was found that the temperature of droplets was increased about 2°C when pure CO_2 flow was applied. From the computation of Lewis number, it was found that the thermal diffusion rate was roughly 100 times faster than mass diffusion rate. Therefore, the spatial thermal gradients in droplets can be neglected in this study. Moreover, the activation energy and Hatta number were computed, which the obtained values supported the hypothesis of the existing gradient in droplets. Finally, the quantities of CO_2 absorbed for a droplet were computed based on the assumptions of homogeneous and non-homogeneous droplet. According to the comparison of the amounts of CO_2 absorbed from both hypotheses, it was found that the effect of composition gradients could be neglected when the measurement position is far enough from the injecting point.

From this study, it is demonstrated that the existence of gradients during the absorption process can be carried out from global rainbow patterns spatial evolution. This approach is of general applications, and can be applied for any couples of gas-liquid reactions or any situations where the gradient of refractive index from the surface to the center is strong enough.

6.2 Perspectives for future research

This study is carried out with droplets to investigate local mass transfer by taking into account the effect of chemical kinetics. Therefore, the perspectives for future research can be discussed in different aspects as followed.

Referring to the results from this study, the intrinsic property of MEA droplets application to CO_2 capture was quantified, demonstrating the effect of composition gradients in the first moments of injection. Accordingly, the evolution of CO_2 absorbed based on the assumption of homogeneous droplet which was presented by Ouboukhlik et al. [4, 34, 35] can be used since the contacting time between gas and liquid were apart from the range of gradients effect. In addition, the obtained results from this study could provide as an experimental database in order to validate the numerical simulation of individual droplet taking into account chemical reaction and mass transfer for the case of CO_2 capture by MEA droplets.

The further investigations by dealing with the chemical kinetics and mass transfer can be considered. According to the literature reviews, the liquid phase mass transfer coefficient increased with the rising temperature. Thus, the experiment with different initial temperature of liquid could be performed in order to search for the optimum temperature, which provide better efficiency of local mass transfer. In addition, the experiment with the droplets electrically charged could be carried out to study the increase of chemical kinetics. Moreover, this experimental approach can be applied for numerous couples of gas-liquid to access the local analysis as well as the investigation in the real reactive spray systems.

In this study, the rainbow signals were recorded at various positions along the line of droplets. A difficulty is to conserve the stability on the line of droplets during the changing positions (during the time). Thus, an extension of rainbow technique named as One-dimensional Rainbow Thermometry (ORT) could be exploited. ORT was recently introduced by Wu et al. [69]. The technique is the extension of a point measurement to one-dimensional measurement providing the possibility to record the rainbow signals corresponding to the different locations along the line **at the same moment**.

Moreover, the evaluation of gradient profiles was manually analyzed in this study. Therefore, the development of automatic process to extract these information could provide faster analysis.

APPENDIX A

Determination of rainbow angle from geometrical optics

According to Figure A.1, the relation of the angles of refraction and reflection are written by equation (A.1) which was rearranged into the form of rainbow angle (θ_{rg}) in equation (A.2).

$$2\pi = (\pi - 2\beta) + (\pi - 2\beta) + 2\tau + (\pi - \theta_{rg}) \tag{A.1}$$

$$\theta_{rg} = \pi - 4\beta + 2\tau \tag{A.2}$$

According to Snell's law, the rainbow angle can be written in term of the incident angle (τ) and refractive index of droplet (n) which is represented in equation (A.3).

$$\theta_{rg} = \pi - 4\left(\sin^{-1}\left(\frac{\sin\tau}{n}\right)\right) + 2\tau \tag{A.3}$$

To find the minimum deviation angle, the first derivative was applied to the equation (A.3).

$$\frac{d\theta_{rg}}{d\tau} = -4\frac{d}{d\tau}\left(\sin^{-1}\left(\frac{\sin\tau}{n}\right)\right) + 2 = 0$$

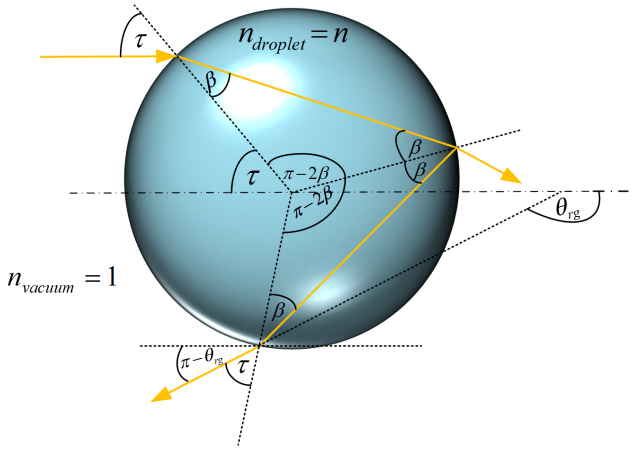

Figure A.1: Interaction between light and spherical droplet

$$-4 \cdot \frac{\cos\tau}{n} \cdot \frac{1}{\sqrt{\left(1-\frac{\sin^2\tau}{n^2}\right)}} = -2$$

$$\frac{\cos\tau}{n} \cdot \frac{1}{\sqrt{\left(1-\frac{\sin^2\tau}{n^2}\right)}} = \frac{1}{2}$$

$$\frac{\cos^2\tau}{n^2} \cdot \frac{1}{\left(1-\frac{\sin^2\tau}{n^2}\right)} = \frac{1}{4}$$

$$\frac{\cos^2\tau}{n^2} = \frac{1}{4}\left(1-\frac{\sin^2\tau}{n^2}\right)$$

$$\frac{\cos^2\tau}{n^2} = \frac{1}{4} - \frac{1}{4}\cdot\frac{\sin^2\tau}{n^2}$$

$$4\cos^2\tau = n^2 - \sin^2\tau$$

$$3\cos^2\tau + (\cos^2\tau + \sin^2\tau) = n^2$$

Using trigonometry relationship,

$$3\cos^2\tau + 1 = n^2$$

$$\cos\tau = \sqrt{\frac{n^2-1}{3}}$$

$$\tau = \cos^{-1}\left(\sqrt{\frac{n^2-1}{3}}\right)$$

Finally, the rainbow angle can be written in term of refractive index of droplet as in equation (A.4), accordingly the rainbow angle can be estimated when refractive index is known.

$$\theta_{rg} = \pi - 4\left\{\sin^{-1}\left[\frac{sin\left(\cos^{-1}\left(\sqrt{\frac{n^2-1}{3}}\right)\right)}{n}\right]\right\} + 2\left[\cos^{-1}\left(\sqrt{\frac{n^2-1}{3}}\right)\right] \qquad \text{(A.4)}$$

APPENDIX B

Computation of initial diameter and traveling time for monodisperse droplets

B.1 Computation of liquid volume flow rate, excitation frequency, and the initial droplet size

According to the guide data provided by TSI Incorporated [9] as plotted in Figure B.1, the correlation between orifice size and volume flow rate of liquid was fitted by the second order polynomial function [10]. The correlation is demonstrated in equation (B.1).

$$\dot{V} = (2.1974 \times 10^{-4}) \cdot D^2 - (5.8363 \times 10^{-4}) \cdot D + 0.0617 \tag{B.1}$$

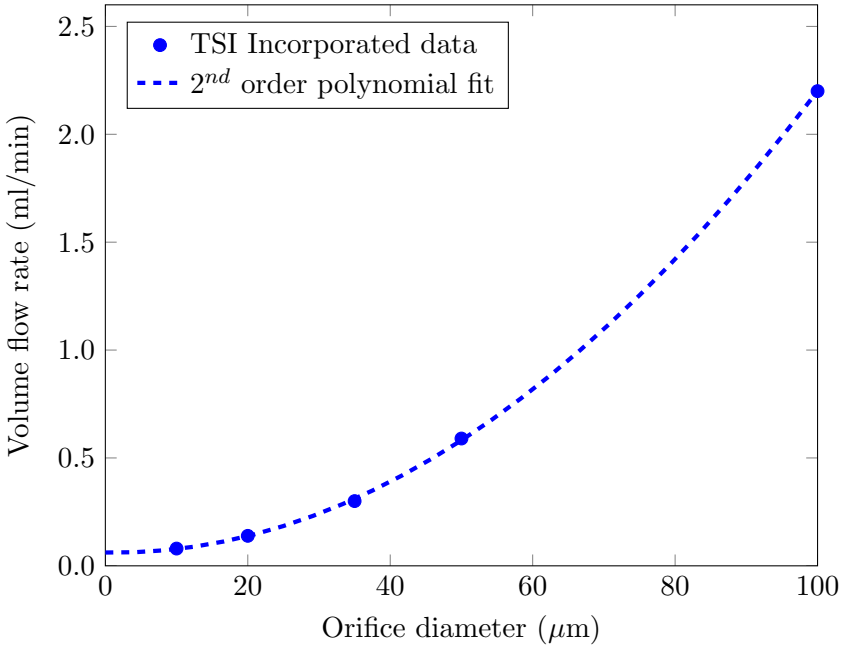

Figure B.1: The correlation between orifice size and volume flow rate of liquid (modified [9, 10])

Based on the Rayleigh breakup of laminar fluid jets, the liquid jet disintegrates into the droplets when the wavelength of deformation on the jet surface is bigger than the circumference of the jet as denoted in equation (B.2) [63]. The piezoelectric vibrating element transfers the interference wave into the liquid jet. The wavelength can be calculated when discharge velocity and excitation frequency are known. The discharge velocity is

computed according to the volume flow rate of liquid and cross sectional area of orifice where is denoted in equation (B.3).

$$\frac{u}{f} \geq \pi D \tag{B.2}$$

$$u = \left(\frac{\dot{V}}{A_d}\right) \cdot \frac{1}{6000} \tag{B.3}$$

In addition, the used interference wave which influences the fluid jet produces the monodisperse droplets when the dimensionless wavelength is located between 0.3 and 0.9 ($0.3 \leq$ k ≤ 0.9) [63].

$$k = \frac{\pi \cdot D \cdot f}{u} \tag{B.4}$$

Therefore, the working range of excitation frequency can be computed from the equation (B.5). Then, the initial droplet size is determined according to the equation (B.6).

$$\frac{0.3 \cdot u}{\pi D} \leq f \leq \frac{0.9 \cdot u}{\pi D} \tag{B.5}$$

$$d = \left(\frac{3 \cdot u \cdot D^2}{2 \cdot f}\right)^{(1/3)} \tag{B.6}$$

where: u : discharge velocity of droplet(m/s)
$\dot{V}$: volume flow rate (ml/min)
A_d : cross-sectional area (cm^2)
k : dimensionless wavelength
D : orifice diameter (m)
d : droplet diameter (m)
f : excitation frequency (Hz)

Table B.1: The computed liquid flow rate, the operating range of excitation frequency, and the estimated range of droplet size for different orifice sizes

D (μm)	A_d (cm^2)	$\dot{V}$ (ml/min)	u (m/s)	Range of f (kHz)	Range of d (μm)
25	4.91×10^{-6}	0.18	6.26	$23.92 \leq f \leq 71.76$	$62.61 \geq d \geq 43.41$
35	9.62×10^{-6}	0.31	5.38	$14.67 \leq f \leq 44.02$	$87.65 \geq d \geq 60.78$
50	1.96×10^{-5}	0.58	4.94	$9.43 \leq f \leq 28.30$	$125.22 \geq d \geq 86.82$
75	4.42×10^{-5}	1.25	4.73	$6.02 \leq f \leq 18.07$	$187.83 \geq d \geq 130.23$
100	7.85×10^{-5}	2.20	4.67	$4.46 \leq f \leq 13.38$	$250.44 \geq d \geq 173.65$

B.2 Computation of traveling time of droplet at different positions from orifice

According to the experiment of upward monodisperse droplets in section 5.5, free body diagram of droplets motion is represented in Figure B.2. The liquid flow rate equal to 0.6 ml/min was applied to produce the line of monodisperse droplets which corresponds to the discharge velocity of droplet equal to 5.1 m/s. The equation of linear motion was used in

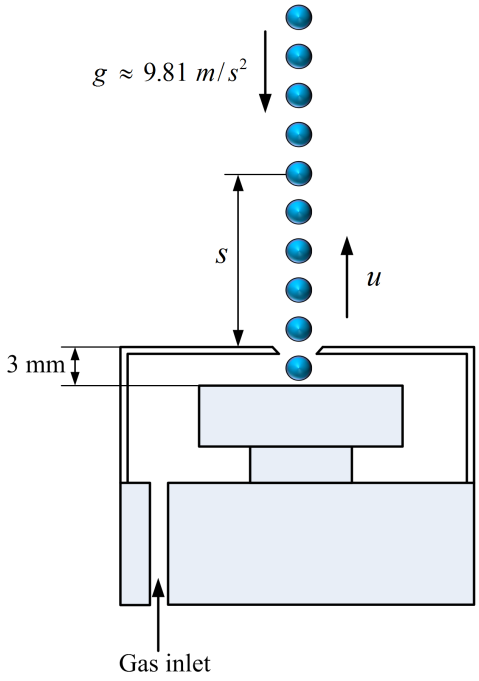

Figure B.2: Free body diagram of moving droplets

order to compute the traveling time for each position. The computed time corresponding to each measurement position is displayed in Table B.2.

$$s = ut + \frac{1}{2}gt^2 \tag{B.7}$$

where: t : traveling time (s)
s : distance from orifice (m)
g : gravitational acceleration (9.81 m/s^2)

Table B.2: Traveling time of droplets at different positions from orifice

Liquid flow rate (ml/min)	Droplet velocity (m/s)	Position from orifice (mm)	time (ms)
0.6	5.1	9	1.77
		13	2.55
		18	3.54
		23	4.53
		28	5.52
		33	6.51
		38	7.50
		43	8.50
		48	9.50
		53	10.5
		58	11.5
		63	12.5

APPENDIX C

Computation of thermal conductivity for MEA30%wt

For the calculation of Lewis number, the thermal conductivity is a required parameter. The thermal conductivity for binary liquid mixture i.e. MEA30%wt was estimated based on a developed model. Tobitani and Tanaka [66] proposed a model for predicting thermal conductivity of binary liquid mixture on basis of coordination number. The randomly mixed packing of particles with two different diameters was used to describe the model. Then, the assumption of heat transfer via the contact points between particles was applied. The estimation was done by considering three types of contact which are water-water, ethanolamine-ethanolamine, and water-ethanolamine, the subscripts A and B in this calculation represent water and ethanolamine, respectively.

The thermal conductivities between water-water molecules (κ_{AA}) and ethanolamine-ethanolamine molecules (κ_{BB}) were defined as thermal conductivity of water (κ_{water}) and ethanolamine (κ_{MEA}), respectively. Thermal conductivity of water was interpolated from thermophysical properties of saturated water [61] while thermal conductivity of ethanolamine was presented in temperature range 298 K to 470 K by DiGuilio et al. [70] which can calculate according to the equation (C.1). In contrast, thermal conductivity between water-ethanolamine molecules (κ_{AB}) was defined in the equation (C.2) [66].

$$\kappa_{AA} = \kappa_{water} = 0.61041(W/(m \cdot K)) \text{ for temperature 298.15 K}$$

$$\kappa_{BB} = \kappa_{MEA} = 0.27719 + (-1.2509 \times 10^{-4})T \tag{C.1}$$

$$\kappa_{AB} = \frac{y}{z} \tag{C.2}$$

where

$$y = \frac{(\sigma_A)z_1^{(\frac{1}{3})} + \sigma_B}{(\sigma_A)z_1^{(\frac{1}{3})}\sigma_B}$$

$$z = \frac{1}{(\sigma_A)z_1^{(\frac{1}{3})}\kappa_{AA}} + \frac{1}{\sigma_B\kappa_{BB}}$$

The thermal conductivity of MEA30%wt (κ) depends on the arrangement of contacts points which can compute according to the equation (C.3) [66].

$$\kappa = \left\{ \frac{\left[\frac{C_1}{\kappa_{AA}}\right] + \left[\frac{C_2}{\kappa_{AB}}\right] + z_2\left[\frac{C_3}{\kappa_{BB}}\right]}{C_1 + C_2 + z_2C_3} \right\}^{-1} \tag{C.3}$$

where

$$C_1 = ((\sigma_A)z_1^{(\frac{1}{3})} + \overline{D})^4 \cdot \frac{(r'_A)^2}{2}$$

Table C.1: The used parameters of water and ethanolamine to compute thermal conductivity of MEA30%wt

Required parameters	Water [71]	Ethanolamine [72]
Molecular weight (g/mol)	18	61.08
Boiling temperature (K)	373.15	443.55
Critical density (g/cm^3)	0.322	0.312
Critical temperature (K)	647.096	614.15

$$C_2 = ((\sigma_A)z_1^{(\frac{1}{3})} + \overline{D})^2(\sigma_B + \overline{D})^2 r'_A(1 - r'_A)$$

$$C_3 = (\sigma_B + \overline{D})^4(1 - r'_A)\frac{(1 - r'_A)}{2}$$

$$r'_A = \frac{W_A M_B}{W_A M_B + z_1 M_A(1 - W_A)}$$

$$\overline{D} = (\sigma_A)z_1^{(\frac{1}{3})} r'_A + \sigma_B(1 - r'_A)$$

The weight fraction of water (W_A) is equal to 0.7 due to MEA30%wt. The size parameter of a molecule (σ) was determined according to the equation (C.4) which was estimated based on the critical volume (V_{cr}) of each substance.

$$\sigma = 0.561 V_{cr}^{(\frac{5}{12})} \tag{C.4}$$

Critical volume (V_{cr}) of each substance was determined from molecular weight (M) divided by critical density. Moreover, the boiling temperatures (T_b) of both substances are used in order to compute the parameter of strength of hydrogen bond (ν). All required parameters of water and ethanolamine are provided in Table C.1.

$$\frac{\varepsilon}{k_{Boltzmann}} = 1.77 T_{cr}^{(\frac{5}{6})} \tag{C.5}$$

$$z_1 = 0.4322 exp\left\{0.6710\left(\frac{\sigma_B}{\sigma_A}\right)\left(\frac{\varepsilon_B}{\varepsilon_A}\right)^{2.2}\right\} \tag{C.6}$$

$$\nu = T_b - 21.5\big(M - 12\big)^{0.591} - 64.2 \tag{C.7}$$

$$z_2 = 0.2\left(\frac{\nu_A}{\nu_B}\right) + 1.188 \tag{C.8}$$

where: ε : potential parameter
$k_{Boltzmann}$: Boltzmann constant
ν : the parameter of strength of hydrogen bond
z_1 : a correction parameter 1
z_2 : a correction parameter 2

From the critical constant, we obtain

$$V_{cr,A} = 55.9006$$
$$V_{cr,B} = 195.7821$$
$$\sigma_A = 2.9995, \frac{\varepsilon_A}{k_{Boltzmann}} = 389.4460$$
$$\sigma_B = 5.0567, \frac{\varepsilon_B}{k_{Boltzmann}} = 372.8510$$

Then, substituting those values into equation (C.6)

$$z_1 = 0.4322exp\left\{0.6710\left(\frac{5.0567}{2.9995}\right)\left(\frac{372.8510}{389.4460}\right)^{2.2}\right\} = 1.2080$$

From the molecular weight and boiling temperature, we obtain

$$\nu_A = 246.9594$$
$$\nu_B = 164.6738$$

Therefore, the parameter z_2 from equation (C.8) was obtained.

$$z_2 = 0.2\left(\frac{246.9594}{164.6738}\right) + 1.188 = 1.4879$$

Finally, thermal conductivity of MEA30%wt for temperature 298.15 K was obtained by substituting all defined values in equation (C.3).

$$\kappa = \left\{\frac{\left[\frac{729.7391}{0.61041}\right] + \left[\frac{365.1645}{0.3820}\right] + 1.4879\left[\frac{45.6825}{0.2399}\right]}{729.7391 + 365.1645 + (1.4879)(45.6825)}\right\}^{-1} = 0.4776(W/(m \cdot K))$$

APPENDIX D

Refractive index and density of MEA30%wt unloaded and loaded CO_2

D.1 Refractive index of MEA30%wt unloaded and loaded CO_2

The refractive index values of MEA30%wt unloaded and loaded CO_2 measured by the refractometer (Abbemat 300) are provided in Table D.1, D.2 respectively.

Table D.1: Refractive index of MEA30%wt unloaded CO_2

Temperature	Refractive index				SD
(°C)	Measure 1	Measure 2	Measure 3	Average	
10	1.3726	1.3726	1.3726	1.3726	0.0000
20	1.3710	1.3710	1.3709	1.3710	0.0001
30	1.3694	1.3694	1.3693	1.3694	0.0001
40	1.3678	1.3678	1.3677	1.3678	0.0001
50	1.3662	1.3662	1.3658	1.3661	0.0002

Table D.2: Refractive index of MEA30%wt loaded CO_2

Temperature	Refractive index			SD
(°C)	Measure 1	Measure 2	Average	
10	1.3987	1.3990	1.3988	0.0003
20	1.3967	1.3971	1.3969	0.0003
30	1.3947	1.3952	1.3950	0.0003
40	1.3927	1.3932	1.3929	0.0003
50	1.3907	1.3914	1.3911	0.0005

D.2 Density of MEA30%wt unloaded and loaded CO_2

The density values of MEA30%wt unloaded and loaded CO_2 measured by the density meter (DMA 4100M) are demonstrated in Table D.3, D.4 respectively.

Table D.3: Density of MEA30%wt unloaded CO_2

Temperature	Density (g/cm^3)				SD
(°C)	Measure 1	Measure 2	Measure 3	Average	
10	1.0165	1.0165	1.0165	1.0165	0.0000
20	1.0127	1.0127	1.0127	1.0127	0.0000
30	1.0083	1.0083	1.0083	1.0083	0.0000
40	1.0034	1.0035	1.0034	1.0034	0.0001
50	0.9981	0.9981	0.9981	0.9981	0.0000

Table D.4: Density of MEA30%wt loaded CO_2

Temperature	Density (g/cm^3)			SD
(°C)	Measure 1	Measure 2	Average	
10	1.1126	1.1128	1.1127	0.0001
20	1.1082	1.1085	1.1084	0.0002
30	1.1034	1.1038	1.1036	0.0003
40	1.0984	1.0989	1.0987	0.0004
50	1.0932	1.0936	1.0934	0.0003

References

[1] Core Writing Team, R.K. Pachauri, and A. Reisinger. Climate change 2007: synthesis report. *Geneva, Switzerland: IPCC*, 104, 2007. (Cited on pages viii, 2 & 3).

[2] Electric Power Research Institute (EPRI). CO_2 capture technology: Technology options for CO_2 capture. *Global CCS Institute*, January 2012. (Cited on pages viii & 4).

[3] J. Han. *Mass transfer characteristics of CO_2 absorption into liquid droplets.* PhD thesis, 2014. (Cited on pages viii, 8 & 9).

[4] M. Ouboukhlik. *Caractérisation du transfert de matière dans un spray réactif pour le traitement des fumées-Application au captage du CO_2.* PhD thesis, INSA de Rouen, 2015. (Cited on pages viii, 4, 7, 9, 10, 18, 19, 59, 60, 62, 63 & 76).

[5] N. Roth, K. Anders, and A. Frohn. Simultaneous measurement of temperature and size of droplets in the micrometer range. *Journal of Laser Applications*, 2:37–42, 1990. (Cited on pages viii & 16).

[6] S. Saengkaew. *Development of novel global rainbow technique for characterizing spray generated by ultrasonic nozzle.* PhD thesis, Chulalongkorn University, 2005. (Cited on pages viii, 15, 17, 18, 26 & 56).

[7] L. Kai, P. Massoli, and A. D'Alessio. Some far-field scattering characteristics of radially inhomogeneous particles. *Particle & Particle Systems Characterization*, 11(5):385–390, 1994. (Cited on pages viii & 22).

[8] M.R. Vetrano, J.P.A.J. van Beeck, and M.L. Riethmuller. Generalization of the rainbow airy theory to nonuniform spheres. *Optics letters*, 30(6):658–660, 2005. (Cited on pages viii & 22).

[9] TSI Incorporated. *Instruction manual (Model 3450 Vibrating orifice aerosol generator)*, 1992. (Cited on pages ix, xi, 45, 46 & 79).

[10] J. Promvongsa. *On experimental study to evaluate evaporation rate of liquid fuel sprays.* PhD thesis, King Mongkut's University of Technology Thonburi, 2013. (Cited on pages xi & 79).

[11] A.B. de Haan and H. Bosch. *Industrial separation processes: Fundamentals.* Walter de Gruyter, 2013. (Cited on page 1).

[12] A.A. Olajire. CO_2 capture and separation technologies for end of pipe applications-a review. *Energy*, 35(6):2610–2628, 2010. (Cited on pages 1 & 3).

[13] R. Thiele and J. Loning. Industrial absorption-current status and future aspects. In *Intitution of Chemical Engineers Symposium Series*, volume 152, page 44. Institution of Chemical Engineers; 1999, 2006. (Cited on page 1).

[14] A.L. Kohl and R. Nielsen. *Gas purification*. Gulf Professional Publishing, 1997. (Cited on page 1).

[15] C.A. Johnson and R. Hutcheson. Alabama electric cooperative flue gas desulfurization operating and maintenance experience. *Journal of the Air Pollution Control Association*, 30(7):744–748, 1980. (Cited on page 2).

[16] Innovative technologies for clean air. Available at `https://www.amecfw.com/documents/brochures-publications/brochures/technologies-for-clean-air.pdf`. (Cited on page 2).

[17] J.K. Lee, S. Banerjee, H.G. Nam, and R.N. Zare. Acceleration of reaction in charged microdroplets. *Quarterly reviews of biophysics*, 48(4):437–444, 2015. (Cited on page 2).

[18] NSW Government. Causes of climate change. Available at `http://climatechange.environment.nsw.gov.au/About-climate-change-in-NSW/Causes-of-climate-change`. (Cited on page 2).

[19] Australian Government (Department of Environment and energy). Greenhouse effect. Available at `http://www.environment.gov.au/climate-change/climate-science-data/climate-science/greenhouse-effect`. (Cited on page 2).

[20] Greenhouse gas. Available at `https://en.wikipedia.org/wiki/Greenhouse_gas`. (Cited on page 2).

[21] D.Y.C. Leung, G. Caramanna, and M.M. Maroto-Valer. An overview of current status of carbon dioxide capture and storage technologies. *Renewable and Sustainable Energy Reviews*, 39:426–443, 2014. (Cited on pages 2 & 3).

[22] Carbon capture and storage association. Available at `http://www.ccsassociation.org/what-is-ccs/capture/`. (Cited on page 3).

[23] R. Davidson. Profiles:pre-combustion capture of CO_2 in IGCC plants. *IEA Clean Coal Centre*, 2011. (Cited on page 3).

[24] Z. Niu, Y. Guo, and W. Lin. Experimental studies on removal of carbon dioxide by aqueous ammonia fine spray. *Science China Technological Sciences*, 53(1):117–122, 2010. (Cited on page 4).

[25] Z. Qing, G. Yincheng, and N. Zhenqi. Experimental studies on removal capacity of carbon dioxide by a packed reactor and a spray column using aqueous ammonia. *Energy Procedia*, 4:519–524, 2011. (Cited on page 4).

[26] S. Ma, B. Zang, H. Song, G. Chen, and J. Yang. Research on mass transfer of CO_2 absorption using ammonia solution in spray tower. *International Journal of Heat and Mass Transfer*, 67:696–703, 2013. (Cited on page 4).

[27] K.H. Javed, T. Mahmud, and E. Purba. The CO_2 capture performance of a high-intensity vortex spray scrubber. *Chemical Engineering Journal*, 162(2):448–456, 2010. (Cited on page 4).

[28] C.H. Yu, C.H. Huang, C.S. Tan, et al. A review of CO_2 capture by absorption and adsorption. *Aerosol Air Qual. Res*, 12(5):745–769, 2012. (Cited on page 4).

[29] H. Hikita, S. Asai, Y. Katsu, and S. Ikuno. Absorption of carbon dioxide into aqueous monoethanolamine solutions. *AIChE Journal*, 25(5):793–800, 1979. (Cited on page 7).

[30] J. Kuntz and A. Aroonwilas. Performance of spray column for CO_2 capture application. *Industrial & Engineering Chemistry Research*, 47(1):145–153, 2008. (Cited on pages 7 & 10).

[31] M. Koller, D. Wappel, N. Trofaier, and G. Gronald. Test results of CO_2 spray scrubbing with monoethanolamine. *Energy Procedia*, 4:1777–1782, 2011. (Cited on page 8).

[32] O. Seyboth, S. Zimmermann, B. Heidel, and G. Scheffknecht. Development of a spray scrubbing process for post combustion CO_2 capture with amine based solvents. *Energy Procedia*, 63:1667–1677, 2014. (Cited on pages 8 & 10).

[33] Y. Tamhankar, B. King, J. Whiteley, T. Cai, K. McCarley, M. Resetarits, and C. Aichele. Spray absorption of CO_2 into monoethanolamine: Mass transfer coefficients, dropsize, and planar surface area. *Chemical Engineering Research and Design*, 104:376–389, 2015. (Cited on pages 9 & 10).

[34] M. Ouboukhlik, G. Godard, S. Saengkaew, M.C. Fournier-Salaün, L. Estel, and G. Gréhan. Mass transfer evolution in a reactive spray during carbon dioxide capture. *Chemical Engineering & Technology*, 38(7):1154–1164, 2015. (Cited on pages 9, 10 & 76).

[35] M. Ouboukhlik, S. Saengkaew, M.C. Fournier-Salaün, L. Estel, and G. Gréhan. Local measurement of mass transfer in a reactive spray for CO_2 capture. *The Canadian Journal of Chemical Engineering*, 93(2):419–426, 2015. (Cited on pages 9, 10 & 76).

[36] S. Zimmermann, M.O. Schmid, B. Klein, and G. Scheffknecht. Experimental studies on spray absorption with the post combustion CO_2 capture pilot-plant CASPAR. *Energy Procedia*, 114:1325–1333, 2017. (Cited on page 10).

[37] X. Wu, M. He, Y. Yu, Z. Qin, and Z. Zhang. Overall mass transfer coefficient of CO_2 absorption in a diameter-varying spray tower. *Energy Procedia*, 114:1665–1670, 2017. (Cited on page 10).

[38] I. Durickovic. Using raman spectroscopy for characterization of aqueous media and quantification of species in aqueous solution. In *Applications of Molecular Spectroscopy to Current Research in the Chemical and Biological Sciences*. InTech, 2016. (Cited on page 14).

[39] F. Lemoine and G. Castanet. Temperature and chemical composition of droplets by optical measurement techniques: a state-of-the-art review. *Experiments in fluids*, 54(7):1572, 2013. (Cited on page 14).

[40] G. Chen, M.M. Mazumder, R.K. Chang, J.C. Swindal, and W.P. Acker. Laser diagnostics for droplet characterization: application of morphology dependent resonances. *Progress in energy and combustion science*, 22(2):163–188, 1996. (Cited on page 14).

[41] G. Schweiger. In-situ determination of the molecular composition of aerosol particles in a monodisperse model aerosol. *Particle & Particle Systems Characterization*, 4(1-4):67–73, 1987. (Cited on page 14).

[42] H.M. Nussenveig. *The theory of the rainbow*. WH Freeman, 1977. (Cited on page 15).

[43] S. Saengkaew. *Optical characterization of discrete media: From Rainbow to Fourier Interferometric Imaging*. 2014. Habilitation à Diriger les Recherches (HDR), Université de Rouen. (Cited on pages 15, 16 & 18).

[44] N. Roth, K. Anders, and A. Frohn. Refractive-index measurements for the correction of particle sizing methods. *Applied optics*, 30(33):4960–4965, 1991. (Cited on page 16).

[45] J.P.A.J. van Beeck and M.L. Riethmuller. Nonintrusive measurements of temperature and size of single falling raindrops. *Applied optics*, 34(10):1633–1639, 1995. (Cited on page 16).

[46] J.P.A.J. van Beeck, D. Giannoulis, L. Zimmer, and M.L. Riethmuller. Global rainbow thermometry for droplet-temperature measurement. *Optics letters*, 24(23):1696–1698, 1999. (Cited on page 16).

[47] J. Promvongsa, B. Fungtammasan, G. Gréhan, S. Saengkaew, and P. Vallikul. A study on the evaporation of water–ethanol mixture using rainbow refractometry. *Journal of Energy Resources Technology*, 139(6):062002, 2017. (Cited on page 18).

[48] X. Wu, Y. Wu, S. Saengkaew, S. Meunier-Guttin-Cluzel, G. Gréhan, L. Chen, and K. Cen. Concentration and composition measurement of sprays with a global rainbow technique. *Measurement Science and Technology*, 23(12):125302, 2012. (Cited on page 18).

[49] A. Verdier, J.M. Santiago, A. Vandel, S. Saengkaew, G. Cabot, G. Gréhan, and B. Renou. Experimental study of local flame structures and fuel droplet properties of a spray jet flame. *Proceedings of the Combustion Institute*, 36(2):2595–2602, 2017. (Cited on page 18).

[50] L. Kai and P. Massoli. Scattering of electromagnetic-plane waves by radially inhomogeneous spheres: a finely stratified sphere model. *Applied optics*, 33(3):501–511, 1994. (Cited on page 22).

[51] F. Onofri, G. Gréhan, and G. Gouesbet. Electromagnetic scattering from a multilayered sphere located in an arbitrary beam. *Applied optics*, 34(30):7113–7124, 1995. (Cited on page 22).

[52] Z.S. Wu, L.X. Guo, K.F. Ren, G. Gouesbet, and G. Gréhan. Improved algorithm for electromagnetic scattering of plane waves and shaped beams by multilayered spheres. *Applied optics*, 36(21):5188–5198, 1997. (Cited on page 22).

[53] Z.S. Wu and Y.P. Wang. Electromagnetic scattering for multilayered sphere: recursive algorithms. *Radio Science*, 26(6):1393–1401, 1991. (Cited on page 22).

[54] M.R. Vetrano, J.P.A.J. van Beeck, and M.L. Riethmuller. Assessment of refractive index gradients by standard rainbow thermometry. *Applied optics*, 44(34):7275–7281, 2005. (Cited on page 22).

[55] S. Saengkaew, T. Charinpanitkul, H. Vanisri, W. Tanthapanichakoon, Y. Biscos, N. Garcia, G. Lavergne, L. Mees, G. Gouesbet, and G. Gréhan. Rainbow refractrometry on particles with radial refractive index gradients. *Experiments in Fluids*, 43(4):595–601, 2007. (Cited on pages 22, 24 & 27).

[56] K. Anders, N. Roth, and A. Frohn. Influence of refractive index gradients within droplets on rainbow position and implications for rainbow refractometry. *Particle & particle systems characterization*, 13(2):125–129, 1996. (Cited on page 22).

[57] C.D. Richards and R.F. Richards. Transient temperature measurements in a convectively cooled droplet. *Experiments in Fluids*, 25(5):392–400, 1998. (Cited on page 23).

[58] C. Laurent, Y. Biscos, N. Doué, C. Maqua, F. Lemoine, G. Gréhan, and G. Lavergne. Thermal gradient determination inside vaporizing droplets by combining rainbow and laser induced fluorescence measurements. In *Proceedings of ASME Fluids Engineering Division Summer Meeting*, 2006. (Cited on page 23).

[59] R.J. Hopkins, C.R. Howle, and J.P. Reid. Measuring temperature gradients in evaporating multicomponent alcohol/water droplets. *Physical Chemistry Chemical Physics*, 8(24):2879–2888, 2006. (Cited on page 23).

[60] C.D. Rosebrock, S. Shirinzadeh, M. Soeken, N. Riefler, T. Wriedt, R. Drechsler, and L. Mädler. Time-resolved detection of diffusion limited temperature gradients inside single isolated burning droplets using rainbow refractometry. *Combustion and Flame*, 168:255–269, 2016. (Cited on page 23).

[61] A.C. Yunus and A.B. Michael. *Thermodynamics: An engineering approach Sixth Edition (SI Units)*. McGraw-Hill, New York, 2007. (Cited on pages 39 & 83).

[62] Ethanolamine. Available at `http://www.ilo.org/dyn/icsc/showcard.display?p_card_id=0152`. (Cited on page 39).

[63] Ü. Acikel. *Assembly and operating instructions monodisperse droplet generator*, 2011. (Cited on pages 45, 79 & 80).

[64] Abbemat performance and performance plus line. Available at `https://www.anton-paar.com/corp-en/products/details/abbemat-performance-and-performance-plus-line/`. (Cited on page 47).

[65] R.H. Weiland, J.C. Dingman, and D.B. Cronin. Heat capacity of aqueous monoethanolamine, diethanolamine, n-methyldiethanolamine, and n-methyldiethanolamine-based blends with carbon dioxide. *Journal of Chemical & Engineering Data*, 42(5):1004–1006, 1997. (Cited on page 64).

[66] A. Tobitani and T. Tanaka. Predicting thermal conductivity of binary liquid mixtures on basis of coordination number. *The Canadian Journal of Chemical Engineering*, 65(2):321–328, 1987. (Cited on pages 64 & 83).

[67] E. Alper. Reaction mechanism and kinetics of aqueous solutions of 2-amino-2-methyl-1-propanol and carbon dioxide. *Industrial & Engineering Chemistry Research*, 29(8):1725–1728, 1990. (Cited on page 66).

[68] M. Roustan. *Transfert gaz-liquide dans les procédés de traitement des eaux et des effluents gazeux*. Tec & Doc, 2003. (Cited on page 66).

[69] X. Wu, H. Jiang, Y. Wu, J. Song, G. Gréhan, S. Saengkaew, L. Chen, X. Gao, and K. Cen. One-dimensional rainbow thermometry system by using slit apertures. *Optics letters*, 39(3):638–641, 2014. (Cited on page 76).

[70] R.M. DiGuilio, W.L. McGregor, and A.S. Teja. Thermal conductivities of the ethanolamines. *Journal of Chemical and Engineering Data*, 37(2):242–245, 1992. (Cited on page 83).

[71] International Association for the properties of Water and IAPWS G5-01(2016) Steam. Guideline on the use of fundamental physical constants and basic constants of water. September 2001. (Cited on page 84).

[72] Ethanolamine (C_2H_7NO). Available at `http://www.matweb.com/search/datasheet.aspx?matguid=76f1162706d74d688816ba88e067afb7&ckck=1`. (Cited on page 84).